LAURA M. BICKLEY

STUDIES TO IMPROVE THE *IN VIVO* MEASUREMENT OF STRONTIUM BY X-RAY FLUORESCENCE

By

LAURA M. BICKLEY, B. Sc., M. Sc.

A Thesis
Submitted to the School of Graduate Studies
in Partial Fulfilment of the Requirements
for the Degree Doctor of Philosophy

McMaster University DOCTOR OF PHILOSPHY (2024) Hamilton, Ontario (Medical Physics)

TITLE: Studies to improve the *in vivo* measurement of strontium by X-ray fluorescence

AUTHOR: Laura M. Bickley B.Sc (University of Guelph) M.Sc. (McMaster University)

SUPERVISOR: Dr. Fiona E. McNeill

COMMITTEE: Dr. Soo Hyun Byun, Dr. Eric Da Silva, Dr. Marcin Wierzbicki

PAGES: xvii, 143

ABSTRACT

Strontium is a rare earth element, present in products such as pyrotechnics, medications, glass and certain pigments. Exposure of humans to strontium mainly comes through dietary means, through the consumption of food and water. While high levels of strontium have been shown to be toxic in animal studies, low levels may be beneficial, such as for the treatment of osteoporosis. Some women in Canada choose to self-supplement with strontium with the intention of preventing this bone disease. At present, there is no clinical tool to monitor strontium levels in these women. A technology that could montior women would be useful as it would allow the determination of whether the self-supplementation is indeed beneficial. To measure strontium in humans, a non-invasive, non-destructive technique called X-ray fluorescence (XRF) is used. This thesis describes work to develop improved technology for *in vivo* measurements of strontium in bone using XRF.

A new XRF system for measuring strontium in bone was designed around a VITUS H150 Silicon Drift Detector (SDD) from KETEK GmbH, and used a ^{109}Cd source in a 180^{o} backscatter geometry. The system was calibrated against a series of anthropomorphic finger phantoms which were 3D printed with a strontium doped hydroxyapatite core and varying polylactic acid (PLA) thicknesses to simulate different thicknesses of soft tissue. Phantoms with a range range of strontium concentrations were created to test the system.

It was determined that the new system was able to perform as well as previously tested radioisotope-based *in vivo* strontium XRF systems, with the system having the potential to perform significantly better if a significantly more active source could be employed. Calibration using the 3D printed phantoms was also found to perform extremely well, indicating that this phantom methodology is a viable way to make more anatomically correct calibration phantoms in the future.

A Monte Carlo model was created in the EGS 5 code of the experimental geometry and the model performance was benchmarked against experimental data. This model was then used to test two separate issues. First, the model was used to determine the validity of coherent normalization for *in vivo* strontium measurements in the finger. Second, the model was used to determine if there was a radioisotope source that could result in better performance of the system.

The coherent normalization was shown to not be valid in terms of correction for soft tissue attenuation, but may be valid as a correction method for errors in positioning or patient motion. In combination with a new Compton correlation method that can estimate the thickness of overlying soft tissue, the implementation of coherent normalization would reduce variability in the system's measurements of the strontium signal.

Finally, through the testing of alternative radioisotope sources, ^{103}Pd was identified as a promising alternative source of fluorescing photons and it is recommended that an experimental XRF system employing this source be tested to verify this result.

ACKNOWLEDGEMENTS

First and foremost I would like to thank my supervisor Dr. Fiona E. McNeill for providing a tremendous amount of guidance and support over these 5 tumultuous years. I would also like to extend my thanks to Dr. Soo Hyun Byun and Dr. Marcin Wierzbicki for being on my committee and providing me with valuable guidance and support. My thanks also to Dr. Eric Da Silva for who, in addition to his support as my committee member, allowed me to join in on his lab group meetings, and provided me with the use of his labs for creation of my phantoms.

My thanks to Minahil Manzoor for helping me make the phantoms, without whom I would not have been able to get them done as fast as we did! As well as my thanks to Dr. Sami Bangash and Bobby Tang for their help in setting up and troubleshooting EGS5 code. To my fellow graduate (Mélodie, Brendan, Sami, Bobby, Michelle, Helen) and undergraduate lab members (Taren, Etain, Megan, Josie, Renée, Dhara, Sonia), thank you for all the laughs, stories, and Viking mouse funerals (RIP Algernon and Fish). You have all given me wonderful memories. I would also like to thank all those who I shared an office with in TAB again for all the wonderful conversations, memories and hours spent playing cards at the TAB office table.

My thanks also goes out to Dr. Joanne O'Meara from the University of Guelph who suggested I apply to McMaster in the first place, and to Dr. Sara Mahallati and Dr. Taufik Valiante for taking me on as a summer student in their lab during my final year of undergrad, and to Dr. Homeira Moradi. I would also like to extend my thanks to Justin Bennett and Shereecia Bangura for all their help with 3D printing, as well as for our many wonderful conversations.

I would also like to thank my friends from my undergraduate (Lauren, Asha, Jen, Rebecca, Emily and Sierra), high school (Nisa, Elinor) and childhood (Kaveri, Sene) for listening to my rants, and for otherwise keeping me sane.

Finally thank you to my parents Cathy and David for getting me through this!

TABLE OF CONTENTS

List of Figures:

Chapter 1:

Chapter 2

List of Tables

Chapter 1

List of Abbreviations and Symbols:

A

ABS – acrylonitrile butadiene styrene

Ag – silver

B

Be – beryllium

BMD – bone mineral density

C

Ca – calcium

Cd – cadmium

109Cd – cadmium 109

D

DEXA/DXA – dual energy X-ray absorptiometry

E

EC – electron capture

EGS5 – Electron Gamma Shower 5

F

FDM – fused deposition modelling

H

HaP – hydroxyapatite

HPGe – hyperpure germanium

I

I – iodine

125I – iodine 125

IC – internal conversion

K

K_{α} – k-alpha X-ray

K_{β} – k-beta X-ray

M

MCNP – Monte Carlo Neutron Photon

MDL – minimum detection limit

N

Ni – nickel

P

Pb – lead

PLA – polylactic acid

PoP – plaster of Paris

ppm – parts per million

PREVOS – PREvention Of early postmenopausal bone loss by Strontium ranelate

S

SDD – silicon drift detector

Si(Li) – lithium drifted silicon

SLA – stereolithography

SOTI – Spinal Osteoporosis Therapeutic Intervention

Sr – Strontium

STRATOS – STRontium Administration for Treatment of OSteoporosis

T

Ta – Tantalum

Te – tellurium

Ti – titanium

TROPOS – Treatment of Postmenopausal Osteoporosis

X

XRF – X-ray Fluorescence

DECLARATION OF ACADEMIC ACHIEVEMENT

The work presented in this thesis is wholly my own and free from any academic dishonesty or plagiarism.

This thesis has been thoroughly reviewed and, in my opinion, meets the appropriate requirements in scope and quality for a dissertation for a Doctorate of Philosophy.

Chapter 1: Introduction and Methodologies

1.1 Introduction:

1.1.1 Strontium and bone health

Strontium (Sr) is a trace element on Earth, making up 0.04% of the Earth's crust[30]. It is found in rocks, soil, dust and in compounds used in the manufacturing of pyrotechnics, medicines, glass and pigments. The largest exposure of people to strontium comes in the form of food and water, with Canada recommending a limit on Sr in drinking water of 7mg/L[30] and the U.S. recommending a limit of 4mg/L[1].

Canada and the United States limit drinking water strontium levels even though low doses of strontium are not known to cause any adverse health effects in humans and may even be beneficial[1,57,58,71,72]. The limits are in place because high doses may cause impaired growth in children. Animal studies have also shown high doses of strontium may cause rickets, and an increase in mortality[1]. However, there is a purported benefit of low doses of strontium in humans[57,58,71,72]. It has been suggested that it has an effect on bone mineral density (BMD) and the treatment of osteoporosis.

Osteoporosis is a bone disease characterized by abnormalities in the amount and arrangement of bone tissue, usually due to accelerated bone loss[41,42]. When this happens, the structure of the bone is weakened and the likelihood of fractures from minor or major falls increases[41,69]. Approximately 1 in 2 women will break a bone due to osteoporosis and some falls can be fatal if the femoral artery is damaged[42]. A less severe form of osteoporosis, called osteopenia can also occur. Osteopenia differs from osteoporosis in that the weakening of the bone is milder compared with osteoporosis[40].

Osteoporosis generally affects women more than men, with women being four times as likely to develop the disease[69]. It is also more prevalent with age as bone mass generally peaks at age 30[41,55]. Prevalence also seems to be increasing over time. Between 2015 and 2016 a study conducted by the Public Health Agency of Canada (PHAC) found that the rates of osteoporosis diagnosis for the general population over 40 increased from 6% in 2000-2001 to 11.9%, with over 80% of those diagnosed being women[69].

Canada is an aging population, with people aged 85 and older representing one of the fastest growing demographic groups (a 12% increase from 2016 to 2021)[83]. Rates of osteoporosis are thus also likely to increase. This could result in a large burden on our healthcare system. Any drugs or compounds that could potentially prevent or delay the onset of osteoporosis would be beneficial to individuals and the public good.

A technique called Dual Energy X-ray Absorptiometry or Dual X-ray Absorptiometry (DEXA or DXA) is the gold-standard for diagnosis of osteoporosis or osteopenia[39]. DEXA scans take between 5 and 20 minutes to complete in clinic[96]. They assess bone mineral density via measurements of the differential attenuation of two beams of x-rays. The patient BMD is compared to the 'normal' BMD of a healthy population sample matched to ethnicity and sex. The difference between the measured BMD and the health population BMD is then calculated, using a T-score[39]. If the T-score is between 1 and 2.5 standard deviations below the mean of the healthy population then this is a clinical indication of osteopenia. A T-score of greater than 2.5 standard deviations below the mean of the healthy population is a clinical indication of osteoporosis[39].

It has been suggested that doses of strontium would be beneficial for bone density and could be a treatment to prevent osteoporosis. A detailed overview of strontium's effect on BMD is provided in Chapter 2 of this thesis. A brief overview is summarized here. Strontium ranelate (brought to market as the drugs Protelos[22] and Protos[64]) was first approved for treatment of osteoporosis in the European Union in 2004[22]. Based on promising results from early animal studies, four large scale clinical trials were undertaken (called PREVOS[71], STRATOS[57], TROPOS[72], SOTI[58]) to investigate the minimum dose and long-term efficacy of strontium ranelate. These clinical trials were considered a success as it was found that at a dose of 2g/day BMD was increased by as much as 6.8% compared with a placebo group whose BMD decreased by 1.3% over the same time range[58]. In addition to the increase in BMD, the trials also resulted in a decrease in the incidence of new vertebral fractures compared to placebo (Reginster 2005).

However, some caution is required in interpretation of the data as these values may be an overestimation as studies found that for every 1% increase in the molar strontium concentration the BMD was overestimated by 10%[9,93]. While this increase in molar strontium concentration would not happen under normal dietary conditions, it may occur for women who take strontium supplements. A 2012[60] study of a woman self-supplementing with 680 mg strontium citrate per day for 2.5 years found that the molar concentration of strontium increased from a baseline of 0.0172% to a plateau of 0.120% for finger measurements, and 0.0177% to 0.289% for ankle measurements.

This overestimation could then mean that the BMD may not have actually changed in the patient, resulting in them being misdiagnosed as not suffering from osteoporosis or osteopenia, when in reality they do. A 2012 study on a woman self-supplementing with 680 mg of strontium-citrate per day found that the Strontium is found naturally in the human body at low levels, with the ratio of strontium to calcium in bone being 0.035 Sr:Ca[63]. This element acts in a similar fashion to calcium in the body when ingested. Once strontium is absorbed, most generally through ingestion of food and water, it is preferentially taken up by bone, and excreted in the urine. The site of highest absorption of strontium in the body are the bones of the iliac crest, and any bones undergoing growth or high turnover[14,65,76,92] . Biopsies of the iliac crest from patients in the STRATOS, SOTI and TROPOS clinical trails determined that strontium was present in up to 48% of the total bone area and was almost exclusively present in recently formed bone[92].

In terms of micro-distribution, strontium is generally considered to be heterogeneously distributed throughout the bone, with the most commonly studied deposition sites being the iliac[14,65,92], femur[14,68] and humerus[14]. There are studies[90] that suggest a more homogenous distribution in measurements of human cadaver fingers. Zamburlini et al. 2009[90] found that the distribution of strontium was uniform throughout the bone, suggesting that depending on the bone site the strontium distribution may change.

A common method to measure strontium in vivo is through the use of the technique of X-ray fluorescence (XRF). A more detailed discussion of the physics behind X-ray fluorescence is presented in later sections of this thesis. In short, X-ray fluorescence works by irradiating a target (in this case bone) with x- or γ-rays, exciting the element. These x-rays or γ-rays can undergo photelectric interactions with strontium. The subsequent de-excitation can lead to the release of x-rays that are characteristic of and specific to strontium. The question of whether strontium is distributed heterogeneously or homogenously in bone may have little impact on in vivo XRF measurements. The XRF technique only interrogates a volume up to a few mm[67,89] into the bone surface and thus the strontium measured by XRF is mostly located at the surface of the bone. Elemental distributions can be problematic for XRF measurements, however Cardenas et al.[11] found that the highest levels of strontium concentration were found near the surface of the bone. The volume sampled by the measurement is thus also the site of highest concentration. The XRF technique has been adopted as a measurement of strontium because an in vivo XRF measurement is painless, non-invasive and relatively simple to perform.

1.1.2 X-ray Interactions

In order to understand x-ray fluorescence measurements of elements in vivo we must first understand how the x-rays interact with matter. The only difference between γ-rays and x-rays is where they originate. γ-rays originate from the nuclear de-excitation of an atom, while x-rays originate from the electron orbitals[10,43].

X- and γ-rays primarily undergo one of five potential interactions with matter[10,45]:

1) Photoelectric effect
2) Compton (incoherent) Scattering
3) Pair Production
4) Elastic (coherent) Scattering
5) Photo nuclear interactions

At low energies (<1 MeV) photoelectric interactions and Compton scattering are dominant, with a lesser amount of elastic scattering taking place. Pair production cannot occur at low energies as it requires γ-rays of energy above 1.022 MeV in order to occur[10]. Photo nuclear interactions are most likely to occur at extremely high energies (>10 MeV) and thus will not be discussed in regards to the low-energy x- or γ-ray interactions that are observed in x-ray fluorescence analysis[45,94]. The interactions that are of interest in this thesis work are thus the photelectric effect, Compton scattering and coherent scattering.

The photoelectric effect occurs when an incident x- or γ-ray interacts with an electron (most commonly inner shell) of an atom, resulting in the ejection of an electron referred to as a photoelectron.

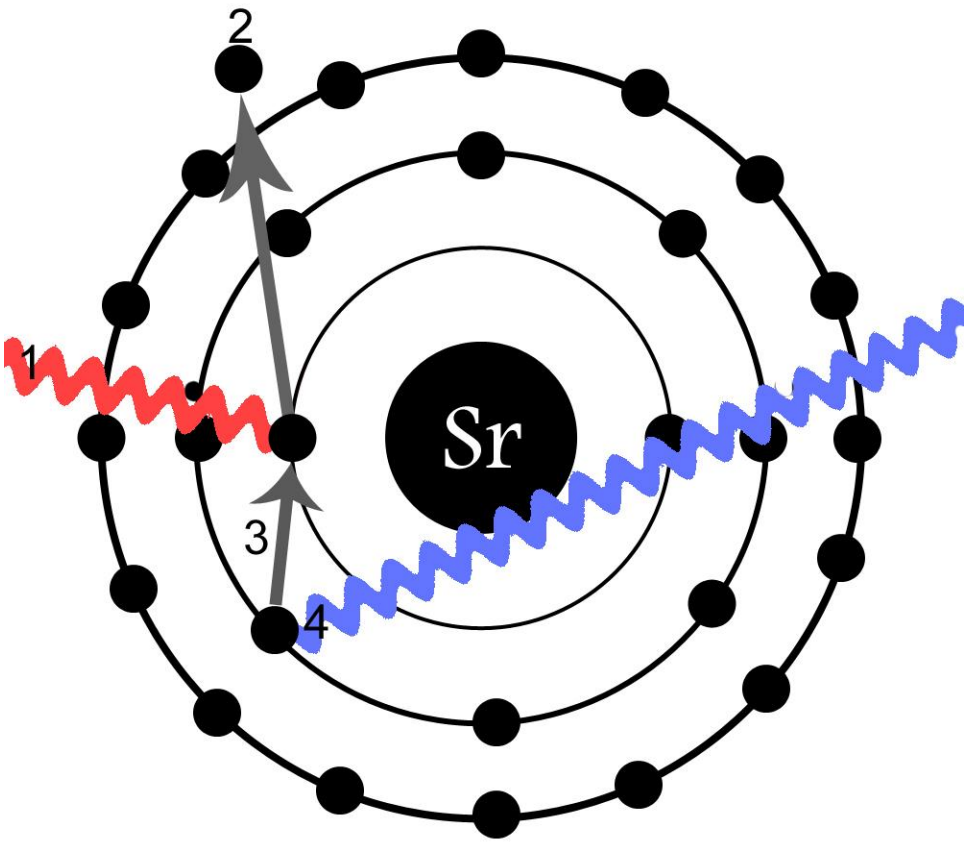

Figure 1: A diagram of the photo-electric effect in a strontium atom. Step 1 shows an incoming photon interacting with an inner-shell electron, transferring it's energy to that electron. Step 2 shows the photoelectron being ejected from the atom. Step 3 shows an electron from a higher energy shell move

to fill the vacancy left by Step 2. Step 4 shows the emission of a characteristic X-ray from the movement of the electron in Step 4.

The kinetic energy of the photoelectron (T) is equal to the difference of the incident x- or γ-ray energy (hv) and the binding energy of the particular shell E_i, where i refers to the shell (K, L, M etc). In order for the photoelectron to be ejected from the shell, the photon must be higher than the binding energy of that particular shell.

$$T = hv - E_i \quad (1)$$

While photoelectric interactions can happen with electrons in other shells, the most common interactions are (if the energy is high enough) with electrons in the inner K-shell. The probability of the interaction is given by the cross section σ and is dependent on the atomic number Z of the atom, proportional to Z^4 at low energies and Z^5at higher energies.[10,20]

The photoelectric effect is the x- or γ-ray interaction that permits the technique of XRF. Both K XRF and L XRF systems have been employed in vivo. When an x- or γ-ray undergoes the photoelectric effect, it must have an energy above the absorption edge. If there is enough energy to cause the ejection of the photoelectron then either an Auger electron or a characteristic x-ray can be released[10,20]. Emitted characteristic x-rays have an energy equal to the difference between the shells of the given element. The closer the energy of the x- or γ-ray is to an absorption edge (which in XRF measurements are generally the K or L edges), the higher the probability of interaction[10,20,100]. A figure of the K- and L- absorption edges for strontium can be found in Figure 2 below.

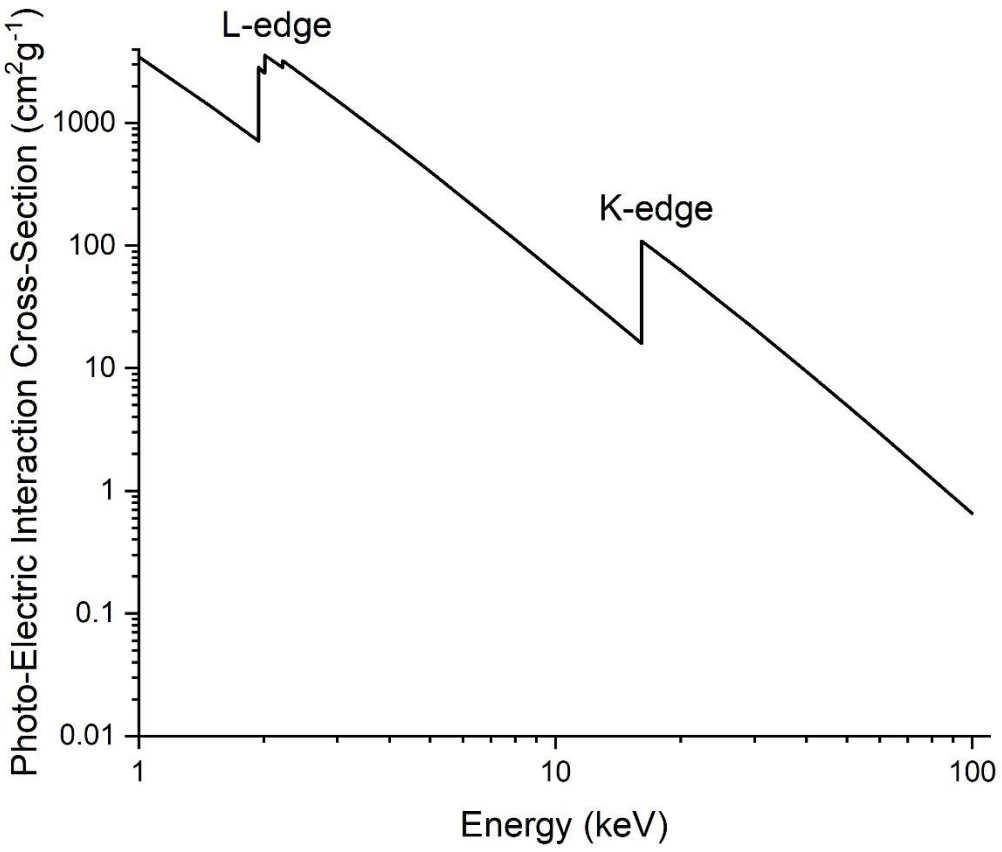

Figure 2: K- and L- edges of strontium. Data taken from NIST XCOM[7]

The proportion of de-excitations that result in emission of a characteristic x-ray rather than an Auger electron from a particular shell after a photoelectric interaction is given as[20]

$$\omega_k = \frac{N_k}{N_k + A_k} \quad (2)$$

$$\omega_k = \frac{Z^4}{Z^4 + a_k} \quad (3)$$

Where N_k is the number of X-rays released and A_k is the number of Auger electrons released. This can be further simplified by knowing that the probability of a radiative transition (release of a photon) is

proportional to Z^4. There is also a factor (a_k) which depends on the shell of the transition, for the K-shell the value is 1.12×10^6 for the L-shell it is 1.02×10^8.[10,20,43]

The rate at which x-rays of different energies are emitted from an atom are defined by the transition probability of one shell to the other, and the fluorescence yield and the probability of a photoelectric interaction[10,23,43].

Compton scattering occurs when an incident x- or γ-ray with energy Ey scatters off an electron, at an angle θ, transferring part of it's energy to the electron, resulting in a scattered photon of Ey'. This process generally considered to be independent of Z, and the cross section only depends on the electron density of the material, as well as the energy of the photon[10] . There is however a change in electron density with increasing Z[43]. Below the equation for the Compton scatter of a photon can be found:

$$E'_\gamma = \frac{E_\gamma}{1+\frac{E_\gamma}{m_e c^2}(1-\cos(\theta))} \quad (4)$$

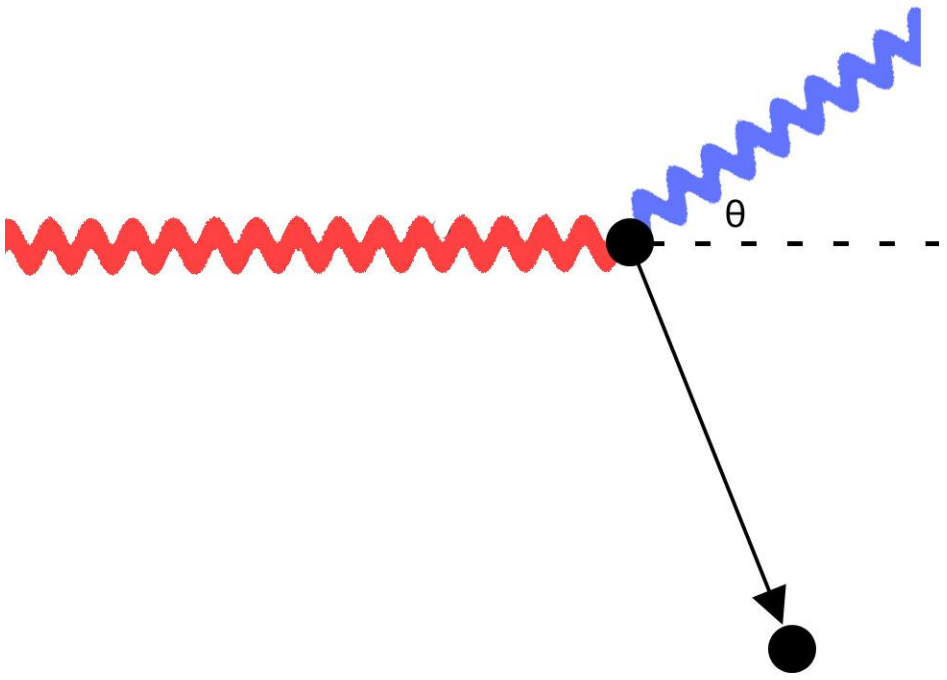

Figure 3: Diagram of Compton scattering off an electron in an arbitrary material. The incoming photon (red) with energy Ey scatters of an electron (black) at an angle theta, transferring some of it's energy to the scattered electron (black). As a result the photon loses energy, and has energy Ey'.[23]

Elastic scattering can be divided into multiple different scattering types. Rayleigh scattering is the elastic scattering of an incident photon with bound electrons, Thomson scattering is the elastic scattering of an incident photon with free electrons (and is also the classical limit of Compton scattering as hv tends towards zero[10], and Delbrück scattering is the elastic scattering of an incident photon with the Coulomb field of an atom[10,23,43]. In all three of these processes, the scattered photon changes direction, but does not lose any energy. Elastic scattering is dependent on Z, being proportional to Z^4 for energies of 0.1 MeV or less[23]. In this thesis work, Rayleigh scattering is the most dominant of these interactions and thus the term elastic scattering means Rayleigh scattering in subsequent sections of the thesis.

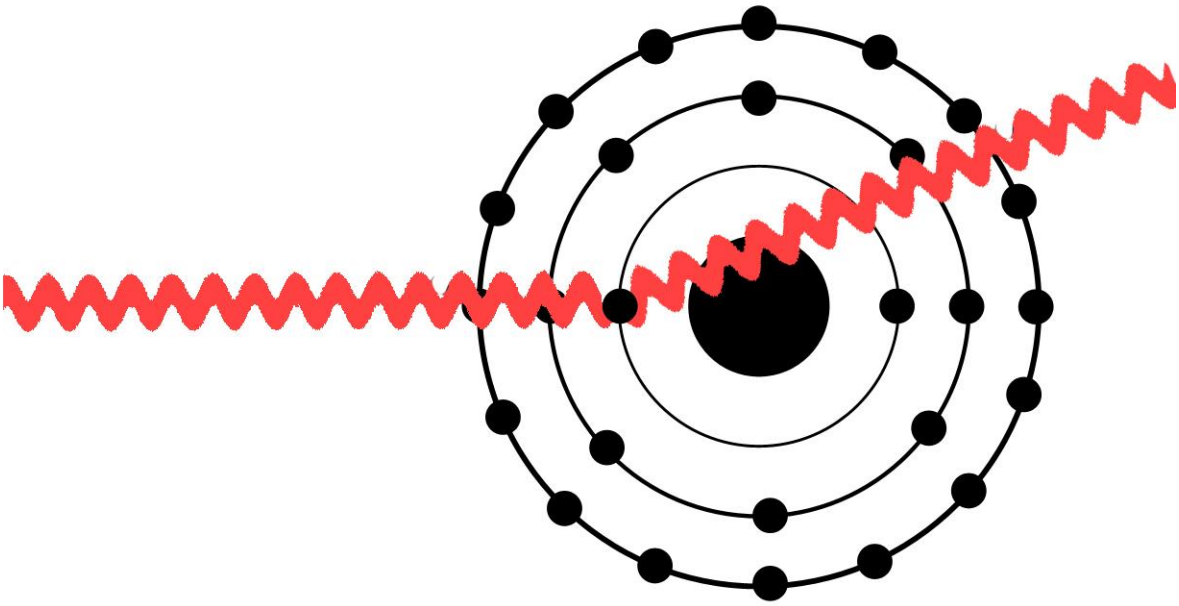

Figure 4: Diagram of coherent scattering. An incoming photon (red) of energy E, scatters off a bound electron of an atom, changing direction, but not losing any energy.

In an in vivo XRF measurement x- or γ-rays are used to irradiate, for example, a person's leg or finger. In bone, the photo-electric effect is the dominant interaction due to the relatively high average atomic number of bone when compared with soft tissue. Due to the strong dependence of elastic scattering on atomic number, elastic scattering interactions also primarily occur in bone, though at a much lower rate than photoelectric interactions; at an energy of 22.2 keV the photo-electric effect accounts for ~93% of total interactions in bone, and coherent scatter accounts for ~3.8% of interactions in bone. Compton scattering is the dominant interaction in soft tissue.

The x- or γ-ray interaction that permits the technique of XRF is the photoelectric effect.

1.1.3 History of in-vivo Strontium XRF:

A fuller overview of the history of strontium XRF can be found in Chapter 2 of this thesis. Briefly, in-vivo strontium XRF work was first performed in animal studies in the 1980s[88,101]. These early systems used a Si(Li) detector with either ^{109}Cd or ^{125}I being the source of fluorescing x- or gamma-rays. After a hiatus of approximately 20 years, work on in-vivo strontium XRF resumed in the early 2000s, utilizing a Si(Li) detector and either a ^{109}Cd[67] or ^{125}I[67,89] source. In-vivo pilot studies on women self-supplementing with strontium citrate with the same system, were performed in 2012[60] and 2014[61]. Other labs[82,91] have also measured strontium in-vivo using portable XRF guns with silver targets.

^{109}Cd decays via electron capture (EC) to the excited state of ^{109}Ag in 100% of decays. This excited state of ^{109}Ag de-excites to the ground state with the emission of an 88 keV γ-ray in 3.6% of transitions or undergoes internal conversion, resulting in the release of silver x-rays at 22.2 keV (18.7%), 24.9 keV (6.03%) and 25.5 keV (0.96%). A description of the ^{109}Cd sources used for this work is presented in the methodologies section below.

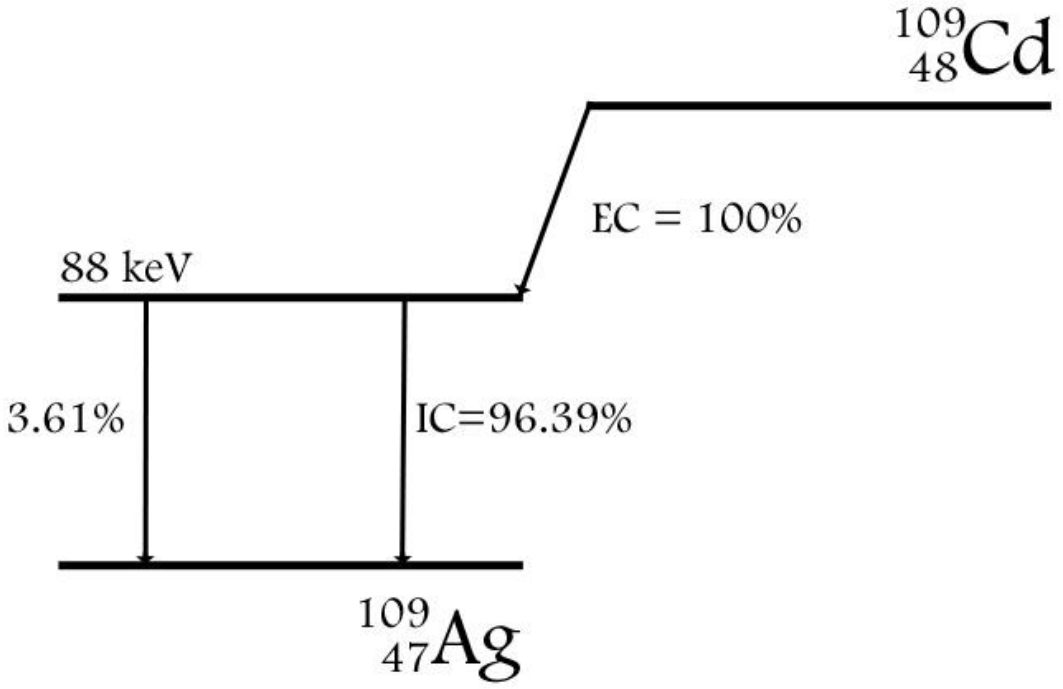

Figure 5: Decay scheme of ^{109}Cd. The half-life of ^{109}Cd is 462.6 days.

	Energy (keV)	Absolute Intensity (%)	Relative Intensity (%)
^{109}Cd	88	3.72[6]	3.61[37,67]
Ag X-rays	21.99 22.16 24.9 25.5	9.9[6] 18.7[6] 6.03[6] 0.96[85]	- 78[67] 16.7[67] -

Table 1: Absolute and relative intensities of emitted γ-ray and x-rays from the decay of ^{109}Cd. Note that because of the source encapsulation, the ratio of the emitted Ag X-rays to 88 keV γ-ray can change.

In a similar fashion to ^{109}Cd, ^{125}I decays via electron capture to an excited state of ^{125}Te. This excited state then de-excites to the ground state of ^{125}Te, with the emission of a 35.5 keV gamma in 6.68% of transitions or undergoes internal conversion with the emission of tellurium x-rays at 27.4 keV and 31 keV.

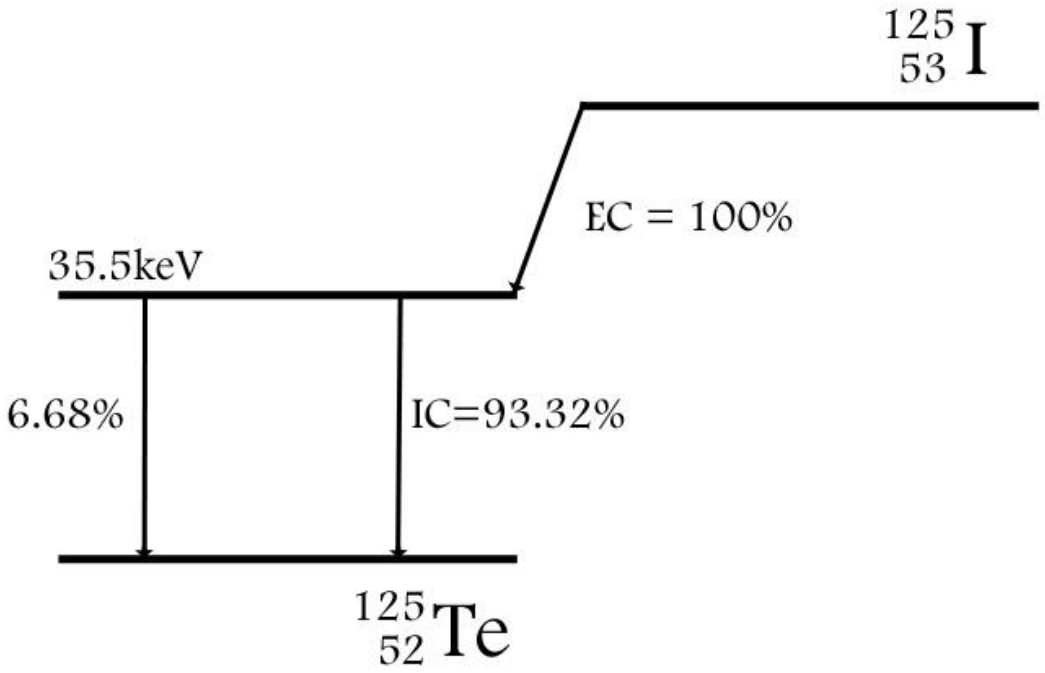

Figure 6: Decay scheme of ^{125}I, the half-life of ^{125}I is 60 days.

The ^{125}I seeds used in previous systems were IsoAid © sealed brachytherapy seeds (Model IAI-125A), consisting of ^{125}I adsorbed onto a silver marker of length 3.0mm and diameter of 0.5mm housed in a 0.05mm thick and 4.5mm long titanium capsule. Due to the silver in the capsule, the ^{125}I seeds thus also emit silver x-rays at 22.2 keV[62].

	Energy (keV)	Relative Intensity (%)
I-125	35.5	6.68
Te X-rays	27.4 31	59.5 14.43
Ag X-rays	22.2 24.9	17.56 16.66

Table 2: Relative intensities of emitted X- and y-rays from 125I. Included are the Ag X-rays from the silver present in the source capsule. Data taken from Zamburlini et al. 2007[89]

Most prior studies used ^{125}I in the form of brachytherapy seeds, likely due to them being lower cost and easy to obtain[28,60,61,89,97]. However, there are disadvantages to using ^{125}I as the fluorescing source compared to using ^{109}Cd when performing in-vivo strontium XRF measurements.

For ^{125}I, the Compton peaks observed in a backscatter spectrum are higher in energy than those of ^{109}Cd. They are thus less likely to result in background under the strontium K x-ray peaks. In addition the detector is transparent to the 88 keV γ-ray from ^{109}Cd, leading to a small contribution of dose for no additional signal. However, silver x-rays are also emitted which results in a more complicated spectrum, and the main disadvantage with the use of ^{125}I as a fluorescing source is the short half-life of 60 days. Sources must be purchased and replaced relatively frequently.

1.1.4 Phantom Materials

In order to properly test and calibrate in-vivo XRF systems there needs to be a reference standard that approximates the geometry and composition of potential measurement volunteers. In x-ray fluorescence work (and other wider medical Physics applications) these are referred to as phantoms. Phantoms are usually made of bone and soft-tissue equivalent materials and are doped with varying concentrations of the element under investigation. These phantoms are then used to calibrate the detector response to a known concentration, so that if in-vivo measurements are performed, the concentration of a given element in a person or unknown sample can be accurately quantified. These phantoms do not necessarily need to be exact anthropomorphic analogues to the region being investigated, but rather be close enough so as to approximate the given experimental setup geometry.

1.1.4.1 *Surrogates for bone*

Cortical bone makes , up to about 80% of the human bone mass by weight[36]. Cortical bone is composed of several components including mineral, collagen, water and non-collagen proteins, with the mineral making up the majority of bone mass by dry weight[4,36] . The bone mineral is primarily composed of calcium hydroxyapatite (HaP $Ca_5(PO_4)_3$), but also includes other compounds and elements such as

carbonate, magnesium, acid phosphates and a several trace elements including lead and strontium[4,36]. Bone matrix also contains collagen fibres, and 'cement' made of mucopolysaccharides and mucoproteins[36].

In the early development of measurement systems, bone phantoms for the calibration of *in vivo* strontium XRF systems were made of plaster of Paris (PoP). Plaster of Paris is commercially available and relatively easy to use. To make an element doped bone phantom, the desired concentration of strontium and water is added to the powder and thoroughly mixed, then allowed to set. However, there are several limitations to the use of PoP. In XRF systems used voifor bone lead measurements, use of coherent normalization requires a coherent conversion factor (CCF). Because of the chemical differences between plaster of Paris ($CaSO_4 \cdot H_2O$) and bone (mostly made of calcium hydroxyapatite ($Ca_5(PO_4)_3$), x- and γ-rays are coherently scattered differently by the two materials. This is mostly due to the fact that coherent scatter from sulphur is different than the coherent scatter from phosphorus.

The coherent conversion factor is the ratio of the differential scatter cross-section between plaster of Paris and bone at a given scattering angle and photon energy. Examples this factor has been employed include a coherent conversion factor of 1.46 for an 88 keV gamma from ^{109}Cd for measurements of lead[12] and gadolinium[98] and 1.3 for a 35.5 keV gamma from ^{125}I for measurements of strontium[59].

By far the largest disadvantage of using plaster of Paris as a bone equivalent material in strontium XRF measurements is the inherent strontium contamination. A summary of different materials reported as being used for phantoms for in vivo strontium XRF work can be found in Table 3 below, these illustrate just how hard it is to get plaster of Paris phantoms with low contamination. As can be seen the calcium hydroxyapatite phantoms created by Da Silva et al. in 2008 and 2013 were found to have an extremely low level of strontium contamination (<0.7 μgSr/gCa) compared to the contamination present with the most recent reported set of plaster of Paris phantoms (Moise et al. 2012 and 2014) having a

contamination level of 363 µg/g. Simulation studies by Da Silva et al. 2017[18] found that the differential scattering cross section for calcium hydroxyapatite phantoms at a photon energy of 35.5 keV was almost identical to that of cortical bone, eliminating the need for the coherent conversion factor. Experimentally phantoms may not be 100% pure calcium hydroxyapatite, as reactions may not occur and phantoms are instead being a mixture of starting reagents. However, this was determined to not be an issue as this study found that even in the extreme cases where the phantom is 100% calcium hydroxyapatite or 0% calcium hydroxyapatite (i.e. no calcium hydroxyapatite was formed during phantom creation) the differential coherent scatter cross sections were still extremely similar, differing by only 20%.

Paper	Phantom Material	Contamination (µgSr/gCa)
Pejovic-Milic et al. 2004	plaster of Paris	4080±80 – 5800±200 (k-α) 4400±100 – 6600±600 (k-β)
Specht et al. 2017[82]	Mowiol 4-88	74
Zhang et al. 2022[91]	Mowiol 4-88	74
Heirwegh et al. 2012[97]	plaster of Paris	453±9
Moise et al. 2012[60,62]	plaster of Paris	363
Moise et al. 2014[61,62]	plaster of Paris	363
Da Silva et al. 2008[16]	calcium hydroxyapatite	2.2±0.8
Da Silva et al. 2013[17]	calcium hydroxyapatite	<0.7

Table 3: Contamination levels in different phantom materials used to simulate bone for in-vivo strontium XRF measurements.

One downside, however, of calcium hydroxyapatite phantoms is that unlike plaster of Paris, they can decay over time into their base reagents. However, this is only observed for older phantoms, after approximately 7 years, meaning that this is not an issue with new phantoms[59].

1.1.4.2 *Surrogates for Soft Tissue*

3D printing is a versatile technique that can potentially be of use for low energy XRF measurements. It can permit the modelling and printing of anatomically correct[3,46] soft tissue phantoms that would be otherwise difficult to create. It is also relatively fast as the technique is reported as being able to print an

anatomically accurate thyroid phantom in approximately 45 minutes[3]. It has been widely applied, as discussed further below.

There are currently two types of 3D printers in existence: Fused Deposition Modelling (FDM) and Stereolithography (SLA)[25,26]. FDM printing works by extruding a thermoplastic filament (most commonly polylactic acid (PLA) or acrylonitrile butadiene styrene (ABS)) through a heated nozzle layer by layer to create an object[25,26]. FDM printers are more commonly used printers, and are good for simpler, larger object models[25,26]. SLA printers on the other hand work by curing (thus solidifying) resin layer by layer using a laser, making them good for more detailed, complex objects. However, a major drawback to SLA printers is after the part has been printed, the excess resin needs to be washed off and the object cured. This is not the case for FDM printers as they can be used once set, which is almost immediately after they have finished printing.

As stated above, the most common plastics used for 3D printing are PLA and ABS[52,53,54]. Other plastics used in 3D printing include polymethyl methacrylate (PMMA), Nylon and polyethylene terephthalate glycol (PETG)[52,53,54]. For low-energy photon measurements (<100 keV), it has been reported that the 3D printing plastics that best approximate soft tissue are PLA and PMMA[77,78,80,86]. It should be noted, however, that when working with 3D printed plastic as soft-tissue equivalents, that the composition, and thus mass attenuation coefficients, of the plastic can vary between manufacturers[80].

3 D printing has been used in medical physics for several applications. Various types of phantoms will be discussed below, however for the purposes of this thesis we only care about anthropomorphic phantoms that can approximate the experimental geometry. Examples include the creation of IMRT head phantoms[21], brain phantoms[66], and a phantom representing the X-ray of a neonate torso[38]. There are several studies where cylindrical phantoms made of PMMA were used for sample insertion in benchtop CT[2,5,15,19]. Studies have also used 3D printing to create molds for phantoms[29,81]. Other studies have

created hollow phantoms to approximate the thyroid[3,70] into which they were able to insert dosimeters, or iodine solution for imaging of the thyroid phantoms. A particularly interesting use of 3D printing was reported by Kiarashi et al.[46] who developed a breast phantom for mammography. They utilized an SLA printer to create two different phantoms, one with glandular structure and one without. Both phantoms were hollow and allowed for molten wax to be poured into the gaps in the phantom to simulate breast tissue. The phantom with glandular tissue was printed using two different kinds of resin, allowing for a more accurate approximation of a real breast and crushed eggshells were inserted into the phantoms to simulate micro-calcifications. 3 D printing has been used in XRF applications. For example, 3D printing was used to successfully print mouse phantoms to develop a system for in vi vivo measurements of lead in bone in mice, and phantoms that approximated the lattice of human bone were used to test the effects of lead micro-distributions in ^{109}Cd K XRF measurements of lead in the bones of young women[8,79].

Examples of studies employing 3D printed phantoms for low-energy x-ray measurements is presented in Table 4 below.

Papers	Type of Printer	Phantom	Material
Portararo et al. 2018[70]	FDM	Thyroid	PLA
Alssabbagh et al. 2017[3]	FDM	Thyroid	PLA
Deng et al. 2019[19]	FDM	CT	PMMA
Ahmed et al. 2018[2]	FDM	CT	PMMA
Bangash et al. 2022[6]	FDM	Skin	PLA
Kiarashi et al. 2015[46]	SLA	Breast	Resin
Sheehan 2022[79]	SLA	Bone Lattice	Resin
Bider et al. 2024[8]	FDM	Mouse Body	PLA

Table 4: Examples of studies that used FDM or SLA printers to print phantoms for low energy X-ray measurements.

1.1.5 Detectors for low-energy X-ray Fluorescence Measurements:

1.1.5.1 *The band gap and p-n junctions:*

In a given crystalline material, the crystal lattice structure has two energy bands that electrons can occupy. The upper energy band, referred to as the conduction band, contains electrons that are not

bound to the lattice structure of the material. They can move freely, contributing to the material's ability to conduct electricity. The lower energy band, referred to as the valence band, is the opposite: electrons are bound to the lattice structure[47].

Conduction band electrons contribute to electric field, and therefore the conductivity of the material.

The bands are separated by an energy gap called the band gap, the magnitude of which determines if the material acts as an insulator or semi-conductor. Conductors have no band gap, and electrons are able to move freely between the conduction and valence bands. However, for semi-conductors and insulators, only the valence band is populated with electrons. At room temperature, if the band gap is greater than 5 eV, then no electrons can be thermally excited to the conduction band, resulting in the material being labelled an insulator. If the band gap is approximately 1 eV, then thermal excitation of the lattice structure can result in electrons being excited to the conduction band, resulting in the material being labelled a semi-conductor. See Figure 7 below for a visual representation.

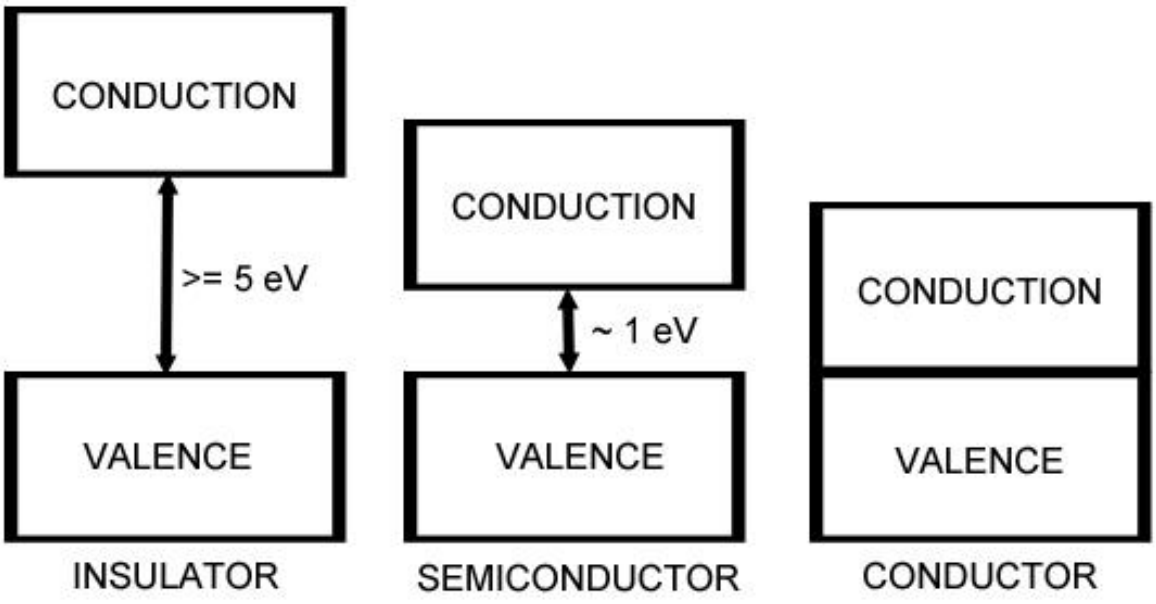

Figure 7: Energy band structure in insulators, semiconductors and conductors. Both insulators and semiconductors have a gap between the valence and conduction bands (called a band gap), with insulators having band gaps of less than or equal to 5 eV, and semiconductors having a band gap of approximately 1 eV.

Generally, semiconductors used for X-ray detection are made of germanium or silicon. As it is nearly impossible to create pure semiconductors from either material, they are doped with impurities to enhance their semiconducting properties. Impurities from Group V (e.g. phosphorus) result in extra electrons present in the material, while impurities from Group III (e.g. boron) result in extra holes. These are referred to as donor and acceptor impurities, and result in the creation of n-type and p-type semiconductors.

When an n-type semiconductor and p-type semiconductor come into contact, with no voltage bias applied, the holes from the p-type side migrate towards the n-type side and vice versa. When either the holes or electrons reach the opposite side, they cancel, resulting in a region with no charge. The migration of holes from the p-side and electrons from the n-side also results in a build up of net charge on either side of the junction (negative for the p-side and positive for the n-side) . This area of no charge is called the depletion region.

The build up of net charge on either side of the junction results in a potential difference (ϕ) given by[47]

$$\nabla^2 \varphi = -\frac{\rho}{\epsilon} \quad (5)$$

Where ρ is the net charge density, and ϵ is the dielectric constant of the semiconductor. This potential difference in turn results in an electric field being created over the depletion region. This electric field sweeps any electrons generated in the depletion region towards the n-type side of the junction, and any holes to the p-type side, resulting in the depletion region being void of any mobile charge carriers.

When a charged particle passes through the depletion region, it has a probability of causing ionizations and creating an electron-hole pair. This charge particle can be from either direct (i.e. from scattered Compton electrons) or indirect (i.e. a photoelectron from the photoelectric effect) action. The amount of energy it takes to create this electron-hole pair and is referred to as the ionization energy (w). This value is approximately 3 eV for silicon and germanium detectors.

1.1.5.2 *Reverse Biasing*

For practical radiation detection, the electric field described above is not strong enough and needs to be enhanced. To accomplish this, the detector is reverse biased, that is the p-type side of the junction is biased negatively compared to the n-type side. This not only enhances the already present electric field, but results in any holes created in the depletion region being swept across the junction towards the p-type side, resulting in a diode, where current flows freely in one direction, but not in the opposite direction. As the bias voltage is increased, the already present potential difference is enhanced, causing any holes from the p-side to cross further into the n-side and vice versa, resulting in the expansion of the depletion region[47].

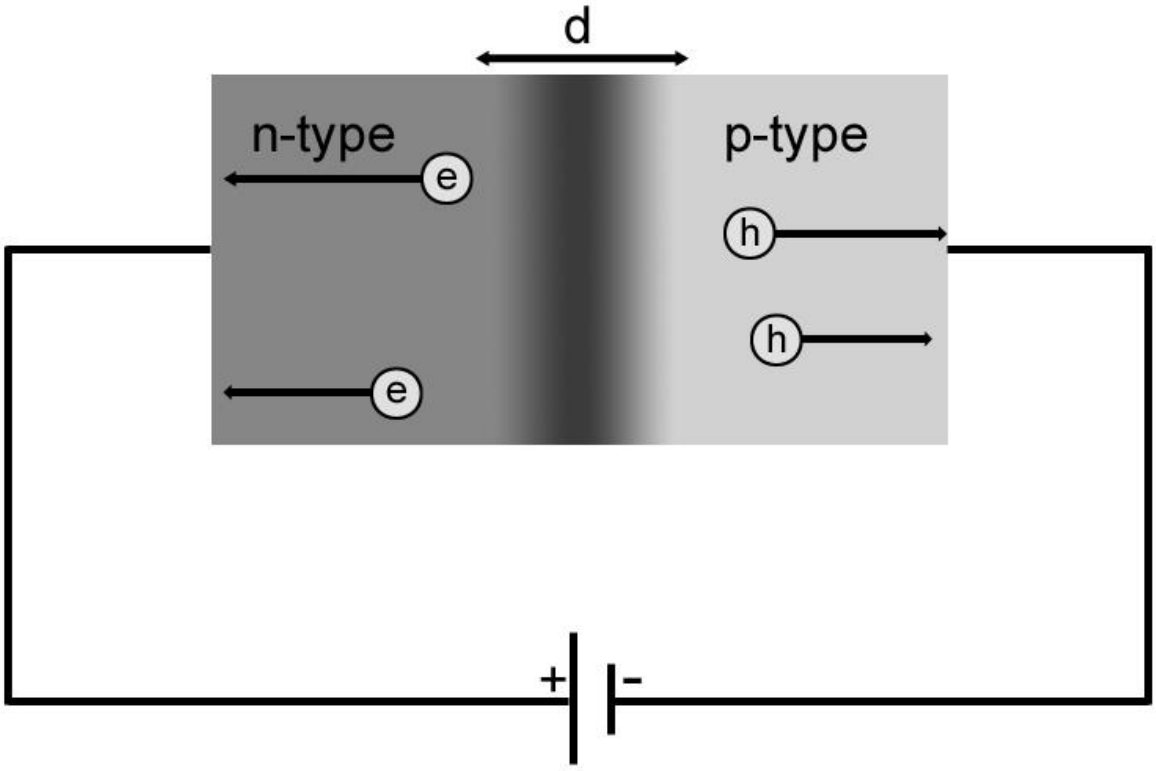

Figure 8: Diagram of a reverse-biased p-n junction, and growing depletion region. As the reverse bias voltage increases applied the width of the depletion region (d) grows.

1.1.5.3 *Noise and Leakage Currents*

The electric field that is applied to collect charge carriers is relatively high voltage and results in a small current (1 nA) being observed, which is known as the leakage current. Leakage currents are produced in one of two ways, bulk or surface. Bulk leakage currents are produced by thermal generation of electron-hole pairs and can only be reduced by cooling the detector to subzero temperatures. Surface leakage, on the other-hand, occurs at the edges of the p-n junction, due to the large voltage gradient in that location[37].

Both bulk and surface leakage currents contribute to the noise of the system (E_{bulk}, $E_{surface}$), which can lead to slower shaping times. In addition to the bulk and surface noise, the electrical contacts and resistances encountered in detectors can also introduce noise (called Johnson noise) to the system[47] .

$$(\Delta E_{noise})^2 = (\Delta E_{bulk})^2 + \left(\Delta E_{surface}\right)^2 + \left(\Delta E_{Johnson}\right)^2 \quad (6)$$

To reduce this noise, systems must be cooled to subzero temperatures through the use of a cryostat and LN_2 dewar or Peltier cooling.

1.1.5.4 *Energy Resolution and Full Width at Half Maximum (FWHM):*

The energy resolution of a semiconductor is affected by three independent processes: the noise from signal processing and any associated components (W_E), the leakage current of the detector as well as any issues with charge collection (W_X), and statistical fluctuations in charge generation ($W_D = 2.35^2 wFE$ where F is the Fano factor, E is energy of the particle, and w is the ionization energy of the material)[48].

$$W_T{}^2 = W_E{}^2 + W_D{}^2 + W_x{}^2 \quad (7)$$

1.1.5.5 *Shaping Time:*

The shaping time of a given detector influences how fast charges are able to be collected, and therefore how high a count rate the detector can handle. The shaping time is affected by two things: the charge transit time, and the plasma time. As plasma time is only relevant for heavy charged particle spectroscopy, it will not be discussed in this thesis.

The charge transit time of a detector is the time it takes for a given charge carrier created in the detector volume to migrate from where it was created to the collection anode. This is governed by the applied voltage, V, the thickness of the depletion region, d, and the mobility of charge carriers, μ.[47]

$$t_c = \frac{0.53d^2}{\mu V} \quad (8)$$

1.1.5.6 *Types of Semiconductor detectors*:

As stated previously, germanium and silicon are the two most common materials used for semiconductor detectors. For low-energy X-ray measurements, silicon detectors are the preferred choice despite silicon having a photo-electric interaction cross section that is approximately 50 times less than that of germanium at higher energies. At lower energies (<30 keV) the photo-electric effect is the dominant interaction of x-rays in both materials[47]. Because of the low energy of the x-rays, they are more likely to interact near the surface of the detector, resulting in the appearance of x-ray escape peaks in the collected x-ray energy spectrum. For germanium the fluorescence yield is 10 times higher than that of silicon, resulting in these escape peaks being much more prominent in spectra collected using germanium detectors[47]. In addition, the X-ray escape peaks for silicon appear at 1.7 keV, and unlikely to interfere with in vivo XRF measurements, while germanium x-ray peaks appear at 9.8 keV, which could interfere with features in some low energy XRF applications[47,85]. Silicon also has a larger band gap than germanium, resulting in lower thermally generated leakage current[47,48].

1.1.5.7 *Totally Depleted Detectors:*

If the bias voltage is raised so that the entire active region of the detector is depleted, the electric field becomes constant over the detector. This results in better charge transit times, and a reduction in Johnson noise[47,48].

1.1.5.8 *Silicon Detectors:*

One of the most popular types of silicon detectors for low energy XRF measurements is the lithium drifted silicon detector (Si(Li)). The result of drifting lithium onto the detector surface is the creation of a detector with a larger active thickness which increases the efficiency of the detector[47,48].

However, Si(Li) detectors have limitations. Because of fluctuations in the leakage current (due to the thickness of the detector), the detector needs to be cooled to subzero temperatures. In addition, the entire active volume of the detector is not used, which reduces the efficiency of detection of more penetrating radiation types[47,48].

While Si(Li) detectors are a good choice for low-energy XRF measurements, they are not the only type of silicon detector, and pose some disadvantages. A second popular type of silicon detector is the silicon drift detector (SDD). SDDs provide many advantages over Si(Li) detectors, which include their ability to handle higher count rates, their smaller physical size, and the fact that they are cooled using Peltier cooling instead of an LN_2 dewar and cryostat, resulting in a detector that is much smaller and more portable.

SDDs are able to achieve their higher maximum count rates (up to an input count rate of ~10^5 cps[50]) for two reasons: their smaller size results in a smaller charge transit time, and their lower detector and electrode capacitance results in less noise, and therefore a faster shaping time[27]. This results from the theory from which they were born: that of sidewards depletion. First proposed by Gatti and Rehak in 1984[102] , sidewards depletion is able to allow for an extremely low capacitance (120 – 250 fF[50,51]) and shaping time (<= 1μs)[48,50,51].

High-resistivity n-type silicon of thickness 300[50] – 450 μm[44] has boron implanted on the entirety of one side of the detector (acting as a p+ contact and entrance window), while the other side has concentric rings of p+ impurities implanted[24,49,50,51,84]. A shallow n+ contact is placed in the middle of the concentric

rings and acts as the collection electrode[49,50,51]. A constant potential is kept on the side with the boron implant, and the p+ rings are biased such that the outer ring is negative with respect to the n+ collection anode. An electric field is applied parallel to the surface of the detector, which results in a 'well' that funnels any electrons created in the depletion region towards the collection anode[48,49,50,51,73,74,75,102]. The depletion region propagates from the p+ regions, until the wafer is fully depleted. Because the depletion region propagates from both sides of the wafer, the voltage needed to achieve a fully depleted detector is reduced, further reducing leakage current and any noise. In addition, because the detector volume is totally depleted, this eliminates any Johnson noise, improving the energy resolution of the system, and again reducing the shaping time.

1.2 Methodologies

This thesis is a 'sandwich' thesis. That is, three papers for publication are presented in the form of a series of chapters. A disadvantage of this type of thesis is that some experimental details are not included in papers for publication. The following sections therefore provide a more detailed overview of procedures and materials used in Chapters 2, 3 and 4 of this thesis. In particular, the following sections describe challenges with the use of the Monte Carlo code MCNP6.2 for low energy x-ray fluorescence simulations, and a more detailed procedure of the creation of a set of 3D printed hydroxyapatite (HaP) phantoms. These sections also include a more detailed overview of the analysis of data presented in Chapters 3 – 5.

1.2.1 An Overview of 3D Printing

Materials for 3D printing were discussed in the prior section. As part of this thesis work, a set of phantoms were created to simulate human fingers. Phantom shells, designed to represent soft tissue, were filled with a strontium-doped bone surrogate. Phantom shells were printed on an Ultimaker 2 Extended FDM printer (Ultimaker) (see Figure 7) using PLA plastic filament from Overture. Unless

otherwise stated, all phantom shells were printed at 100% infill to ensure that the phantom walls were solid, and no air gaps were present in the plastic. Phantom shells were modelled by me in AutoDesk Inventor and were printed by S. Bangura and J. Bennett.

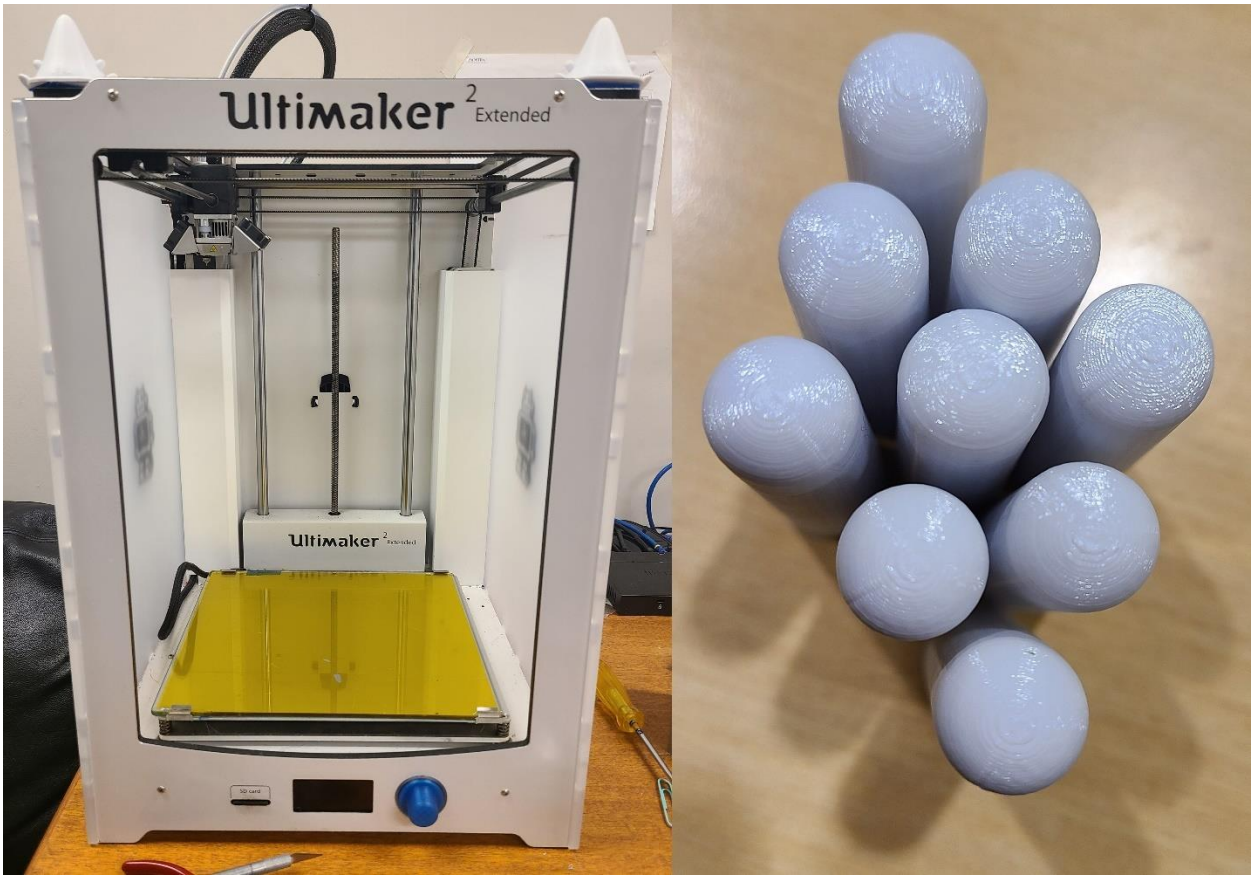

Figure 9: Ultimaker 2 Extended (left) used to 3D print all phantoms, source and phantom holders, and a set of 3D printed phantom shells (right).

1.2.1.1 *Mass attenuation coefficients of PLA plastic:*

Prior to phantom printing, the PLA was measured to determine whether it had a similar mass attenuation coefficient to that of soft tissue. This was required as although existing data suggested that PLA would be a good substitute for soft-tissue in terms of low-energy XRF[3,15,77], there can be variations in

the attenuation coefficients of the PLA dependent on the manufacturer[80]. It was decided therefore to confirm mass attenuation coefficients of the purchased PLA plastic at the outset.

In addition to phantoms shells, a 3D printed PLA source holder was modelled in AutoDesk inventor, and a lead collimator of 3mm thickness with a 1mm pinhole[8] was placed in front of the source. 3D printed PLA blocks (100% infill, printed previously by R. Bider[8]) of varying thicknesses (see Table 5) were placed in front of the detector between the source and detector.) Spectra were collected for 60s for each thickness.

Brick Number	Thickness (cm)
1	0.5
2	0.5
3	1
4	1
5	1
6	1
7	2
8	2

Table 5: Thicknesses of 3D printed PLA bricks used to measure mass attenuation coefficients of PLA plastic.

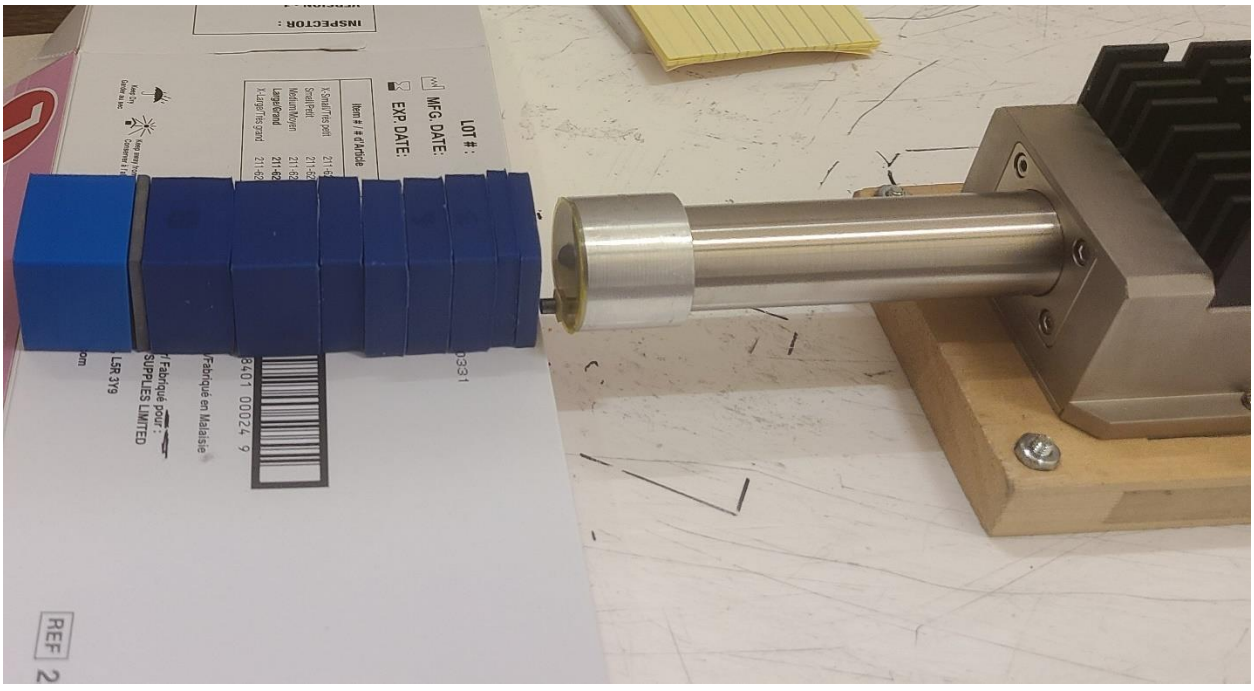

Figure 10: Experimental setup for attenuation measurements of PLA plastic. The light blue cube on the left hand side of the photo is the source holder, followed by the lead collimator, and the total thickness of PLA bricks. The source is pointed directly towards the detector face.

After data collection, the areas of the 22.2 keV, 24.9 keV and 25.5 keV silver X-rays for each thickness of PLA were calculated using OriginPro 2023. The 22.2 keV peak was fit as a single Gaussian on a linear background (EQ 9), while the 24.9 keV and 25.5 keV peaks were fit as a linked double Gaussian on a linear background (EQ 10).

$$G(x) = mx + b + Ae^{-\frac{(x-\mu)^2}{2\sigma^2}} \quad (9)$$

$$G(x) = mx + b + A_1 e^{-\frac{(x-\mu_1)^2}{2{\sigma_1}^2}} + A_2 e^{-\frac{(x-\mu_2)^2}{2{\sigma_2}^2}} \quad (10)$$

Where m is the slope of a linear background, b is the intercept, A is the amplitude of the Gaussian, μ is the position of the Gaussian and sigma is the width/standard deviation of the Gaussian. The peak areas were then calculated using EQ 11 below:

$$Area = \sqrt{2\pi} A\sigma \quad (11)$$

Where A is the amplitude of the peak, and sigma the standard deviation.

These areas were then plotted against the PLA thickness, and an exponential function was fit (EQ 12). The value of the linear attenuation coefficient, μ, was then extracted from this fit.

$$I = I_o e^{-\mu x} \quad (12)$$

Where I_o is the initial intensity of the radiation before going through the PLA, I is the intensity of the radiation amount of radiation after going through the PLA, and μ is the linear attenuation coefficient of

the PLA, and x is the thickness of the PLA. The source can be assumed to be a pencil beam due to the presence of the lead collimator, meaning build-up does not need to be taken into account.

These values were then compared with the tabulated mass attenuation coefficients from the National Institute of Standards and Technology Mass Attenuation Coefficient tables (NIST Standard Reference database 126[33]) for' ICRU 4 component soft tissue', and 'ICRU soft tissue'. Comparison was performed by calculating the percent difference between the measured and NIST (μ/ρ) values, and by calculating the difference in attenuation through 1cm of material. NIST values were converted from μ/ρ to μ by multiplying by the density of soft-tissue (1 g/cm^3). For full details of the results please see Chapter 2.

Energy	μ (cm^{-1})	R^2
22.2	0.83±0.08	0.98
24.9	0.72±0.07	0.98
25.5	0.70±0.07	0.98

Table 6: Calculated linear attenuation coefficients for 3D printed PLA plastic, and regression statistics for the fits shown in Figure 11.

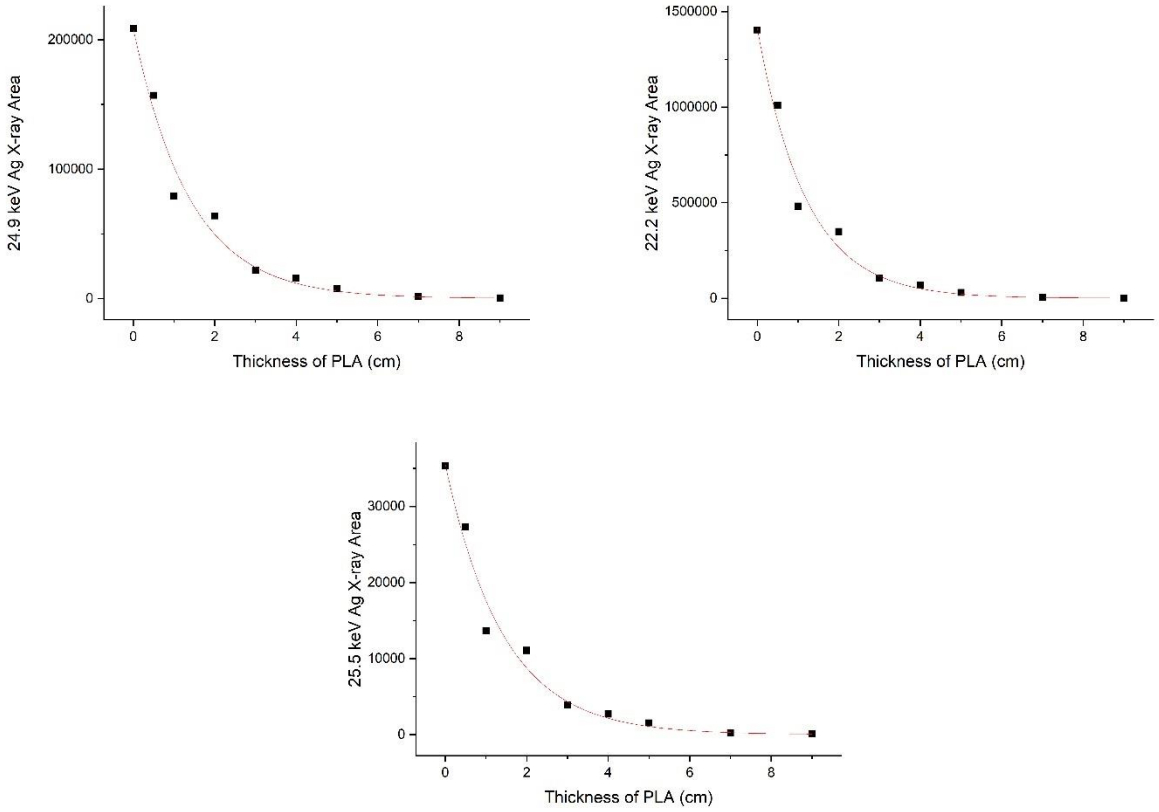

Figure 11: Graphs of attenuation of 22.2 keV (top left), 24.9 keV (top right) and 25.5 keV (bottom) Ag X-rays through 0 – 9cm of 3D printed PLA plastic.

1.2.2 Phantom Construction:

1.2.2.1 *3D Modelling of Phantom Shells:*

A preliminary phantom shell design (modelled by undergraduate student E. Davidson) was modified by me for the work in this thesis. Finger phantom shells consisted of a hollow core modelled by a tapered cylinder, with an overlay of soft-tissue, and a rounded cap at the top of soft-tissue to simulate the fingertip. The hollow core was filled with the bone-equivalent materials plaster of Paris or calcium hydroxyapatite. The outer-shell represents the soft-tissue of the finger being made of tissue equivalent material – in this case PLA. The dimensions were modified to the following: the inner diameter of the

hollow core at the top was changed to 7.5mm and to 9.7mm at the bottom. The length of the core was changed to 60 mm. The diameter of the outer shell was altered dependent on the desired thickness of soft tissue. The dimensions for each phantom are listed in the table below:

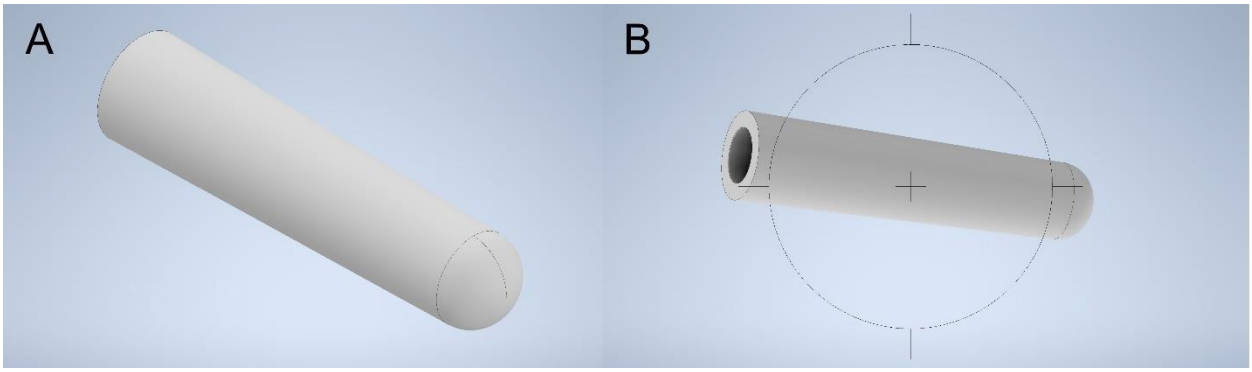

Figure 12: 3D models of phantom shells. Modelled in Autodesk Inventor.

Figure 13: Filled calcium hydroxyapatite 3D printed PLA phantoms.

Phantom PLA Overlay Thickness (mm)	Top Outer Diameter (mm)	Bottom Outer Diameter (mm)
2	11.5	13.7
2.5	12.5	14.7
2.9	13.3	15.5
3.5	14.5	16.7
4.0	15.5	17.7

Table 7: Dimensions of 3D printed PLA phantom shells, based on dimensions of human fingers from Pejovic-Milic et al. 2004[67]

For 0mm tissue thickness calcium hydroxyapatite phantoms and plaster of Paris phantoms, no overlay of PLA was required for measurements. A straight cylinder with PLA overlay thickness (outer diameter of 11.5mm, inner diameter of 7.5mm, 60mm long) was printed and used as a mould.

One set of phantoms were filled with strontium-doped calcium hydroxyapatite. A required amount of brushite ($CaHPO_4 \cdot 2H_2O$) was estimated and the required mass of calcium hydroxide ($Ca(OH)_2$) to add was calculated such as to keep the Ca/P molar ratio at 1.67. Finally, the volume of strontium stock solution was calculated based on the desired concentration of strontium and the molar mass of calcium present in the phantom materials. An example of the weights added for a set of phantoms is given in Table 8.

To create the calcium hydroxyapatite phantoms, the brushite (Sigma Aldrich) was measured into a clean beaker. The required mass of calcium hydroxide (VMR Lifesci) was added to the beaker and mixed by hand with a clean glass stir rod in order to ensure the mixture was homogeneous. The mass of reagents added was kept to within 1% of the theoretical value. A strontium stock solution of 10 mg/L strontium (Ultra Scientific) was added via micropipette to the beaker and mixed thoroughly with a glass stir rod until combined with the powder.

A setting solution of 1M sodium dibasic phosphate (NaH_2PO_4) was created by adding 1 to 2 spoonful of sodium dibasic phosphate powder (Sigma Aldrich) to approximately 250 mL of water. The mixture was stirred using a magnetic stir-plate until the powder had been completely dissolved in the water. The setting solution was added to the strontium phantom hydroxyapatite mixture by pipette until a frosting-like consistency was achieved. This was usually accomplished by the addition of 4 to 5 pipettes.

The mixture was then poured from the beaker into each phantom shell and tapped on the benchtop to pop any air bubbles. For the phantoms with no modelled soft tissue overlay, the bottom of the shell was sealed with a layer of masking tape to prevent leakage. The phantoms were then left to cure for one week. After a week the bottom of the phantoms were sealed with duct tape. After one week, the

phantoms with no soft tissue overlay phantoms were demolded. Unfortunately, likely due to a combination of un-popped air bubbles and the brittleness of the calcium hydroxyapatite, the phantoms broke when being demolded. To attempt to remediate this, the phantoms were wrapped in Kim wipes and secured with tape. The thinnest thickness of Kim wipes were used in order to produce minimal effects from the paper overlay.

Glassware was cleaned in between preparation of each phantom using deionized water and a sponge in order to ensure no cross-contamination. Phantoms were also created in order of lowest strontium concentration to highest strontium concentration in order to ensure any cross-contamination was minimal.

Phantom	Strontium Concentration (ppm)	Mass Brushite (g)	Mass $Ca(OH)_2$ (g)	Volume of strontium stock solution (µL)
S0	0	5.0000000	1.4423357	0
S1	25	5.0000000	1.4423357	5
S2	50	5.0000000	1.4423357	10
S3	100	5.0000000	1.4423357	19
S4	250	5.0000000	1.4423357	49
S5	500	5.0000000	1.4423357	97
S6	750	5.0000000	1.4423357	146
S7	1000	5.0000000	1.4423357	194
S8	1250	5.0000000	1.4423357	243
S9	1500	5.0000000	1.4423357	292

Table 8: Theoretical values of reagents for strontium doped calcium hydroxyapatite phantoms. Actual values used are summarized in Tables A.1 to A.6.

Plaster of Paris phantoms with no tissue overlay used the same phantom mould design as the calcium hydroxyapatite phantoms. Commercial plaster of Paris was mixed with water and varying concentrations of strontium solution. The mixture was then poured into each mould and allowed to cure for one week, at which point there was an attempt to de-mould the phantoms. However, during the curing process I hypothesize that the plaster became bound to the ridges of the PLA shells. This caused them to be

impossible to remove without destroying them. Therefore all plaster of Paris measurements were made with tissue overlay shells.

1.2.3 Experimental XRF system

The detector used in this work was a VITUS H150 Silicon Drift Detector (SDD) housed in an AXAS-M1 unit from KETEK GmBH. The power supply and signal processing unit was an AXAS-M2 also from KETEK GmBH. The AXAS-M1 houses the Peltier cooling, the detector and reset preamplifier, while the AXAS-M2 houses the temperature control and power supply. The detector has a maximum input count rate of 30 kcps at a rise time of 1 µs, and a FWHM of 136 eV at 5.9 keV. The detector was connected to a computer running GammaVision via an ORTEC DSPEC Plus spectrometer.

A cap and source holder previously designed for skin iron measurements[6] was placed on the detector for all measurements. The cap was made of aluminum, with a 250 µm thick styrene window and tantalum source holder on the bottom front of the face of the styrene. A comparison between detector parameters for the previous (Si(Li)) and new (SDD) detectors is summarized in Table 9 below.

	Ortec © Ametek-AMT Si(Li)	KETEK VITUS H150 SDD
Energy resolution at 5.9 keV (eV)	230	136
Deadtime (%)	30 – 50 (*in-vivo*) 15 – 30 (phantom)	2 – 5 (phantom)
Rise Time (µs)	10	1.6
Width/flat-top (µs)	0.80	0.3
Source Activity (MBq)	24	80 – 1000

Table 9: Detector parameters for a previously used in-vivo XRF Sr measurement system (Si(Li)) and the system discussed in this thesis (SDD). Both detectors used an ORTEC DSPEC Plus spectrometer for pulse processing.

1.2.3.1 *Radioisotope Sources:*

Two different ^{109}Cd sources of assumed identical fabrication (Source 1 and Source 2), but different source activities were used. The sources consisted of ^{109}Cd plated onto a 1mm diameter, 30 µm thick silver plug. The plug was contained in a 3mm x 3mm steel capsule with a 100µm Ti entrance window.

Source 1 had a reported activity of 5.59 GBq (in terms of the emission of 88 keV γ-rays) in February of 2016, and at the time of measurement in April of 2023 was 79.82 MBq. Source 2 had a reported activity of 4.995 GBq (in terms of the emission of 88 keV γ-rays)in 2020 and had an activity of 1.16 GBq in April of 2023.

Each source, when used in the system, was mounted in a tantalum source holder located on the bottom of the polystyrene window (see Figure 14) in a 180^{o} backscatter geometry. The phantom was then placed in a custom 3D printed phantom holder, at a distance of 1 to 2 mm from the source (see Figure 14). Each phantom was measured by the two different sources, for two live times: 300s and 1800s. Phantoms were measured 3 separate times, except for the calcium hydroxyapatite phantoms of concentration 0 µg Sr/ g Ca which were measured five times each. After each measurement, the phantom was moved and repositioned back to 2mm from the source. To ensure the accuracy of the repositioning only the phantom holder was moved, and the phantom was carefully placed back. The only phantoms not measured in the source holder were the ones with no soft tissue overlay as they could not stand upright.

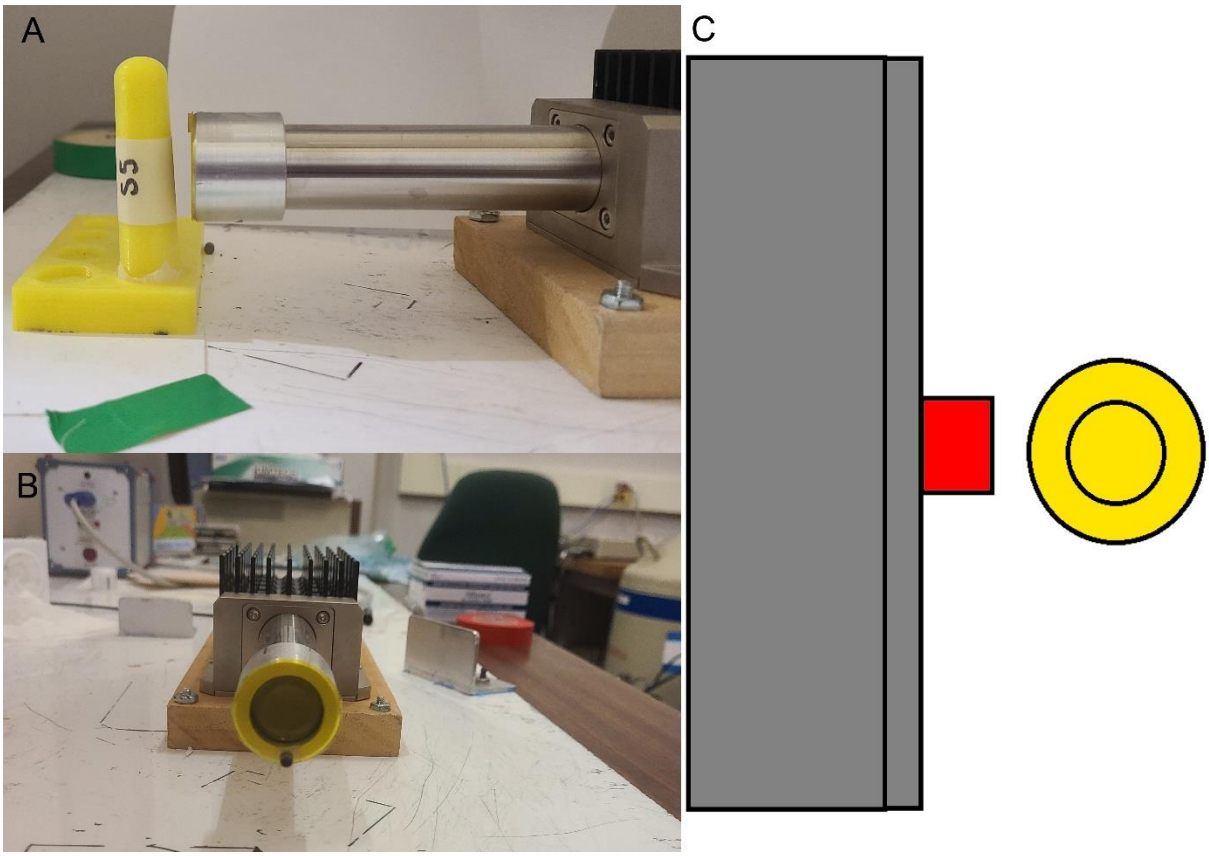

Figure 14: Photographs showing the experimental setup for the work in this thesis. A shows the phantom setup in the 180^{o} geometry, B shows the head-on view of the detector, and the position of the source holder at the bottom of the detector face. C shows a diagram of the top-down view of the detector and phantom, showing the phantom centered with respect to the source holder. Note that for C, grey is the detector, red is the source holder, and yellow is the phantom.

1.2.4 Data Analysis:

1.2.4.1 *Spectral Peak Fitting:*

X-ray signals were extracted from the measured spectra by fitting a mathematical model to the spectra. Peak fitting was performed exclusively using the batch-processing function of OriginPro 2023. Data were first extracted from the raw spectrum files and formatted for OriginPro using MATLAB. The following

procedures were used to fit the peaks for both the calcium hydroxyapatite and plaster of Paris phantoms.

Different parts of the spectrum were fitted using different functions. The strontium $K\alpha_{1,2}$ peak at 14.1 keV, the nickel Kα peak at 7.5 keV, the 22.2 keV coherently scattered silver X-ray and the 24.9 keV coherently scattered silver X-ray were empirically fit using a single Gaussian on a linear background (EQ 13).

$$G(x) = mx + b + Ae^{-\frac{(x-\mu)^2}{2\sigma^2}} \quad (13)$$

The strontium $K\beta_{1,3}$ peaks at approximately 15.9 keV, were fit using a double Gaussian on a linear background. However, the second $K\beta_2$ peak proved challenging to accurately fit. Therefore, only the fit to the more prominent $K\beta_{1,3}$ peak was used to calculate the area of the kβ.

$$G(x) = mx + b + A_1 e^{-\frac{(x-\mu_1)^2}{2{\sigma_1}^2}} + A_2 e^{-\frac{(x-\mu_2)^2}{2{\sigma_2}^2}} \quad (14)$$

The Compton scatter distributions arising from the 22.2 keV and 24.9 keV silver x-rays were each fit as a Voigt function on a background consisting of a complementary error function as shown in equation 5. (EQ 15). The function to use was determined empirically based on what function produced the best fit.

$$y = y_0 + \int_{-\infty}^{\infty}(f_1 * f_2)dx + erfc\left((x - x_c)/(\sqrt{2\pi}w_G)\right) \quad (15)$$

$$f_1(x) = \frac{2A}{\pi}\frac{w_L}{4(x - x_c)^2 + {w_L}^2}$$

$$f_2(x) = \sqrt{\frac{4\ln(2)}{\pi}} \frac{e^{-\frac{4\ln(2)}{w_G{}^2} * x^2}}{w_G}$$

Where A is the area of the peak, w_L is the width of the Lorentzian, w_G is the width of the Gaussian, x_C is the center of the Lorentzian.

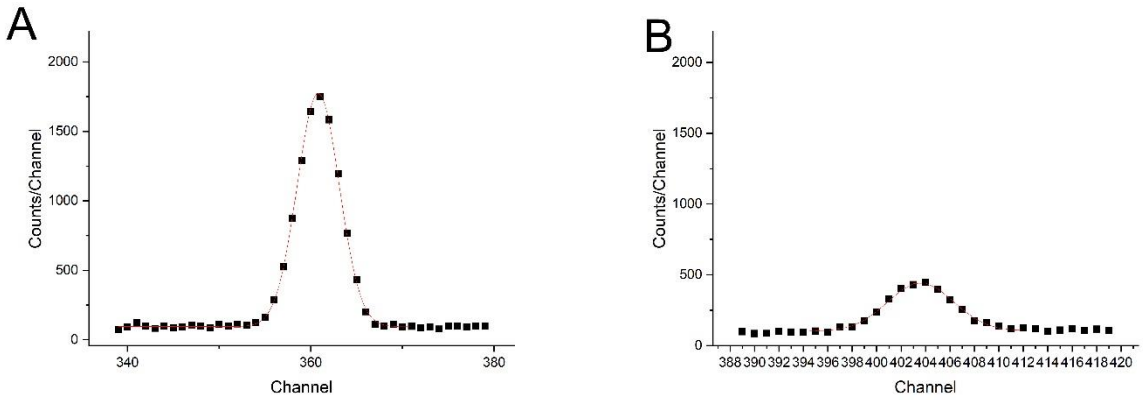

Figure 15: Fits for strontium Kα (A) and Kβ (B).

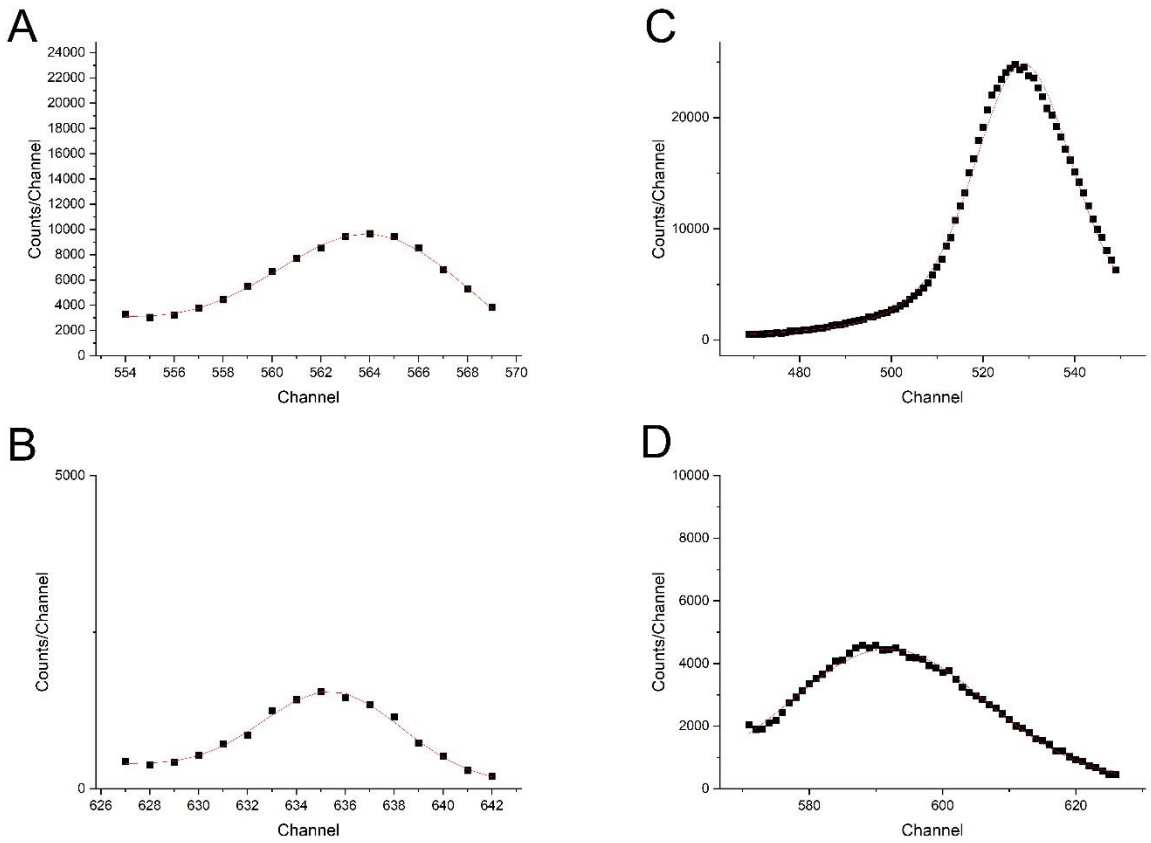

Figure 16: Fits of 22.2 keV coherently scattered Ag X-ray (A), 24.9 keV coherently scattered X-ray (B), 22.2

keV Compton scattered Ag X-ray (C) and 24.9 keV Compton scattered Ag X-ray.

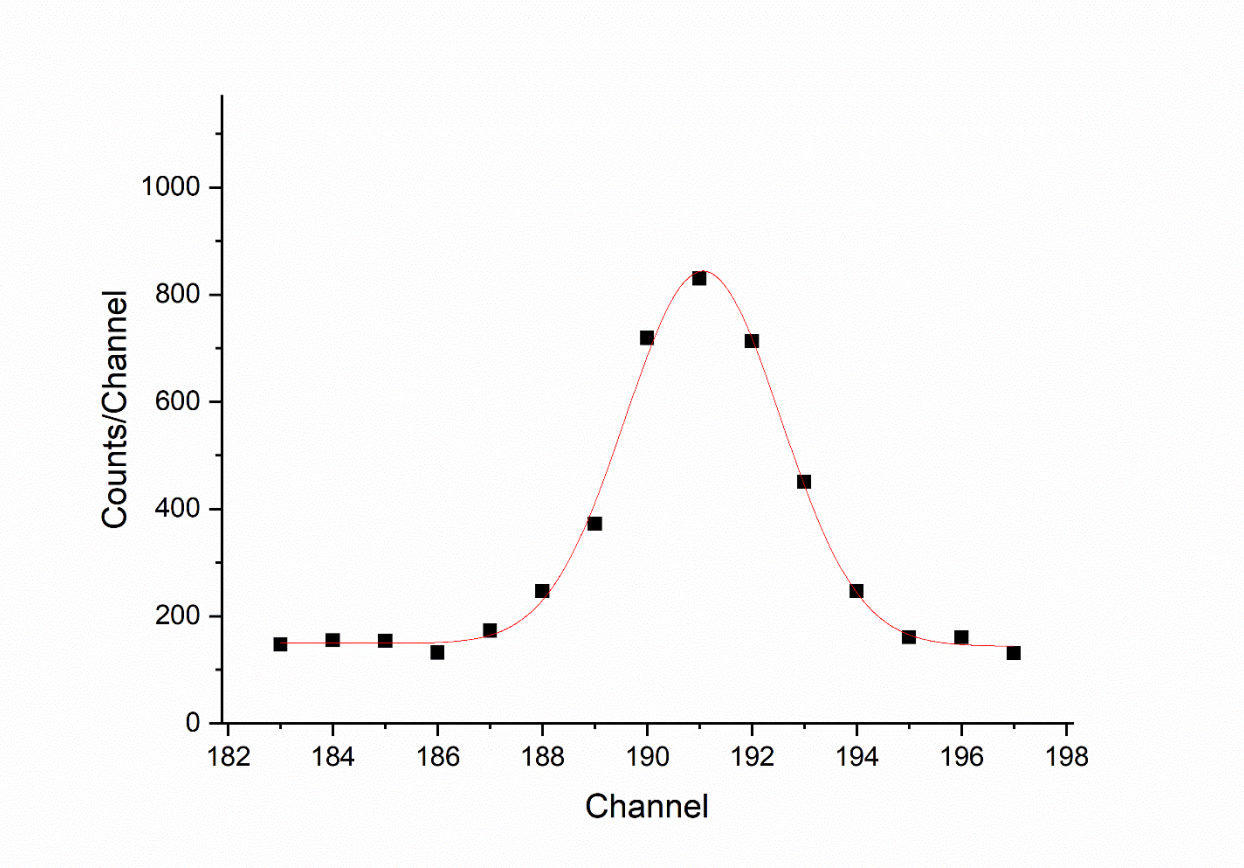

Figure 17: Fit of nickel Kα peak.

1.2.4.2 *Calibration Line and Minimum Detectable Limit Calculations:*

The goal of in vivo x-ray fluorescence is to quantify the elemental concentration of an unknown sample which in this case is a human finger. Quantification is performed by comparing the signal from the sample of unknown concentration with the signal from an appropriate calibration phantom. Calibration lines were created for this by plotting the peak areas of the strontium Kα peak and Kβ peak against the known concentration of each phantom. A linear function was fit to the data in OriginPro 2023.

The minimum detectable limit is the lowest concentration measured by the system that can be determined to be significantly greater than zero. In this work, MDLs for all calibration lines were

calculated by taken two times the uncertainty of the zero phantom (σ_o) and dividing by the slope of the calibration line as this has been the convention in publications from McMaster for several decades.

$$MDL = \frac{2\sigma_o}{slope} \quad (16)$$

MDLs were calculated for all phantom tissue overlay thicknesses, both sources and both measurement times.

1.2.4.3 *Estimates of Phantom Contamination:*

An estimate of the level of strontium contamination in phantoms was calculated from the calibration data. This can be calculated in two ways. It can either be calculated from the intercept of the calibration line or from the net Kα peak area of the 0ppm phantom. Estimates are divided by the by the slope of the calibration line to convert to units of μg Sr/ g Ca. This process was repeated for each source and time combination. The average of these values was then taken as the final overall contamination level of the phantoms.

1.2.4.4 *Plaster of Paris Contamination:*

At the outset of this work, calibration lines were created for a set of plaster of Paris phantoms. The data indicated an extremely high level of strontium contamination, and the calibration lines of Kα x-ray peak area versus concentration had extremely weak linear correlations (see Figure 18 and Table 10). Attempts were made to normalize the signals in the hopes of improving the fitting. Normalization was performed by dividing the strontium Kα and Kβ signals by a signal from nickel Kα x-rays and plotting the ratio against known phantom concentration. (This normalization had been performed in prior published work on iron x-ray fluorescence using this system.)[6] While the normalization to the nickel signal improved the calibration line fit significantly (see Table 10), it was felt that the level of contamination in the plaster of Paris phantoms was so high that reliable information could not be extracted as uncertainties were too

high. Work using plaster of Paris phantoms was therefore discontinued. This was unfortunate, as it did not allow for direct comparison of the performance of the system described in this work with earlier published data.

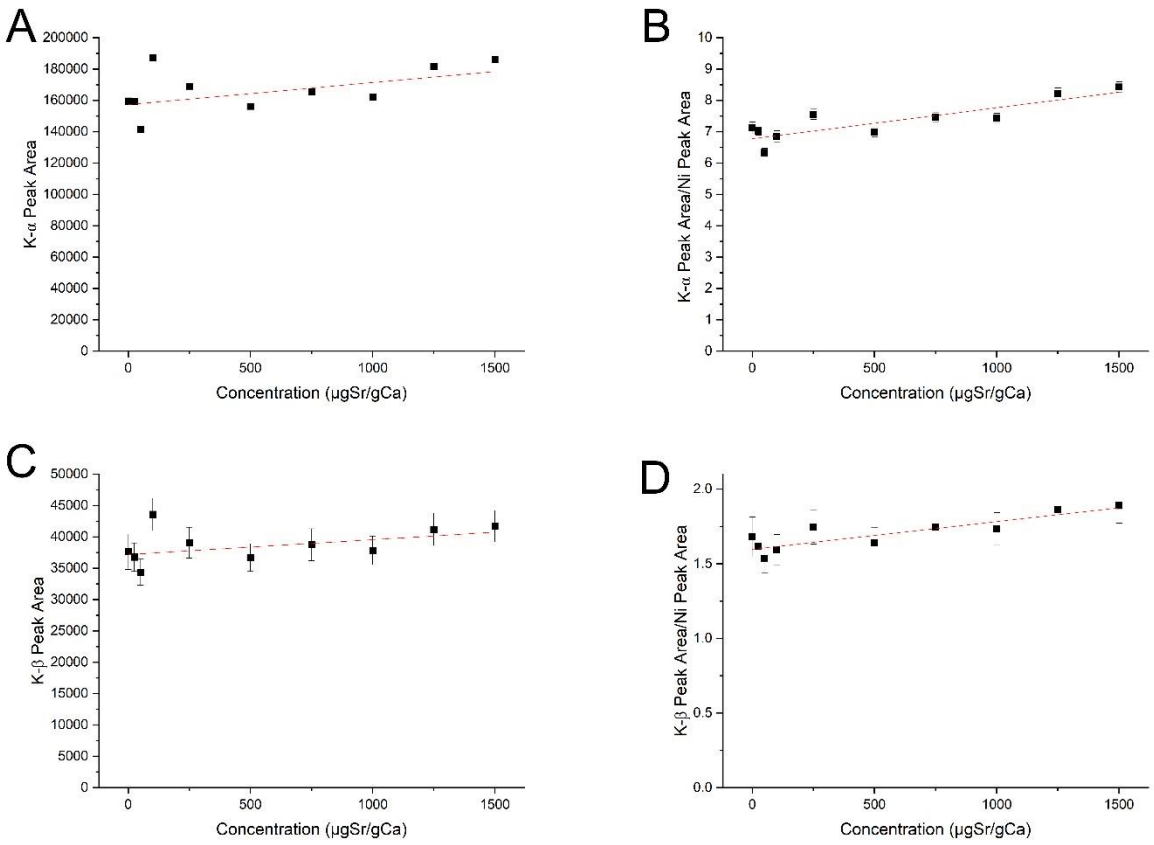

Figure 18: Calibration lines for plaster of Paris phantoms for a 30 minute measurement with Source 2. A shows the calibration of the strontium Kα peak, B the strontium Kα peak normalized to the nickel Kα peak, C shows the calibration of the strontium Kβ peak, and D shows the strontium Kβ peak normalized to the nickel Kα peak.

	Slope	Intercept	R^2
K-α	14.09±8.13	157274± 5820	0.18
K-α/Ni	(9.90±2.17)x10^{-4}	6.77± 0.16	0.69
K-β	2.37±1.61	37184± 183	0.12
K-β/Ni	(18.5±3.69)x10^{-5}	1.60± 0.03	0.73

Table 10: Slope, intercept and R^2 values for 30 minute measurements of plaster of Paris phantoms of varying concentrations of strontium (0 – 1500ppm) using source 2.

1.2.4.5 *Soft Tissue estimation using a Compton scatter correction*

A challenge in in vivo XRF measurements is that human beings come in a variety of shapes and sizes. In the case of measurements of the finger, this can mean different thicknesses of tissue overlying the bone. The soft tissue attenuates the x-ray signals, and if not accounted for, can mean strontium levels are underestimated.

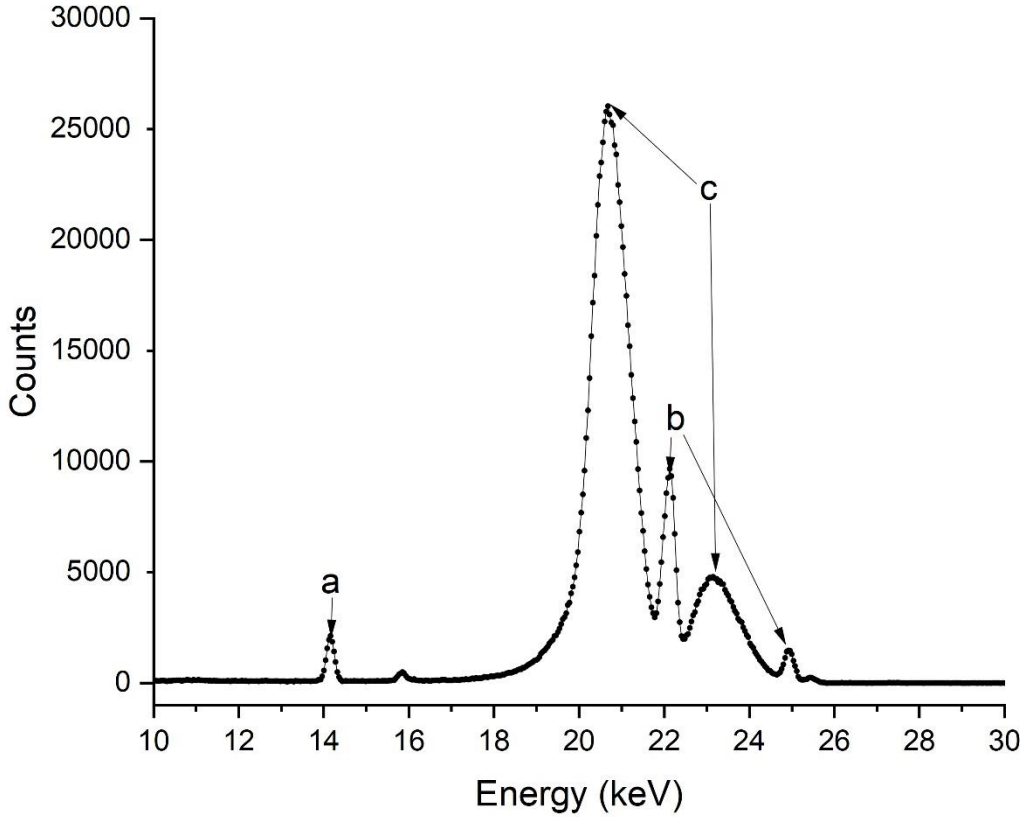

Figure 19: Spectrum for a 3D printed hydroxyapatite phantom with 2mm PLA overlay and concentration of 1500ppm. (c) is pointing to the strontium Kα peak, which gives the XRF signal. (b) is pointing to the coherently scattered Ag X-rays at 22.2 keV and 24.9 keV, which may be used to correct for changes in position. (c) is pointing to the Compton scattered Ag X-rays, which Gaevart and Chettle 2019[28] found to be able to estimate overlying soft-tissue thickness.

In 2019, Gevaert and Chettle[28] developed a procedure to estimate the overlay thickness in phantoms using the Compton scatter distributions of silver x-rays from the ^{109}Cd source. First the areas of the Compton scattered 22.2 and 24.9 keV silver x-rays were calculated for each overlay thickness (2.0mm – 4.0mm). The areas of the Compton scatter for the phantom with 0 overlay thickness were also calculated. This was done for each source strength and measurement time, and only for the 1500ppm phantoms average. The areas were then plotted against the overlay thickness for each energy, and a linear function was fit to each in Microsoft Excel to find the relationship between soft tissue thickness and Compton scatter. This process was repeated for each combination of source and measurement time.

A custom MATLAB script was used to calculate the estimated overlay thickness. Once the relation between the Compton scatter and overlay thickness was able to be estimated. The average area of each Compton peak was calculated for each concentration. The peak areas were then plugged into the corresponding equation based on the overlay thickness (e.g. for a 0ppm phantom with 2mm overlay, would use the 2mm equation) and solve for the overlay thickness. This was done for all concentrations, time and source combinations. The average of all these values were then taken.

The predicted value was then plotted against the known value of overlay thickness and a linear function was fit. To see if the slope was significantly different from 1, a Z-score was calculated.

$$Z = \frac{x-\mu}{\sigma} \quad (17)$$

Where x is the predicted value, μ=1, and σ is the error in x.

1.2.5 Monte Carlo Modelling:

First pioneered by S. Ulam and J. von Neumann in 1947, Monte Carlo modelling is a computational technique that utilizes random sampling in order to simulate radiation interactions in matter[95]. Monte Carlo simulations are useful in that they allow one to predict experimental results, without the labour involved in setting up experiments. Popular choices for Monte Carlo modelling software include MCNP (Monte Carlo Neutron Photon), maintained by Los Alamos National Laboratory in the US, and EGS5 (Electron Gamma Shower 5), maintained by the High Energy Accelerator Research Organization in Ibaraki, Japan. Both code packages allow the user to accurately simulate a variety of radiation interactions in matter ranging from Z=1 to Z=100. A brief overview of EGS5 and MCNP can be found below.

1.2.5.1 *Electron Gamma Shower 5 (EGS5):*

EGS5 is a general purpose FORTRAN based Monte Carlo code, maintained as an extension to EGS4 by the High Energy Accelerator Research Organization – KEK (Ibaraki, Japan). It allows the user to simulate radiation transport in materials ranging from Z=1 – 100. EGS5 introduced improvements to the photo-electric cross sections and to the angular distribution of bremsstrahlung radiation. The option to transport fluorescence photons is now integrated into the program, and it has been entirely rewritten in FORTRAN-77[31].

1.2.5.2 *Monte Carlo Neutron Photon 6 (MCNP6):*

MCNP6 is a general purpose Monte Carlo code maintained by Los Alamos National Laboratories (USA), and the latest iteration of the MCNP code package[87]. MCNP6 combines improvements from MCNP5 and

MCNPX[87]. Of import to our laboratory is the addition of coherent scatter cross sections above 60 degrees, and above 74 keV[34,35]. Doppler broadening has also been improved and turned on by default in the code[34,35].

Both MCNP6.2 and EGS5 were investigated as potential Monte Carlo codes for our simulations of the experimental system. The following section describes the process of attempting to benchmark both codes, as well as a myriad of issues found with MCNP6.2 in regards to low energy photon interactions.

1.2.5.3 *Initial Simulations in MCNP6.2*

Initial Monte Carlo models of the experimental system were performed using MCNP6.2. This initial model consisted of a detector modelled as a cylinder of silicon with a thickness of 450 μm and an area of 150 mm^2. The ^{109}Cd source was placed 1.5 cm from the detector face with its direction biased towards the phantom. A 25 μm Be window was also modelled 1.4mm in front of the silicon cylinder, and a styrene window of 0.25 mm. The phantom was modelled as a set of concentric cylinders with the intention of resemblance of a human finger. An inner cylinder was created to represent the bone with a length of 60mm and a radius of 5mm. An outer cylinder was created to represent the soft-tissue overlay and had a length of 60mm and a radius of 7.9mm resulting in a soft tissue overlay thickness of 2.9mm. Compton scatter, coherent scatter and doppler broadening were all switched to 'on' using the physics card. The energy deposited in the detector was calculated using the F8 tally and the FT8 tally was used to simulate broadening of the signal from the detector. A very high concentration of strontium in the bone was modelled as 5mg Sr/g Ca. The simulation was run for 9×10^9 particles.

An image of the spectrum obtained from the model is inserted below. While the coherent and Compton scatter of the 22.2 keV and 24.9 keV silver x-rays appear to behave as expected the magnitude of both the strontium Kα and Kβ peaks were significantly lower than expected. To investigate this further, further the composition of the 'bone' was replaced with pure strontium, and the soft tissue overlay, beryllium

window, and styrene window were removed. At this point, the model was switched to use the .12p library for MCNP6.2. Two other members of our research group had reported lower than expected x-ray signals in their models and switching to this library improved the simulations. The simulation was run for 1 x 10^6 particles. Despite these changes, the magnitude of the Kα x-ray and Kβ x-ray signals were still significantly lower than expected, being of the same order of magnitude as a 1500ppm strontium phantom.

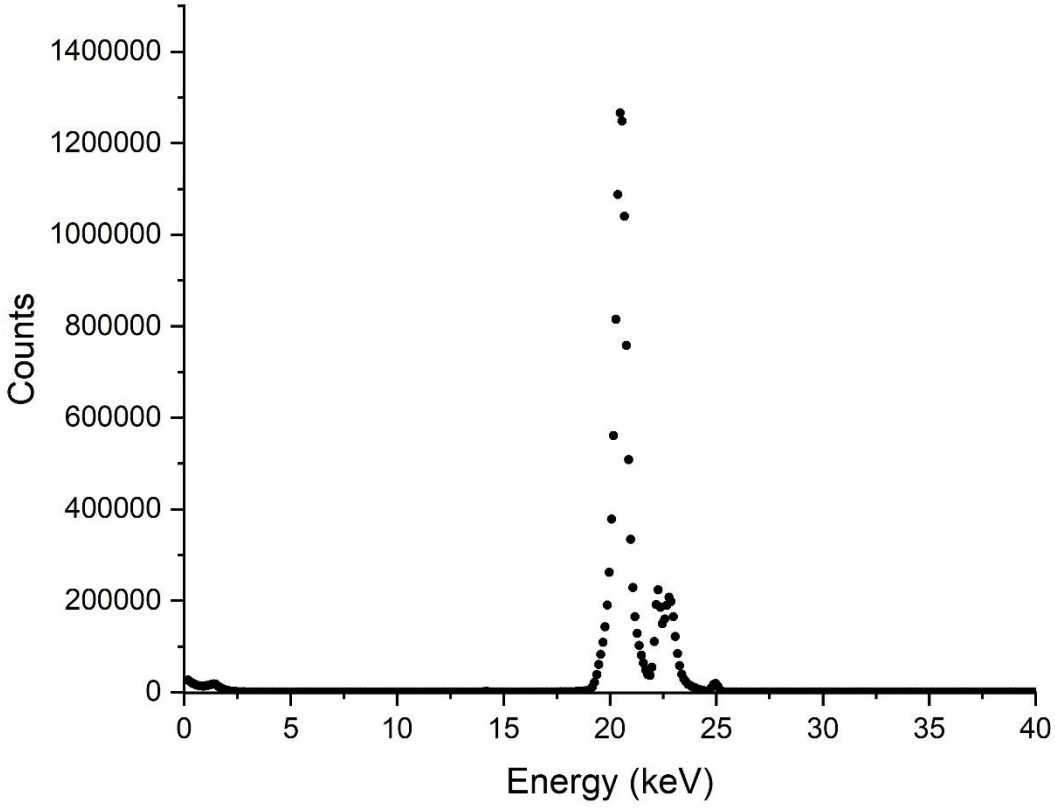

Figure 20: Spectrum for a 5mg/g strontium phantom with soft-tissue overlay using MCNP.

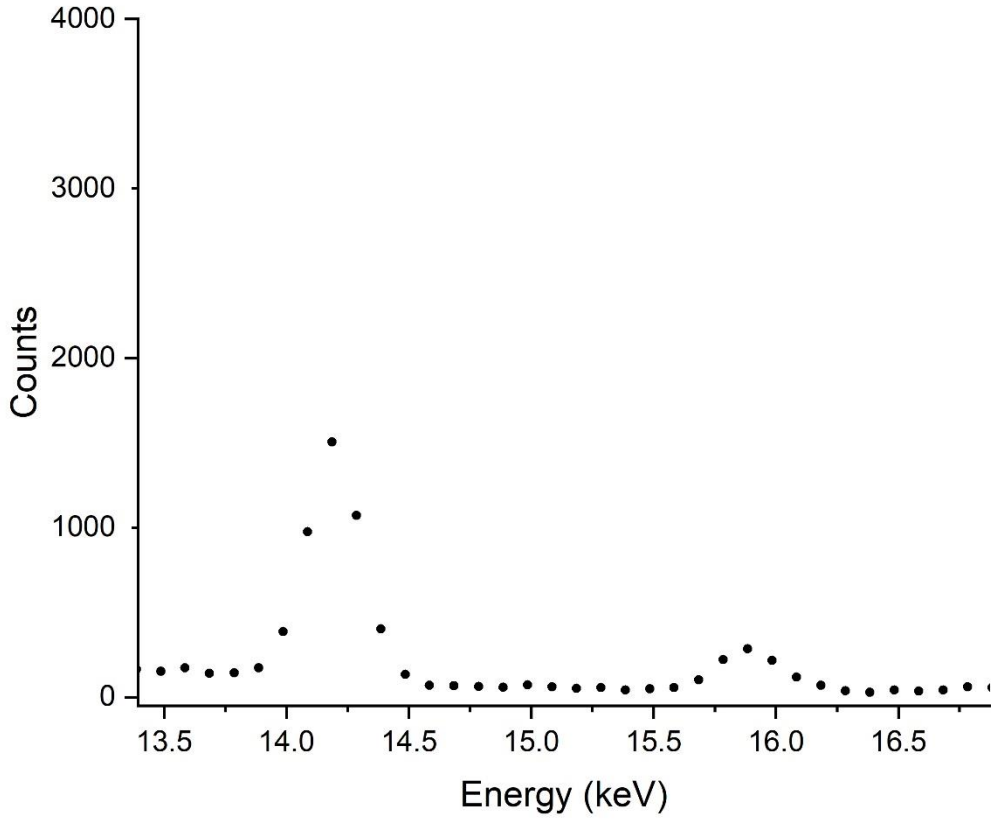

Figure 21: Strontium K-α and K-β peaks for a simulated MCNP

The cross-section data for photoelectric effect, coherent scatter, and Compton scatter for strontium that were being accessed by MCNP were investigated and compared to the values expected from an NIST Data Table[7]. It was found that the cross sections being used by MCNP were significantly different from those published by NIST. In particular the data for the coherent and Compton scatter off strontium in MCNP were substantially different from NIST values. Again, other members of our research group reported similar issues. Studies using MCNP6.2 for XRF measurements of lead in bone found x-ray cross-sections that were substantially different than NIST. Correspondence with MCNP code managers did not resolve the issue.

It was thus decided to discontinue use of MCNP6.2 and instead to perform simulations using EGS5.

1.2.5.4 Final Monte Carlo simulations in EGS5:

1.2.5.4.1 *Initial Simplified Model:*

As there had been fundamental problems with the application of MCNP 6.2 to low energy x-ray work, it was decided to perform initial simple tests using EGS5 to determine if the code could accurately create a simplified model of the detector and phantom setup. The model only contained the 450µm thick Si detector and 25µm thick Be window housed in a vacuum. The phantom was modelled as a cylinder with radius of 3.5mm and length of 60mm. Simulations were performed in EGS5 and run for a total of 1×10^7 particles.

The model performed better and after a promising start, the code was updated. The PLA plastic shell of the finger phantom was then modelled around a pure strontium phantom, with a cap of 0.5cm PLA on top of the phantom and tissue overlay thicknesses of 2mm, 2.5mm, 2.9mm, 3.5mm and 4.0mm.

The geometry of the detector was then updated based on manufacturer specifications. The nickel cap housing the detector was modelled as a cylinder with length 1.3615 cm and radius of 1.0000 cm with an internal vacuum surrounding the silicon detector of length 1.3600 cm and radius 0.7000 cm. Over this, an aluminum cap was modelled with length of 2.0000 cm and thickness of 0.1500 cm, with the 250µm thick styrene window (as used experimentally) placed in front.

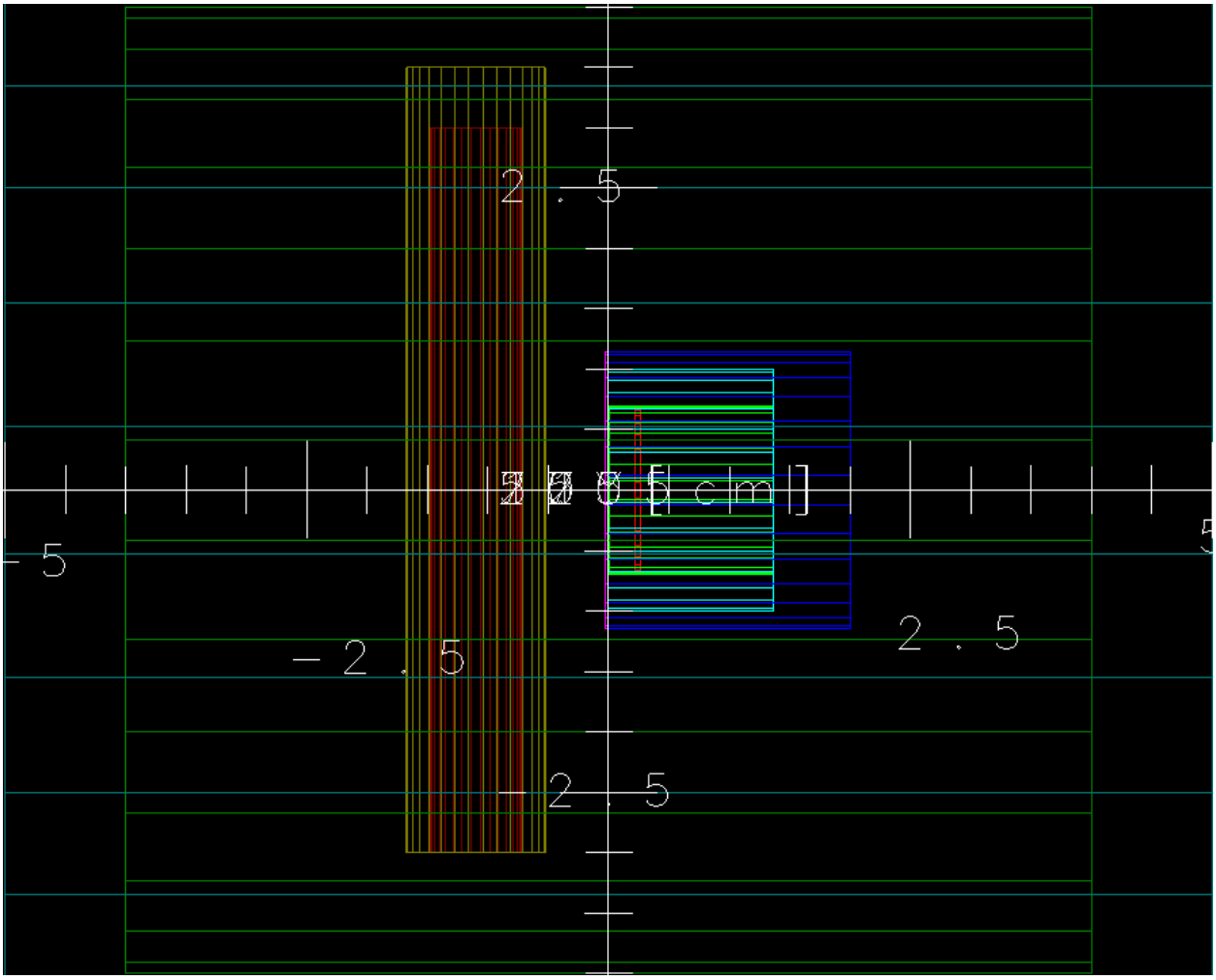

Figure 22: Schematic of simulated EGS5 geometry. The phantom presented has 2mm of PLA overlay thickness.

The air gap between the styrene window and detector face was not modelled as this was found to significantly increase the runtime of the code without improvements to the spectrum and interactions within the air were expected to be minimal. Similarly, the source was modelled as a unidirectional source pointed along the Z-axis towards to phantom. The source collimator and holder were not modelled as they increased runtime without providing substantial benefit to the observed spectrum. See Figure A.1 for the cards.

1.2.5.4.2 *Benchmarking:*

The accuracy of the simulation was determined by modelling phantoms with varying strontium concentrations corresponding to the values used in the real-world experiments. A phantom with a contamination level of 950 ppm strontium was run to simulate the inherent contamination of phantom material by strontium. The area of the strontium Kα peak for this phantom was then calculated, and added to already simulated phantom results.. The areas of the strontium Kα 22.2 keV and 24.9 keV coherently scattered silver X-rays were calculated from the simulated spectrum by summing the counts in each channel corresponding to the peak area and subtracting a linear background. The adjusted strontium Kα x-ray signal for each simulated concentration was then normalized to the 22.2 keV peak for each simulated concentration, plotted against the corresponding experimental result normalized to the 22.2 keV peak. A linear function was fit to the data to verify that the model and experimental results were correlated, and experimental results could be predicted from the model. This was repeated for each overlay thickness, source strength and measurement time to ensure the model and experiment matched for a variety of experimental conditions.

The simulation data were initially normalized to the Source 1 5 minute measurements. The area of the simulated strontium Kα peak was divided by the area of the experimental strontium Kα peak, to create a conversion coefficient (CF) between simulation and experiment. This was repeated for the 22.2 keV and 24.9 keV coherent scatter peaks. There was thus a methodology for converting simulation results to experimental prediction allowing the EGS model to be used to test potential future improvements to the system.

References

[1] Agency for Toxic Substances and Disease Registry (ATSDR). 2004. Toxicological profile for Strontium. Atlanta, GA: U.S. Department of Health and Human Services, Public Health Service.

[2] Ahmed, M., F., Yasar, S., and Cho S., H. "Development of an attenuation correction method for direct x-ray fluorescence (XRF) Imaging using gold L-shell XRF photons" *Medical Physics* vol 14, 12, 2018, pp 5543 – 5554

[3] Alssabbagh, M et al. "Evaluation of 3D printing materials for fabrication of a novel multi-functional 3D thyroid phantom for medical dosimetry and image quality" *Radiation Physics and Chemistry* vol 135 2017 pp 106-112.

[4] Primer on the Metabolic Bone Diseases and Diosrders of Mineral Metabolism, ASMBR, Wiley, 2008.

[5] Assemany et al. "Evaulation of 3D printing filaments for construction of a pediatric phantom for dosimetry in CBCT" *Radiation Physics and Chemistry* vol 167 2019.

[6] Bangash, S., U., K., McNeill, F., E., Farquarson, M., J., and Chettle D., R. "Feasibility of a 109Cd-based portable XRF device for measuring skin iron concentration in anaemic and beta-Thalassaemic patients" *Biomedical Physics and Engineering Express* vol 8, 2022, pp

[7] Berger, M.J., et al. (2010), *XCOM: Photon Cross Section Database* (version 1.5). [Online] Available: http://physics.nist.gov/xcom [2021, July 4]. National Institute of Standards and Technology, Gaithersburg, MD.

[8] Bider R., C., Sheehan, B., Bock, N., and McNeill, F., E. "The Feasibility of K XRF Bone Lead Measurements in Mice using 3D-Printed Phantoms" *Biomedical Physica and Engineering Express*. Vol , 2024.

[9] Blake, G., M. and Fogelman, I. "Effect of Bone Strontium on BMD Measurements" *Journal of Clinical Densitometry* vol 10, 1, 2007, pp 34 – 38.

[10] Elements of Nuclear Physics, Burcham, W., E. Longman. 1979

[11] Cardenas, D. et al. "Determining elemental strontium distribution in rat bones treated with strontium ranelate and strontium citrate using 2D micro-XRF and 3D dual energy K-edge subtraction synchrotron imaging" *X-ray Spectrometry*, vol 49, 2020, pp 424 – 433.

[12] Chettle, D., R. et al. "Lead in Bone: Sampling and Quantation Using K X-rays Excited by 109Cd" *Environmental Health Perspectives,* vol 91, 1991, pp 49 – 55.

[13] Chu, S., Y., F., Ekström, L., P., Firestone, R., B. "WWW Table of Radioactive Isotopes, database version" 1999, http://nucleardata.nuclear.lu.se/nucleardata/toi/

[14] Dahl et al. "Incorporation and Distribution of Strontium in Bone" *Bone.* Vol 28, no 4, pp 446 – 453, 2004.

[15] Dancewicz et al "Radiological properties of 3D printed materials in kilovoltage and megavoltage photon beams" *Physica Medica*. Vol 38 2017 pp 111-118.

[16] Da Silva, E., Pejovic-Milic, A., and Heyd, D., V. "The use of teeth as the site for the *in vivo* or *ex vivo* quantification of skeletal strontium by energy-dispersive X-ray fluorescence spectrometry: A feasibility study" *Journal of Analytical Atomic Spectrometry*, vol 23, 2008, pp 527 – 534.

[17] Da Silva E., Kirkham B., Heyd, D., V., and Pejovic-Milic A. "Pure Hydroxyapatite Phantoms for the Calibration of in vivo X-ray Flourescence Systems of Bone Lead and Strontium Quantification" *Analytical Chemistry* vol 85, 2013, pp 9189 – 9195

[18] Da Silva, E., and Pejovic-Milic, A., "Calibration of the ^{125} I-induced x-ray fluorescence spectrometry-based system of in vivo bone strontium determinations using hydroxyapatite as a phantom material: a simulation study" *Physiological Measurement*. vol. 38, no 6, 2017, pp 1077-1093.

[19] Deng, L. et al. "A detector's eye view (DEV)-based OSEM algorithm for benchtop x-ray fluorescence computed tomography (XFCT) image reconstruction" *Physics in Medicine and Biology* vol 64, 2019, pp

[20] X-rays in Atomic and Nuclear Physics, Dyson, N., A. Longman. 1973

[21] Ehler , E. et al "Patient Specific 3D printed phantom for IMRT quality assurance" *Physics in Medicine and Biology* vol 59 2014 pp 5763-5773.

[22] Protelos| European Medicines Agency" *European Medicines Agency* May 15 2020. https://www.ema.europa.eu/en/medicines/human/EPAR/protelos Accessed January 2024

[23] The Atomic Nucleus, Evans, R., D. McGraw-Hill. 1955

[24] Fiorini, C. et al "A new detection system for x-ray microanalysis based on a silicon drift detector with Peltier cooling" *Rev. Sci. Instrum.* Vol 68, 1997, pp 2461 – 2465

[25] "3D Printing Technology Comparison: FDM vs SLA vs SLS" *Formlabs* 2017a. Retrieved from: https://formlabs.com/blog/fdm-vs-sla-vs-sls-how-to-choose-the-right-3d-printing-technology/ accessed April 7 2020.

[26] "FDM vs SLA: Compare the Two Most Popular Types of 3D Printers" *Formlabs* 2017b. Retrieved from: https://formlabs.com/blog/fdm-vs-sla-compare-types-of-3d-printers/ accessed April 7 2020.

[27] Gatti, E., and Rehak, P. "Review of semiconductor drift detectors" *Nuclear Instruments and Methods in Physics Research* vol A541, 2005, pp 47 – 60

[28] Gevaert, J., and Chettle, D., R. "XRF analysis of strontium: Exploring cellulose as a soft tissue equivalent" *X-ray Spectrometry*, vol. 2019, no. 48, pp 443-451.

[29] Hazelaar et al. "Using 3D printing techniques to create an anthropomorphic thorax phantom for medical imaging purposes" *Medical Physics* vol 45 no 1 pp 92-100.

[30] "Strontium in drinking water – Guideline Technical Document for Public Consultation" *Health Canada* July 20 2018 https://www.canada.ca/en/health-canada/programs/consultation-strontium-drinking-water/document.html Accessed January 2024

[31] Hirayama, H., Yoshihito, N., Bielajew, A., F., Wilderman, S., J,., and Nelson, W., R. The EGS5 Code System. SLAC-R-730. 2005.

[32] Hubbell, J., H., and Overbo, I. "Relativistic Atomic Form Factors and Photon Coherent Scattering Cross Sections" *J. Phys. Chem, Ref, Data* vol 8, no 1, 1979 pp 69 – 105

[33] Hubbell, J. H., and Seltzer, S., M. "NIST standard reference database 126" *X-ray Mass Attenuation Coefficients,* 2004.

[34] Hughes, H. Grady. "Enhanced electron-photon transport in MCNP6." In *SNA+ MC 2013-Joint International Conference on Supercomputing in Nuclear Applications+ Monte Carlo*, p. 03105. EDP Sciences, 2014.

[35] Hughes, G. "Recent developments in low-energy electron/photon transport for MCNP6." *Progress in Nuclear Science and Technology*, vol 4, 2014: 454-458.

[36] ICRP, 1975. Report of the Task Group on Reference Man. ICRP Publication 23. Pergamon Press, Oxford.

[37] International Atomic Energy Agency (IAEA) "Live Chart of Nuclides" Livechart – Table of Nuclides – Nuclear structure and decay data, 2023, https://www-nds.iaea.org/relnsd/vcharthtml/VChartHTML.html Accessed April 2024

[38] Irnstorfer, N. et al. "An anthropomorphic phantom representing a prematurely born neonate for digital x-ray imaging using 3D printing: Proof of concept and comparison of image quality from different systems" *Scientific Reports*. Vol 9 2019.

[39] "Bone Densiometry" *Johns Hopkins* https://www.hopkinsmedicine.org/health/treatment-tests-and-therapies/bone-densitometry Accessed March 2024

[40] "Osteopenia 101"*Johns Hopkins*, April 23 2007 https://www.hopkinsarthritis.org/ask-the-expert/osteopenia-101/ accessed May 2024

[41] Bellatoni, M., F. "Osteoporosis Information" *Johns Hopkins* https://www.hopkinsarthritis.org/arthritis-info/osteoporosis-info/ accessed May 2024

[42] "Osteoporosis" *Johns Hopkins* https://www.hopkinsmedicine.org/health/conditions-and-diseases/osteoporosis accessed May 2024

[43] Nuclear Physics, Kaplan, I. Addison-Wesley Publishing. 1962

[44] Ketek GmBH. VITUS Silicon Drift Detectors User's Manual. Munich: 2012.

[45] Khan, F. M., & Gibbons, J. P. (2014). *Khan's the physics of radiation therapy*. Lippincott Williams & Wilkins.

[46] Kiarashi et al. "Development of realistic physical breast phantoms matched to virtual breast phantoms based on human subject data" *Medical Physics* vol 42, no 7. 2015 pp 4116-4126.

[47] Radiation Detection and Measurement, Knoll, Glenn, F. John Wiley & Sons. 1979.

[48] Radiation Detection and Measurement, Knoll, Glenn, F. John Wiley & Sons. 2010.

[49] Lechner, P., et al. “Silicon drift detectors for high resolution room temperature X-ray spectroscopy” *Nuclear Instruments and Methods in Physics Research A* vol 377, 1996, pp 346-351.

[50] Lechner, P., et al. “Novel high-resolution silicon drift detectors” *X-Ray Spectrometry* vol 33, 2004, pp 256-261.

[51] Leutenegger, P., et al. “Silicon drift detectors as radiation monitor for x-, gamma rays and particles” *X-ray Optics, Instruments and Missions III* vol 4012, 2000 pp 579 – 591

[52] “MakerBot ABS: Production-Grade Real ABS for manufacturing Applications | MakerBot” *MakerBot* Retrieved from: https://www.makerbot.com/3d-printers/materials/method-abs/ accessed April 7 2020.

[53] “3D Printing Materials|MakerBot” *Makerbot* Retrieved from: https://www.makerbot.com/stories/design/3d-printing-materials/ accessed April 7 2020.

[54] “PLA vs ABS vs nylon” *MarkForged* Retrieved from: https://markforged.com/resources/blog/pla-abs-nylon accessed April 7 2020.

[55] “Bone health: Tips to keep your bones healthy” *Mayo* Clinic, 2022. Retrieved from: https://www.mayoclinic.org/healthy-lifestyle/adult-health/in-depth/bone-health/art-20045060 Accessed March 2024.

[56] McNeill, F., E., et al. “Factors affecting *in vivo* measurement precision and accuracy of 109Cd fluorescence measurements” *Physics in Medicine and Biology*, vol 44, 1999, pp 2263-2273.

[57] Meunier, P. J., D. O. Slosman, P. D. Delmas, J. L. Sebert, M. L. Brandi, C. Albanese, R. Lorenc et al. "Strontium ranelate: dose-dependent effects in established postmenopausal vertebral osteoporosis—a 2-year randomized placebo controlled trial." *The Journal of Clinical Endocrinology & Metabolism* 87, no. 5, 2002, pp 2060-2066.

[58] Meunier P. J., Roux C., Seeman E., Ortolani S., Badurski J. E., Spector T. D., Cannata J., Balogh A., Lemmel E. M., Pors-Nielsen S., Rizzoli R., Genant H. K., and Reginster J. Y. “The Effects of Strontium Ranelate on the Risk of Vertebral Fracture in Women with Postmenopausal Osteoporosis” *New England Journal of Medicine* vol 350(5), 2004 pp 459-468.

[59] Micsa, M. et al. “Long-term stability of hydroxyapatite bone phantoms for the calibration of in vivo x-ray fluorescence spectrometry-based systems of bone lead and strontium quantification” *Biomedical Physics Engineering Express* vol 10, 2024,

[60] Moise, H., et al “Monitoring bone strontium levels of an osteoporotic subject due to self-administration of strontium citrate with a novel diagnostic tool, in vivo XRF: A case study” Bone vol 51, 2012, pp 93-97.

[61] Moise, H., et al. “Monitoring bone strontium intake in osteoporotic females self-supplementing with strontium citrate with a novel *in-vivo* X-ray fluorescence based diagnostic tool” *Bone* vol 61, 2014a, pp. 48-54.

[62] Moise, H. Energy Dispersive X-ray Fluorescence Spectrometry and Kinetic Modeling of Elemental Strontium in Human Bone. 2014. McMaster University, PhD.

[63] Nielsen, S., P. “The biological role of strontium” *Bone*, vol 35, 2004, pp 583 – 588.

[64] "Strontium ranelate (Protos) for postmenopausal osteoporosis" *NPS MedicineWise* November 1 2007. https://www.nps.org.au/radar/articles/strontium-ranelate-protos-for-postmenopausal-osteoporosis Accessed January 2024

[65] Oliviera, J., P. et al. "Strontium is incorporated in different levels into bones and teeth of rats treated with strontium ranelate" *Calcified Tissue International,* vol 91, 2012, pp 186 – 195.

[66] Pardo et al. "3D printing of anatomically realistic phantoms with detection tasks to assess the diagnostic performance of CT images" *European Radiology*. Vol 30 pp 4557-4563.

[67] Pejovic-Milic, A., et al. "Quantification of bone strontium levels in humans by *in vivo* x-ray fluorescence" *Medical Physics* vol 31, no 3, 2004, pp 528-538.

[68] Pemmer, B. et al. "Spatial distribution of the trace elements of zinc, strontium, and lead in human bone tissue" *Bone*, vol 57, 2013, pp 184 – 193.

[69] "Osteoporosis and related fractures in Canada: Report from the Canadian Chronic Disease Surveillance System 2020" *Public Health Agency of Canada* February 2024https://www.canada.ca/en/public-health/services/publications/diseases-conditions/osteoporosis-related-fractures-2020.html Accessed February 2024

[70] Portararo A., et al. "Evaluation of the dose received in the tissues of the neck during quantification of iodine in the thyroid by X-ray fluorescence spectrometry" *Radiation Effects & Defects in Solids* vol 173, no 3 – 4, 2018, pp 318 – 328

[71] Reginster, J., Y., Deroisy, R., Dougados, M., Jupsin, I., Colette, J., and Roux, C. "Prevention of early postmenopausal bone loss by strontium ranelate: the randomized, two-year, double-masked, dose-ranging, placebo-controlled PREVOS trial." *Osteoporosis international* 13, 2002, pp 925-931.

[72] Reginster J. Y., Seeman E., De Vernejoul M. C., Adami S., Compston J., Phenekos C., Devogelaer J. P., Diaz-Curiel M., Sawicki A., Goemaere S., Sorensen O. H., Felsenberg D., and Meunier P. J. "Strontium Ranelate Reduces the Risk of Nonvertebral Fractures in Postmenopausal Women With Osteoporosis: Treatment of Peripheral Osteoporosis (TROPOS) Study" *Journal of Clinical Endocrinology and Metabolism*, vol 90, 2005, pp 2816 – 2822.

[73] Rehak, P., Gatti, E., Longoni, A., Kemmer, J., Holl, P., Klanner, R., Lutz, G., and Wylie, A. "Semiconductor Drift Chambers for Position and Energy Measurements" *Nuclear Instruments and Methods in Physics Research* vol A235, 1985, pp 224 – 234

[74] Rehak, P. et al. "Spiral Silicon Drift Detectors" *IEEE Transactions on Nuclear Science* vol 36, no 1, 1989, pp 203 – 209

[75] Rehak, P., Walton, J., Gatti, E., Longoni, A., Sanpietro, M., Kemmer, J., Dietl, H., Holl, P., Klanner, R., Lutz, G., Wylie, A., and Becker, H. "Progress in Semiconductor Drift Detectors" *Nuclear Instruments and Methods in Physics Research* vol A248, 1986, pp 367 – 378

[76] Roschger, P. et al. "Bone material quality in transiliac bone bioposies of postmenopausal osteoporotic women after 3 years of strontium ranelate treatment" *Journal of Bone and Mineral Research,* vol 25, no 4, 2010, pp 891 – 900.

[77] Santos, J.C. et al. "Characterization and applicability of low-density materials for making 3D physical anthropomorphic breast phantoms" *Radiation Physics and Chemistry* vol 164 2019

[78] Savi, M et al. "Study on attenuation of 3D printing commercial filaments on standard X-ray beams for dosimetry and tissue equivalence" *Radiation Physics and Chemistry* vol 182 2021.

[79] Sheehan, B. Investigation of the Potential Effects of Bone Turnover on X-ray Fluorescence Measurements of Bone Lead in Young Women. 2022. McMaster University, MSc.

[80] Solc et al "Tissue equivalence of 3D printed plastics for medical phantoms in radiology" *Journal of Instrumentation* vol 13, 2018.

[81] Soultanidis et al. "Development of an anatomically correct mouse phantom for dosimetry measurement of small animal radiotherapy research" *Physics in Medicine and Biology* vol 64 2019

[82] Specht, A., J., et al. "Measurements of Strontium Levels in Human Bone In Vivo Using Portable X-ray Fluorescence (XRF)" Applied Spectroscopy vol 71, no 8, 2017, pp 1962-1968.

[83] "A portrait of Canada's growing population aged 85 and older from the 2021 Census" *Statistics Canada* April 27 2022 https://www12.statcan.gc.ca/census-recensement/2021/as-sa/98-200-X/2021004/98-200-X2021004-eng.cfm accessed May 2024

[84] Struder, L. "Silicon drift detector – the key to new experiments" *Naturwissenschaften* vol 85, 1998, pp 539-543.

[85] Thompson, A., Attwood, D., Gullikson, E., Howells, M., Kim, K., J., Kirz, J., Kortright, J., Lindau, I., Liu, Y., Pianetta, P., Robinson, A., Scofield, J., Underwood, J., Williams, G., and Winick, H. "X-ray Data Booklet" *Lawrence Berkeley National Laboratory*, 2009.

[86] Villani et al. "Dosimetric characterization of 3D printed phantoms at different infill percentages for diagnostic X-ray energy range" *Radiation Physics and Chemistry* vol 172 2020.

[87] Werner, Christopher John, Jeffrey S. Bull, Clell Jeffrey Solomon, Forrest B. Brown, Gregg Walter McKinney, Michael Evan Rising, David A. Dixon et al. *MCNP version 6.2 release notes*. No. LA-UR-18-20808. Los Alamos National Laboratory (LANL), Los Alamos, NM (United States), 2018.

[88] Wielpolski L., Vartsky, D., Yasumura, S., and Cohn, S., H. "Application of XRF to Measure Strontium in Human Bone In Vivo" *Advances in X-ray Analysis,* vol 26, 1982, pp 415 – 421.

[89] Zamburlini, M., et al. "In vivo study of an x-ray fluorescence system to detect bone strontium non-invasively" Physics in Medicine and Biology vol 52, 2007, pp 2107-2122.

[90] Zamburlini et al. 2009 "" X-ray Spectrometry, vol 38, 2009, pp 271 – 277.

[91] Zhang, X., Wells, E., M., Specht, A., J., Weisskopf, M., G., Weuve, J., and Nie, L., H. "In vivo quantification of strontium in bone among adults using portable x-ray fluorescence" *Journal of Trace Elements in Medicine and Biology* vol 74, 2022, pp 127077

[92] Doublier, A. et al. "Distribution of strontium and mineralization in iliac bone biopsies from osteoporotic women treated long-term with strontium ranelate" *European Journal of Endocrinology*, vol 165, 2011, pp 469 – 476.

[93] Nielsen, S., P., Slosman, D., Sorensen, O., H., Basse-Cathlinat, B., De Cassin P., Roux, C., and Meunier, P., J. "Influence of Strontium on Bone Mineral Density and Bone Mineral Content Measurements by Dual X-ray Absorptiometry" *Journal of Clinical Densitometry* vol 2, no 4, 1999, pp 371 – 379.

[94] Kawano, T. et al. "IAEA Photonuclear Data Library 2019" *Nuclear Data Sheets*, vol 163, 2020, pp 109 – 162.

[95] Metropolis, N. "The beginning of the Monte Carlo method." *Los Alamos Science*, vol 15, no 584, 1987, pp.125-130.

[96] "Bone density scan" *Canadian Cancer Society* https://cancer.ca/en/treatments/tests-and-procedures/bone-density-scan accessed May 2024

[97] Heirwegh, C., M., Chettle D., R., and Pejovic-Milic A. "*Ex vivo* evaluation of a coherent normalization procedure to quantify *in vivo* finger strontium XRS measurements" *Med Phys* vol 39 (2), 2012, pp 832-841.

[98] Lord M., L. et al. "Observed deposition of gadolinium in bone using a new noninvasive in vivo biomedical device: results of a small pilot study" *Radiology,* Vol 287, 2017, pp 96 – 103.

[99] Lord M., L. et al. "Self-identified gadolinium toxicity: comparison of gadolinium in bone and urine to health gadolinium-based contrast agent exposed volunteers" *Physiological Measurement*, vol 39, 2018, pp 115008.

[100] Puri, S., et al. "K and L shell x-ray fluorescence cross sections" *Atomic Data and Nuclear Data Tables* vol 61, 1995, pp 289-311.

[101] Snyder R., E., and Secord D., C. "The in situ measurement of strontium content in bone using x-ray fluorescence analysis" *Physics in Medicine and Biology* vol 27, no 4, 1982, pp 515 – 529

[102] Gatti, E. and Rehak, P. "Semiconductor drift chamber – An application of a novel charge transport scheme" *Nuclear Instruments and Methods in Physics Research*, vol 225, no 3, 1984, pp 608 – 614.

Chapter 2:

2.1 Introduction to Chapter 2:

The work in this paper focuses on the creation and implementation of a new *invivo* strontium XRF system. The system consists of a VITUS H150 silicon drfit detector (SDD) from KETEK GmbH, with a ^{109}Cd source in a 180° backscatter geometry. New phantoms were developed consisting of 3D modelled shells, printed using PLA (polylactic Acid) plastic, and a strontium-doped hydroxyapatite core. Two differing strengths of ^{109}Cd sources were tested at two different measurement times: 5 minutes and 30 minutes respectively.

The system performance was best for bare phantoms achieving an MDL of 45 µgSr/gCa for a 5 minute measurement and 22 µg Sr/g Ca for a 30 minute measurement, on par with previous in-vivo strontium XRF systems. The system could also be pushed further with hotter sources resulting in an even better MDL of 7 µg Sr/gCa.

Contamination of the hydroxyapatite phantoms was found to be 0.86±0.05 mg Sr/g Ca, almost 2.5 times that of previously made plaster of Paris phantoms. Thus for any future endeavours in making strontium-doped hydroxyapatite phantoms, it is imperative that the purity of the reagents is verified. In addition the phantoms themselves are more brittle than plaster of Paris phantoms, and should be handled more delicately. While this contamination was higher than plaster of Paris phantoms, the MDL achieved was still on-par with previous systems. In addition, 3D printing allowed us to create more anatomically accurate phantoms much quicker and more reliably than conventional means.

Finally the Compton correction method was able to accurately measure the thickness of overlying PLA, suggesting this could be used in the future with coherent normalization to compensate for changes in source-subject distance.

The original idea for using the SDD in combination with the ^{109}Cd source was suggested by Dr. David Chettle. Data collection, study design, and analysis were performed by myself, with contributions and guidance for data analysis from Dr. Fiona McNeill. In addition, I wrote the first draft of the manuscript, with Dr. Fiona McNeill serving as primary editor, and Drs. Eric Da Silva and David Chettle serving as secondary editors. The 3D model for the finger phantoms was previously modelled and provided by Ms. Renee-Claude Bider and Ms. Etain Davidson. Printing of the phantoms, source holder and phantom holders were done by Ms. Shereecia Bangura, with upkeep of the 3D printer provided by Mr. Justin Bennett.

Dr. Eric Da Silva also provided lab space, materials and guidance in the construction of the plaster of Paris and hydroxyapatite phantoms. Reagents were purchased through Dr. Da Silva's NSERC Discovery Grant. Ms. Minahil Manzoor helped in the preparation and filling of both the plaster of Paris and hydroxyapatite phantoms.

This article is ready for publication and will be submitted to the Journal of Analytical Atomic Spectroscopy.

2.2 Paper 1: Development of an improved portable radioisotope-based x-ray fluorescence system for the *in vivo* measurement of bone strontium

L. M. Bickley[1], E. Da Silva[2], D. R. Chettle[1], F. E. McNeill[1,*]

[1]Department of Physics and Astronomy, McMaster University, 1280 Main Street West, Hamilton, ON, Canada L8S 4M1

[2]Department of Physics, Toronto Metropolitan University, 350 Victoria Street, Toronto, ON, Canada M5B 2K3

Abstract

Strontium is a trace element commonly found in produce and drinking water. While high levels of strontium can cause impaired bone growth in children, and excess mortality in animals, at low doses there are no known toxic effects in humans. Strontium is purported to be beneficial for post-menopausal bone density loss and strontium citrate is used as a nutritional supplement by some women. A system that can monitor bone strontium levels quickly and accurately could be of use in the assessment of the health risks of self-administered strontium supplements.

Previous radioisotope-based systems for measurement of strontium *in vivo* take upwards of 30 minutes for measurements and are not portable. This article describes the development of a system for the measurement of strontium in bone that comprises a silicon drift detector (SDD) with a ^{109}Cd source in a 180^{o} backscatter geometry. New anthropomorphic phantoms were developed for system calibration. Phantoms are 3D printed PLA shells in thicknesses from 2 – 4 mm with hydroxyapatite cores doped with strontium in concentrations ranging from 0 – 1500 µg Sr/g Ca.

The system performance was investigated using two different sources whose reported activity was a factor of ten different. Studies were also performed for two different measurement times: 120 s and 1800 s. During development, it was noted that while one ^{109}Cd source did emit an order of magnitude higher 88 keV gamma-rays than the other, it did not emit an order of magnitude greater fluence of silver x-rays. This is attributed to differences in source encapsulation. This lower-than-expected x-ray fluence meant that the best minimum detectable limit (MDL) was determined to be 22 µg Sr/g Ca for a 30minute measurement time similar to previously reported radioisotope systems. However, low system dead times indicated that the system was not used at maximum throughput, and it is predicted that with higher silver x-ray fluence sources, the system could achieve a minimum detectable limit of 7 µg Sr/g Ca.

Keywords: strontium, X-ray fluorescence, bone

1. Introduction

Strontium (Sr) is an ubiquitous trace element present in 0.04% of the Earth's crust, which is commonly found in consumables such as produce and drinking water[1]. High levels of strontium may cause impaired bone growth in children[2], and very high levels of Sr ingestion have been found to cause an excess in mortality in animal studies, although no known deaths from stable Sr ingestion by humans have been found[1]. Low level exposure has been shown to be non-toxic or even beneficial with one purported beneficial property of strontium being its relationship to bone mineral density (BMD). Strontium is a bone-seeking mineral, and it has been suggested that supplementing the diet with low levels of strontium could increase the BMD of humans, and potentially help treat osteoporosis. Early studies of strontium intake in animals showed an increase in new bone formation[3,4,5,6,7], and a decrease in bone resorption[4]. These effects were seen in as little as four weeks, but only at higher administered doses. While these studies[3,4,5,6,7] did not directly measure the bone mineral density (BMD) of the animals, it was inferred that the increased bone growth would impact the bone density.

Later studies were performed on strontium ranelate, a drug initially approved for osteoporosis treatment in the European Union in 2004 (as Protelos®[8]) and Australia in 2007 (as Protos®[9]). Four large-scale clinical trials (named PREVOS[10], STRATOS[11], TROPOS[12] and SOTI[13]) aimed to investigate the required minimum dose for beneficial effects (PREVOS, STRATOS), and the long-term efficacy and safety of the drug (TROPOS, SOTI). These studies were able to show a clear relationship between strontium ranelate supplementation and BMD. For participants in the SOTI study, those receiving a dose of strontium ranelate of 2 g/day had a 6.8 % increase in BMD averaged across three different bone sites, compared with a 1.3 % decrease below the original baseline level for the placebo group[13]. Similar results were seen in the TROPOS study[12] which showed a significant increase in the BMD of women who took 2 g/day of strontium ranelate as compared with women in a placebo group. This study also showed a decrease in the number of new vertebral fractures in women receiving strontium supplementation[12]. Post-hoc studies[14,15] on the SOTI and TROPOS groups[14] showed that for every 1% increase in BMD beyond year one, the relative risk of a new vertebral fracture dropped by an average of 3%. Rather than a single dose of 2 g/day strontium ranelate, participants in the PREVOS and STRATOS studies[16] were given a range of doses of strontium ranelate: 125 mg /day, 500 mg per day, 1 g /day or 2 /day. The participants showing the largest increase in BMD from the original baseline were those in the 2 g/day group, with no significant effects being noted below a dose of 1 g / day. These studies also showed an increase in markers of bone formation, with levels in the 2 g/day group being significantly higher than those in the placebo group. The BMD values reported by these studies may be inflated, as studies[18,19] showed an overestimation of the BMD by 10% for every 1% increase in molar strontium concentration (*i.e.,* the ratio of Sr/(Sr+Ca)) in bone. This should be considered when analyzing the efficacy of supplementation.

Mild side effects were reported in these studies which included diarrhea and gastritis, although these particular studies[14,15,13,16] did not report any adverse events. However, a review by the European Medicines Agency (EMA)[17] found that those who suffered from heart disease, venous thromboembolic events, peripheral artery disease or cerebrovascular disease were at increased risk of heart attack from strontium ranelate use, and for this reason the use of the drug is now restricted in Europe. Australia[20] followed suit, restricting use of the drug in 2014.

Strontium ranelate was never approved for use in Canada, and so there are no populations of women who were prescribed the drug. However, there are Canadian women who choose to supplement

their diet with strontium in the belief that it prevents or treats osteoporosis[21,22]. Compounds such as strontium citrate are available from health food stores. Canada recognizes that there may be health risks associated with strontium supplementation[23,24] and requires businesses selling supplements containing more than 4 mg strontium to attach a warning label about cardiovascular risks. Canada has also legislated a limit of strontium in drinking water of 7 mg/L per day. [25] To date, no known rigorous studies have been done on the long-term health effects of strontium citrate ingestion. A study in rodents found that strontium citrate increased the concentration of strontium in bone by a factor of 1.5 after 8 weeks. [26] Pilot studies showed that women who reported self-supplementing with strontium citrate had increasing strontium levels in bone and were often ingesting more than 100 times the daily recommended limit of strontium[21,22]. There are therefore potential populations of people in Canada who have elevated exposure to strontium, but the impact on their health is not known. Studies that compare a measured bone strontium level with the potential health risks would provide information regarding risk, allowing government to make informed decisions about the sale of these supplements.

Such studies require a method of assessing bone strontium non-invasively *in vivo*. Early work on the quantification of bone strontium *in vivo* was performed *via* animal studies[27,28] using x-ray fluorescence (XRF). Both of these early systems utilized a Si(Li) detector, and either a ^{109}Cd or ^{125}I x- and ϒ-ray source[27,28]. No further work was conducted on these systems beyond the initial publications, but in 2004 the technology was re-examined[29], utilizing a Si(Li) detector, a ^{109}Cd source, 1800 s live-time measurements, and plaster of Paris (poP) phantoms. A 90^{o} geometry was found to produce a better signal-to-noise ratio when compared to a 180^{o} backscatter geometry. This system produced phantom based minimum detectable limits (MDL) ranging from 110 µg Sr/g Ca for low-purity phantoms to 170 µg Sr/g Ca for high purity phantoms. A re-design of the collimator in 2006[40] further improved the MDL of the system to (44.6 ± 0.9) µg Sr/g Ca. The same Si(Li) detector was employed, but with an ^{125}I source, 1800 s live time measurements, and a 180^{o} backscatter geometry, as the 180^{o} geometry was easier to setup compared to the 90^{o} geometry[30]. This MDL was further reported as being improved in 2007 to (22.9 ± 0.6) µg Sr/g Ca while using the same 1800 s live-time, geometry, detector and source and the system was applied in in vivo studies to measure baseline Sr levels in 22 non-supplementing subjects.[31] This same system was then used in 2008[32] to measure strontium in tooth enamel (MDL 28 µg Sr/g Ca, measurement time 1000 s), and in 2012[33] to measure strontium levels in human cadaver fingers [MDL (22.9 ± 0.6) µg Sr /g Ca[34], measurement time 1800 s]. A further study used the system to investigate the difference in strontium concentrations in rats following ingestion of strontium ranelate *versus* strontium citrate[26] in 2013 although no updated MDL was reported for these rat studies. Finally, two pilot studies in 2012[21] and 2014[22] reported using the same system, each with an MDL of 21 – 23 µg Sr/g Ca[35] in phantoms, to measure the concentration of strontium in bone of volunteers who had been self-supplementing with strontium citrate. No *in vivo* MDL was able to be reported due to inherent strontium contamination of the phantoms. Other research groups developed similar systems to measure concentrations of strontium in bone[36,38], and one study in 2017[36] investigated the concentration of strontium in the bones of a population of children in China who had been exposed to lead.

Much of the research described above employed a measurement time of 1800 s live time. This is possibly too long for a useful clinical tool. Some groups therefore tested shorter measurements times, varying from 1s to 1000s[36,38,33,32,37,39]. Researchers in these two studies[36,38] were able to employ short detection times because they used an SDD detector in an x-ray tube based handheld system, that is a portable (p)XRF device. A study in human teeth[7] used shorter detection times but this does not directly

translate to an indication of the required time for measurements in bone, and a study[37] aiming to develop a correction technique for soft tissue overlay was able to test the theory without a long measurement time. While most measurements in the literature are reported in terms of true times, this does not necessarily explain the clinical utility accurately. Dead times for these systems ranged from as low as 15 % [21] to as high as 50 %[22], leading to actual (true or clock) measurement times of 2100 s to 2700 s. While a 40 minute measurement is acceptable for *in vitro* studies, and experimental *in vivo* measurements, if this technology is to be translated to application outside of the laboratory, especially as a point-of-care device, then the total time of measurement should be on the same order of magnitude as other clinical procedures, such as a DXA scan. DXA scans are employed to test the BMD of a patient over multiple bone sites in the body[40]. They typically take on the order of 5 to 20 minutes[41] in total for multiple site measurement.

This work aimed at developing an improved XRF-based *in vivo* bone strontium measurement system that could attain the required detection limits at measurement times that approach those of other point-of-care devices. We describe the development of an SDD based system employing a ^{109}Cd source, calibrated using a set of 3D printed anthropomorphic finger calibration phantoms. We discuss the accuracy of a soft tissue correction factor and show how these phantoms may create a simpler measurement system that being portable may be able to be deployed in a clinical setting.

2. Materials and Methods

2.1. Detector and electronics

The new *in vivo* x-ray fluorescence strontium measurement system utilized a VITUS H150 Silicon Drift Detector (SDD) in an AXAS-M1 unit with an AXAS-M2 power supply and signal processing unit from Ketek GmBH Inc. fed into an ORTEC DSPEC Plus® spectrometer and computer running GammaVision© gamma spectroscopy software. The AXAS-M1 unit housed the detector, plus a reset preamplifier and the Peltier cooling system. This detector system was chosen as it can handle up to 30,000 counts per second (cps) with a rise time of 1 µs. The H150 SDD has an area of 170mm^2 which is collimated to 143mm^2, with an active silicon thickness of 450 µm. The detector system is encapsulated in a nickel cap with a 25 µm beryllium entrance window.

A source holder and detector cap that had been previously designed for *in vivo* measurements of iron in skin[42] was used for measurements of strontium in bone. This collimator/source holder/cap, was made from aluminum with a 250 µm thick styrene window while the source holder was made of tantalum.

2.2 Excitation source

A ^{109}Cd source was used as the excitation source for the system. ^{109}Cd decays by electron capture to ^{109}Ag. An 88 keV γ-ray is emitted in approximately 4 % of decays with silver (Ag) K x-rays of energy 22.2 keV and 24.9 keV being emitted in 84 % and 18 % of decays, respectively. The observed relative intensity of the Ag x-rays to the ϒ-rays is lower than these numbers indicate, as the Ag x-rays are more attenuated through the source window than the ϒ-rays. However, the photoelectric interaction cross section for Sr is 47.74 cm^{2}g^{-1} at 22.2 keV, 35.03 cm^{2}g^{-1} at 24.9 keV and 0.95 cm^{2}g^{-1} at 88 keV. The combination of the higher emission intensity of the silver x-rays with the larger photoelectric cross-section means that photoelectric interactions on strontium are considerably more likely to occur with the Ag x-rays and they can be considered to be the dominant fluorescing source with contributions from the 88 keV ϒ-rays being considered negligible.

Two different source activities were used in this study. The sources were presumed to be identical in design having been made in the same facility: the ^{109}Cd was plated onto a 1 mm diameter circular 30µm thick Ag plug and placed in a 3 mm x 3 mm steel capsule, with a 100 µm thick titanium entrance window. We identify this source as Source 1 which had a nominal activity of 79.82 MBq in April 2023 (down from 5.59 GBq in February 2016, calculated), while the source we identify as Source 2 had a nominal activity of 1.16 GBq in April of 2023 (down from 4.995 GBq in August 2020, calculated).

2.3. Phantoms

Three-dimensional finger phantoms were modelled in Autodesk Inventor. The fingers comprised an outer soft tissue layer which was printed from 100% infill polylactic acid (PLA) plastic (Overture). Phantoms were modelled as a hollow shell, with a length of 60 mm and inner diameter of 7.5 mm at the base of the phantom, tapering to an inner diameter of 9.7 mm at the tip of the phantom. The soft tissue layer was modelled as five thicknesses: 2 mm, 2.5 mm, 2.9 mm, 3.5 mm, and 4.0 mm. These phantom shells were then filled with strontium-doped calcium hydroxyapatite to mimic bone mineral, following the same procedure outlined previously[43].

The calcium hydroxyapatite infill was created by adding calcium hydroxide to calcium hydrogen phosphate dibasic to achieve a Ca/P ratio of 1.67. A strontium standard solution, in the form of an ICP-OES standard solution (10000 µgSr/L, Ultra Scientific) was then added to reach the desired concentration. Phantoms of strontium concentration 0, 25, 50, 100, 250, 500, 750, 1000, 1250, 1500 µg Sr/g Ca were created. The components were thoroughly mixed to ensure a homogenous distribution of strontium. A setting solution of sodium phosphate dibasic (Sigma-Aldrich) was then added until a free flowing consistency was achieved and the mixture was poured into the 3D printed phantom shells and left to set for a week. To minimize air bubbles the shells were tapped firmly on a hard surface immediately after filling to remove any air bubbles.

A phantom with no soft tissue (hereafter referred to as a 0 mm phantom) was modelled as a cylinder with length of 60 mm and diameter 7.5 mm. These were created from a cylindrical mould with wall thickness of 2.0 mm.

The attenuation coefficient of the 3D printed plastic was measured to ensure it was a suitable soft tissue model for this x-ray energy range. While the coefficient could be calculated from the presumed composition, other studies[44] have suggested that the attenuation coefficient can vary from manufacturer to manufacturer, so empirical testing is required. A custom source holder was printed for the ^{109}Cd source, with a lead pinhole collimator. Previously printed[45] bricks of 100 % infill PLA plastic with varying thicknesses (up to a total distance of 10 cm) were placed between the source and the detector and spectra acquired for 5 minutes.

The attenuation was calculated by plotting the area of the two Ag K x-ray peaks at 22.2 keV and 24.9 keV against the PLA thickness. An exponential function was fitted using Origin 2023 and the attenuation coefficients for 22.2 and 24.9 keV were calculated. These were then compared to the theoretical coefficients for soft tissue at these energies.

2.4. System Geometry and Phantom Measurements

The detector system was set up in a 180^{o} 'backscatter' geometry with the ^{109}Cd source mounted on the front of the detector in the tantalum source holder (Figure 1). Finger phantoms were placed in a custom printed source holder oriented vertically and placed at an estimated distance of 2 to 3 mm from the source. The 0 mm phantom was oriented horizontally to the source. The deadtime was kept to between 2 % to 5 %.

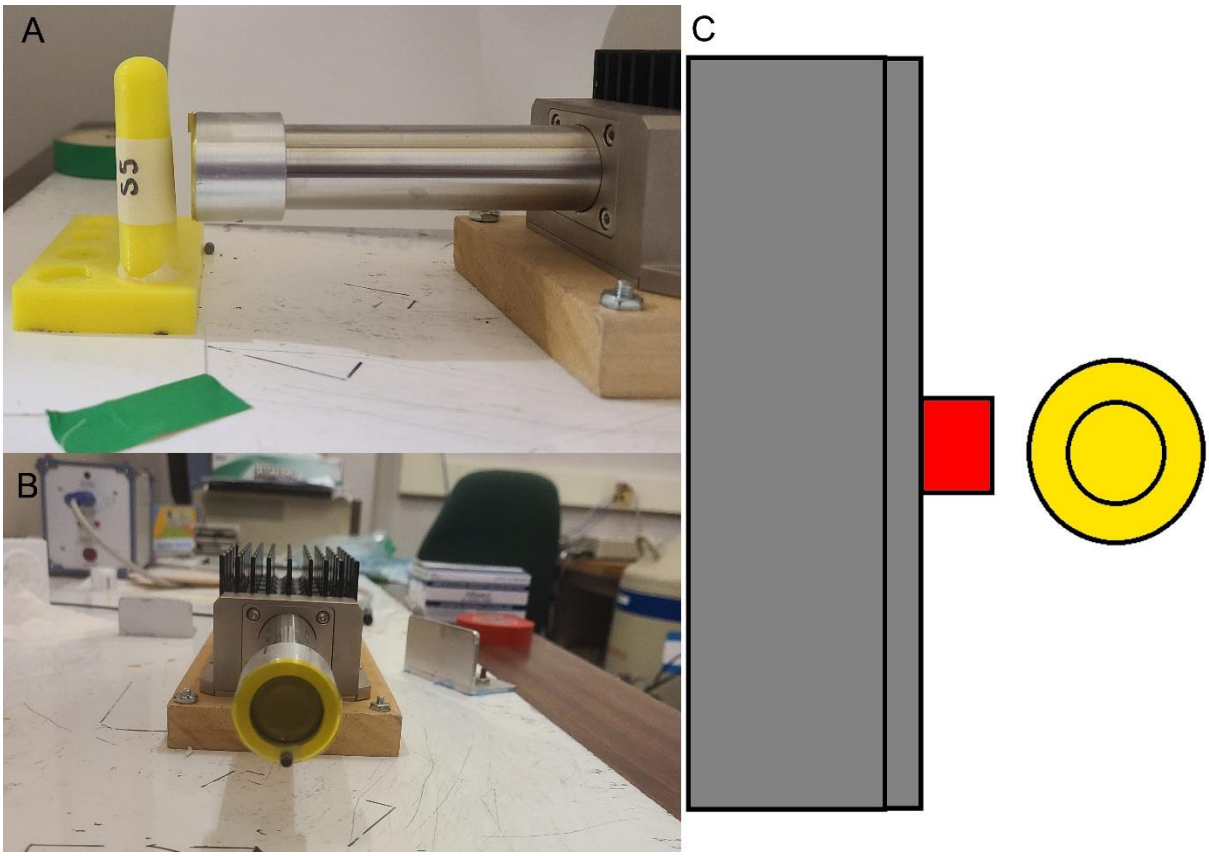

Figure 1: A photograph showing the detector and phantom holder with phantom on the top left (A), and a head-on view of the detector in the bottom left (B). On the right (C) is a not-to-scale diagram of a top-down view of the detector showing the location of the source in the 180° backscatter geometry. Grey is the detector head, red is the tantalum source holder, and yellow is a finger phantom. Note: the source is centered when one looks at it from above (C).

Phantoms were each measured for 5 minutes and 30 minutes live time for each source resulting in a total of 4 sets of calibration measurements. The 0 µg Sr/g Ca hydroxyapatite phantoms for each tissue overlay thickness were measured 5 times, while all other hydroxyapatite phantoms were measured 3 times for each source. Between measurements each phantom was removed and replaced for the next measurement.

Peak fitting was performed using Origin 2023. A mathematical model was fitted to the spectra to extract x-ray peak areas and the Levenberg-Marquardt method of analysis was used to find the best fit. A sample spectrum from a 1500 µg Sr/g Ca strontium phantom is shown in Figure 2. Strontium K_α and K_β x-rays and features from Compton and coherently scattered Ag x-rays (22.2 keV and 24.9 keV) are clearly observed, as is an x-ray signal from nickel in the detector. The 14.1 keV Sr K_α x-ray, the Ni K_α x-ray, and the 22.2 keV and 24.9 keV coherently scattered Ag K x-rays from the ^{109}Cd decay were fitted using a Gaussian function with a linear background model (equation 1 below). The 15.9 keV strontium K_β x-rays were fitted using two linked Gaussian functions on a linear background model (equation 2 below). The Compton scatter distribution from the Ag x-rays were fitted using a Voigt function given by OriginPro 2023 on top of a complementary error function background model (equations 3 – 5 below).

$$G(x) = mx + b + Ae^{-\frac{(x-\mu)^2}{2\sigma^2}} \quad (1)$$

Where m and b are the slope and intercept of the background, and A, mu and sigma are the amplitude, centre and standard deviation of the gaussian.

$$G(x) = mx + b + A_1 e^{-\frac{(x-\mu_1)^2}{2{\sigma_1}^2}} + A_2 e^{-\frac{(x-\mu_2)^2}{2{\sigma_2}^2}} \quad (2)$$

Where m and b are the slope and intercept of the background, μ_1 , σ_1 and A_1 are the centre, standard deviation and amplitude of the first gaussian, and μ_2, σ_2 and A_2 are the centre, standard deviation and amplitude of the second gaussian.

$$y = y_0 + \int_{-\infty}^{\infty}(f_1 * f_2)dx + erfc\left((x - x_c)/(\sqrt{2\pi}w_G)\right) \quad (3)$$

$$f_1(x) = \frac{2A}{\pi}\frac{w_L}{4(x-x_c)^2+{w_L}^2} \quad (4)$$

$$f_2(x) = \sqrt{\frac{4\ln(2)}{\pi}}\frac{e^{-\frac{4\ln(2)}{{w_G}^2}*x^2}}{w_G} \quad (5)$$

Where x_c is, w_L is the width of the Lorentzian, w_G is the width of the Gaussian, and A is the area of the Lorentzian.

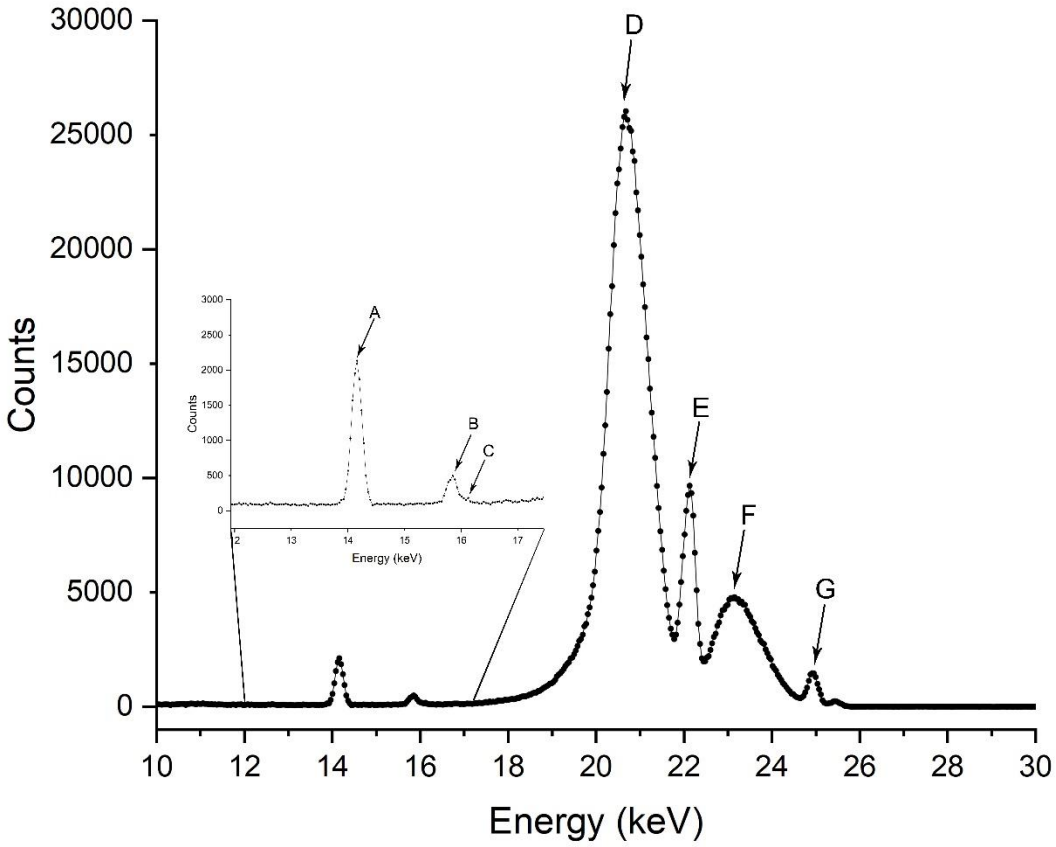

Figure 2: An example strontium spectrum of a 1500 µg Sr/g Ca phantom, with 2mm soft-tissue overlay thickness showing the coherently (E,G) and Compton scattered silver -rays (D,F) and an expanded view of the strontium x-rays (A,B,C).

Net peak areas for the strontium K_α and K_β x-rays were plotted against phantom concentration for each tissue overlay thickness to obtain calibration lines for each finger phantom tissue overlay thickness. The MDL for each phantom thickness set was then calculated as twice the uncertainty in the zero concentration phantom divided by the slope of the appropriate calibration line to obtain the detection limit in units of µg Sr/g Ca.

Strontium is a ubiquitous contaminant in calcium compounds and there is often an observed non-zero calibration line intercept arising from strontium in the phantom materials. The strontium concentration of potential phantom contamination was calculated by dividing the intercept of the calibration line by the slope of the given calibration line. This assumes the intercept on the calibration line arises solely from contamination and that the spectral fitting function does not introduce an artifact.

2.5. Compton Thickness Estimates

Strontium produces low energy x-rays that can be significantly attenuated by soft tissue. To accurately estimate strontium bone content, some method of soft tissue estimation is required. Previous studies[21,22,29,31] have employed ultrasonography to obtain estimates, but this is costly and adds a layer of complexity to the measurement. To test whether accurate estimates of the tissue overlay thickness could be extracted from the phantom spectra, a modified version of a published Compton thickness estimate technique[37] was implemented. In brief, a relationship between the size of the Compton scatter distribution from the 22.2 keV and 24.9 keV Ag x-rays and the soft tissue thickness was tested. This was estimated based on the net peak areas from the 1500 µg Sr/g Ca phantoms for each source and measurement time combination. This relationship was then used to estimate the soft tissue thickness, which was compared with the known value of tissue thickness of the phantom. By plotting the estimated soft tissue thickness against the known value of soft tissue thickness, the slope and significance of the relationship can be calculated, thus showing whether thicknesses could be determined reliably in unknown measurements.

3. Results

3.1. PLA Plastic as a soft tissue surrogate

The measured mass attenuation coefficients for PLA plastic at 22.2 and 24.9 keV were 0.672 cm^2g^{-1} and 0.579 cm^2g^{-1} respectively. These compare extremely well to the attenuation coefficients for the NIST tabulated ICRU four component soft tissue model of 0.673 cm^2g^{-1} and 0.565 cm^2g^{-1}. The differential attenuation through 1 cm of soft tissue versus through 1 cm of PLA would be 7.9 % at 22.2 keV and 8.5 % at 24.9 keV. At the expected tissue overlay thicknesses of soft tissue in the finger, the differences in attenuation would thus be negligible.

3.2. Calibration lines, sensitivity and MDL

Figure 3 shows example calibration lines for both ^{109}Cd sources for counting times of 5 minutes and 30 minutes. All calibration lines are shown for the 2 mm (the thinnest PLA printed tissue overlay) thickness finger phantom. The slope of the regression of K_α x-ray peak area versus phantom concentration and K_β x-ray concentration versus phantom concentration were highly significant ($p < 0.001$, $R^2 > 0.85$) for all PLA printed phantoms. The slope of the regressions for the zero tissue overlay thickness phantoms against phantom concentration were poorer than the slopes of phantoms with tissue overlay, with the significance ranging from $p = 0.012$ to $p < 0.001$, and R^2 values ranging from 0.26 to 0.94.

Figure 4 shows the sensitivity of the system i.e. the measured K_α and K_β peak area counts per µg Sr/g Ca for both sources and both times. As expected, the sensitivity decreased with increasing finger phantom soft tissue thickness. Source 2 is reported by the manufacturer as being a factor of 10 times more active than Source 1. However, for the 5 minute counts and the 30 minute counts, the sensitivity was found to be only 25 % and 10 % higher, respectively.

Figure 5 shows the MDL as determined from the K_α calibration line versus phantom wall thickness for both sources for 5 minutes and 30 minutes, respectively. As expected, the MDL becomes poorer with increasing phantom wall thickness. Only the K_α detection limit is shown. The K_β detection limit was calculated but was significantly poorer than the K_α detection limit in every instance. Overall, when the K_α and K_β MDLs were combined, (using an inverse variance weighted mean), it was found that the addition of the K_β information only improved the detection limit by (1.0 ± 0.2) % on average. As so little extra information was provided, further analysis focused solely on the K_α calibration slope. Table 1 shows the MDLs for the thinnest and thickest phantoms for both sources for both time intervals. The relationship between the 5 minute and 30 minute MDLs for each source were found to be close to the expected value of 0.41 (from $1/\sqrt{6}$). The ratio of the 30 minute MDL to the 5-minute MDL for Source 1 was 0.40 ± 0.03 while the ratio for Source 2 was 0.43 ± 0.03.

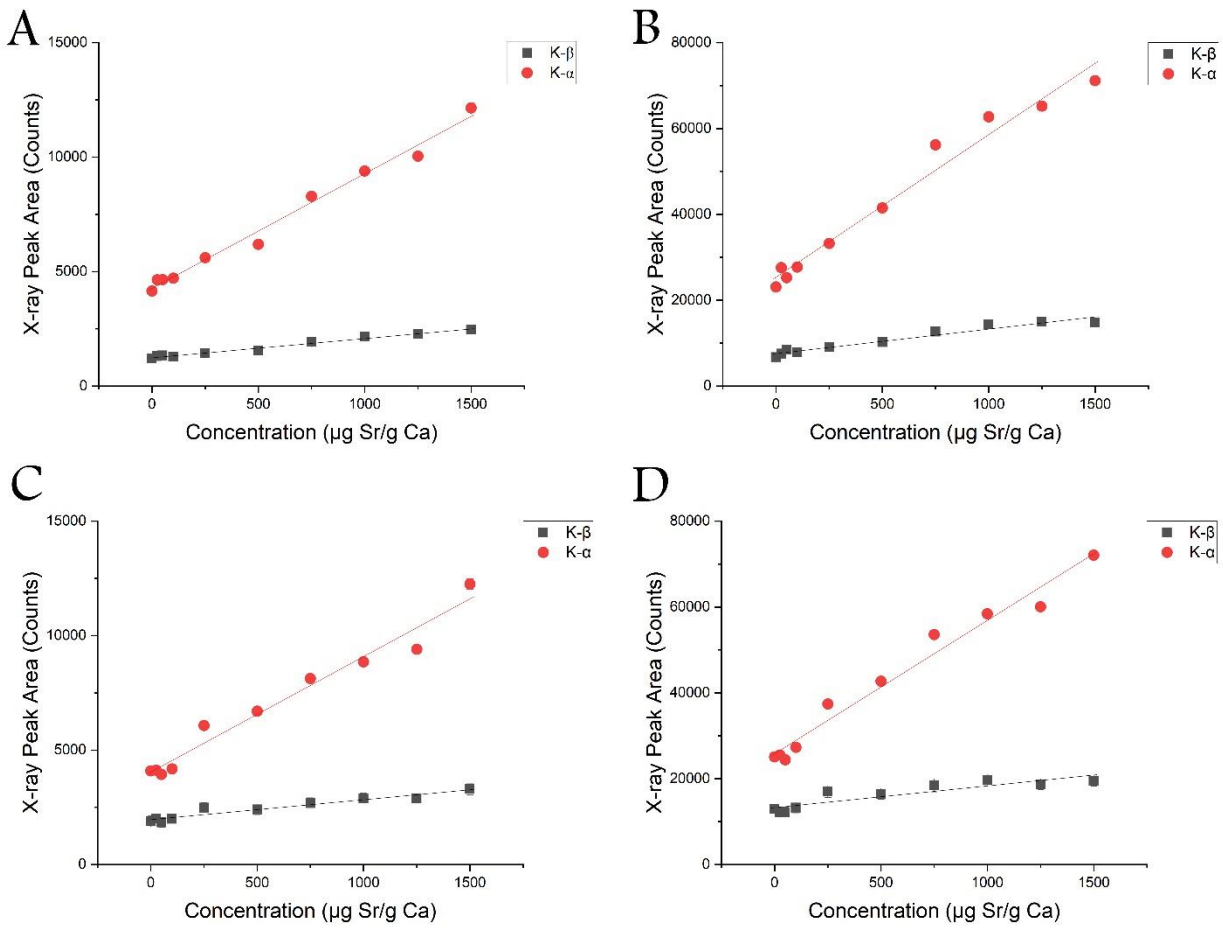

Figure 3: Calibration lines obtained from 2 mm thick printed PLA finger phantoms for K_α x-ray area versus concentration (red) and K_β x-ray area versus concentration (black) for both sources and both measurement times. Images A and B show the 5-minute (A) and 30-minute (B) measurement time for Source 1, while images C and D show the 5-minute (C) and 30-minute (D) measurement time for Source 2. While Source 1 and 2 are reported as being a factor of 10 x different in activity, this is not observed in the calibration lines.

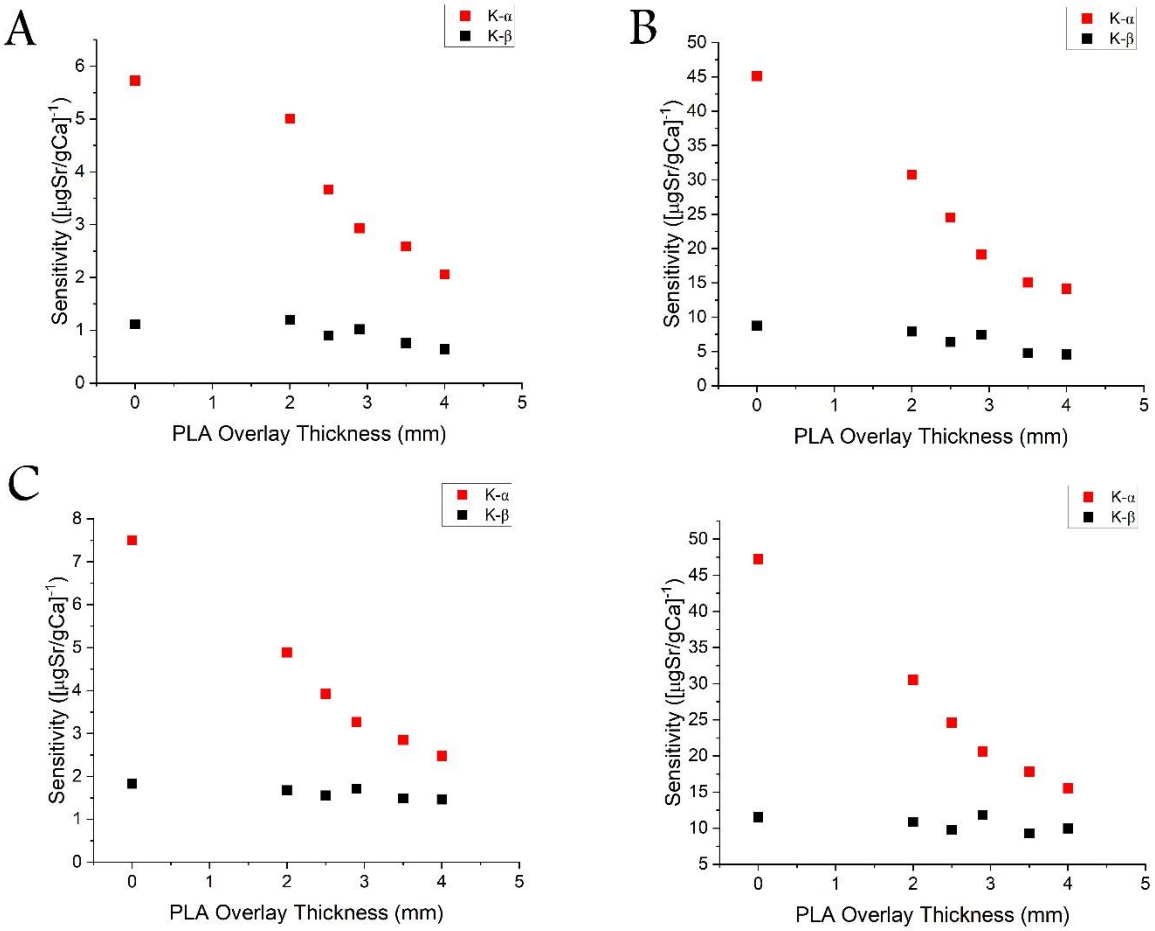

Figure 4: The sensitivity of the detection system defined as x-ray peak area detected per µg Sr/g Ca for K_α x-ray area versus phantom wall thickness in mm (red) and K_β x-ray area versus phantom wall thickness in mm (black) for Source 1 (A – 5 minutes, B – 30 minutes) and Source 2 (C – 5 minutes, D – 30 minutes). While the two sources are reported as being a factor of 10 x different in activity, this is not observed in the sensitivity signal.

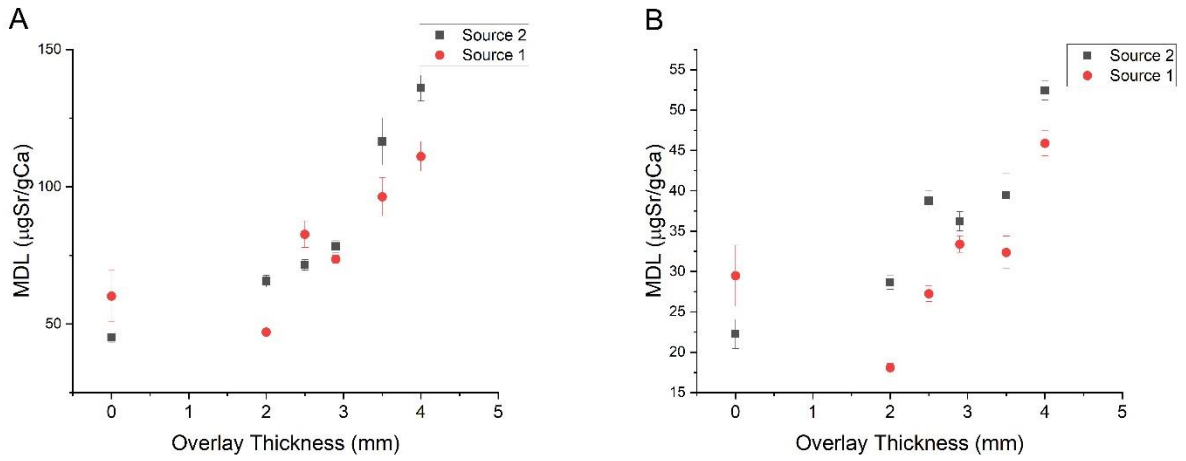

Figure 5: The K_α x-ray based MDL for different wall thicknesses of phantoms for Source 1 and Source 2 for 5 minutes (A) and 30 minutes (B). The difference in the MDL suggests that Source 2 only emits a factor of approximately 1.8 times more silver x-rays than Source 1 despite the sources reportedly being a factor of 10 different in activity.

Table 1: Minimum detectable limits for both sources for both counting times for the thinnest and thickest phantoms. The MDLs for individual sources for the different counting times change as expected. The MDL for Source 2 was expected to be approximately 3 times better than for Source 1 but is only a factor of approximately 1.8 better.

Source	Time (s)	MDL (µg Sr/g Ca 0 mm thickness	MDL (µg Sr/g Ca) 4 mm thickness
Source 1	300	60	110
Source 2	300	45	136
Source 1	1800	29	46
Source 2	1800	22	52

3.3. Phantom contamination

As can be seen in Figure 3, all the K_α x-ray-based calibration lines had a positive intercept, and our hypothesis is that this is most likely due to strontium contamination in the calcium ingredients of the phantoms. Contamination levels were calculated for each set of calibration data by assuming that the intercepts on the calibration lines are an estimate of the contamination level in units of µg Sr/g Ca. Table 2 shows two estimates for each calibration line. The first estimate is a calculation of the mean estimate from all phantom wall thickness calibration lines for a specific source and time. The second estimate calculates an inverse variance weighted mean (IVWM) as uncertainties on estimates from individual calibration lines varied. An estimate is also calculated for each method using all data combined. Results were consistent and appear to indicate a level of contamination of approximately 800 to 850 µg Sr/g Ca.

Table 2: Strontium contamination as estimated from calibration line intercepts for both sources for both counting periods. As the individual estimates had differences in uncertainty, an inverse variance weighted mean (IVWM) was calculated in addition to the mean.

Source	Mean Sr contamination (mg Sr/g Ca)	IVWM Sr contamination (mg Sr/g Ca)
Source 1 5 minutes	0.92 ± 0.07	0.86 ± 0.03
Source 1 30 minutes	0.87 ± 0.07	0.77 ± 0.03
Source 2 5 minutes	0.79 ± 0.04	0.76 ± 0.03
Source 2 30 minutes	0.85 ± 0.04	0.82 ± 0.03
Average	0.86 ± 0.05	0.80 ± 0.01

3.4. Compton tissue thickness estimate

Table 3 shows the results of the regressions of the tissue thickness estimated using the Compton tissue technique versus the known thickness. As can be seen, the Compton correlation method estimate was strongly correlated with the overlying soft-tissue thickness for both sources for both time periods and the slopes were not statistically different from 1. The correlation method developed here used the known thickness estimates, so the correlation is expected. However, we wished to assess the value and strength of the correlation to assess the robustness of the technique, by calculating forwards and backwards. The average slope from all four sets of data was 1.07 ± 0.09 and suggests that the Compton tissue technique could provide an estimate of soft tissue thickness for this measurement system, thus obviating the need for additional measurements such as ultrasonography to be employed.

Table 3: Regression statistics for correlation of known PLA thickness and the estimated thickness using the Compton tissue thickness technique to assess the robustness of the technique. Note that the slope value is unitless as we are plotting known thickness (mm) against calculated thickness (mm)

	Slope	R^2 of correlation	P-value correlation	Z-score (difference of slope from 1)	P-value (Two-Tailed Test) for Z score
Source 1 5 min	0.99±0.10	0.957	0.00245	-0.11	0.912
Source 1 30 min	0.93±0.07	0.976	0.00104	-1.00	0.353
Source 2 5 min	1.20±0.12	0.958	0.00238	1.64	0.230
Source 2 30 min	1.14±0.08	0.979	8.45e-4	1.71	0.087
Mean slope estimate	1.07 ± 0.09	N/A	N/A	0.780	0.435

3.5. Normalization to nickel signal

The solid angle subtended by the source on the phantom or finger and the solid angle subtended by the phantom or finger with the detector changes with the position of the phantom. The signal will thus vary in a clinical measurement with any patient motion. If a calibration line based on the Sr K_α x-ray measured at a fixed distance is used, this will mean measurements could potentially be inaccurate if the patient moves. A signal from nickel was observed in the spectrum. This signal arises from the detector itself[42] and has been found to be dependent on the measurement system geometry. We hypothesized that the strontium signal and the nickel system would vary in the same way and the potential for a normalization to the nickel signal was investigated.

The R^2 and *p*-values values for the strontium K_α calibration lines for both sources and both measurement times and the R^2 and *p*-values for the calibration lines with the strontium K_α x-ray signal normalized to the nickel K_α x-ray signal were examined. If we assume that the removal and replacement of phantoms between measurements could result in variation of position, then a successful normalization method should improve the linearity of the calibration lines. R^2 and *p*-values of all calibrations found that any improvement in linearity of the calibration line as a consequence of the normalization were negligible. Only 2 out of 24 Ni Kα/Sr Kα calibration lines showed improvement over the K_α x-ray signal calibration lines alone, with R^2 values improving from 0.80 to 0.84, and 0.96 to 0.97, and p-values improving from <0.0003 to <0.0002.

4. Discussion

4.1. Minimum Detection Limits

Previously published *in vivo* Sr measurement systems have utilized a range of detector types and sources as described earlier in this article. Table 4 presents a summary of the information with detection limits for the different systems for specific live measurement times. As can be seen, the best previously reported MDLs for a radioisotope-based system were in the range 21-23 µg Sr/g Ca[35] for an 1800 s live time measurement. The MDL obtained using source 2 in our new system is comparable, being 22 µg Sr/g Ca for an 1800 s measurement. While the MDL has not been improved, this new system does offer one significant advantage over prior radioisotope-based systems in that it is portable.

The use of an SDD was expected to attain a lower detection limit through the faster processing ability of this type of detector. However, the dead times in this ^{109}Cd system were low, in the range from 4-5 %. This system did not achieve input count rates where the SDD, despite having a smaller detector surface area, could have an advantage over a Si(Li) detector. There is therefore an opportunity for improved detection limits if a source with significantly higher Ag x-ray fluence rates could be used.

The use of Source 2, a reportedly significantly higher activity ^{109}Cd source (as assessed from the 88 keV signal strength), was expected to result in an approximate factor of 10 greater Ag x-ray fluence, and thus a factor of 3 improvement in the MDL. The MDL was thus expected to be of the order of 15 µg Sr/g Ca for a 300 s counting time and 7 µg Sr/g Ca for an 1800 s counting time. This would have been a marked improvement over previous radioisotope-based system. This was not observed in practice. Strontium K_α x-ray signal sensitivities were only a factor of 1.8 higher for Source 2 as compared to Source 1.

Comparison of the spectra for the same phantom for the two different sources determined that the relative heights of the silver 22 keV and 24.9 keV x-rays were different between the sources. In addition, the relative size of the background above 25 keV was significantly higher in Source 2. Direct measurements of each source were made through a pinhole collimator, and it was observed that the relative heights of the 88 keV, 24.9 keV and 22 keV peaks were different (Figure 6). This change in relative height is likely a result of differential attenuation, and so we hypothesize that the source encapsulation was slightly different. Using the changes between the 22 keV and 24.9 keV photons we estimate that source 2 has a thicker capsule that would crudely equate to approximately a 200 µm greater thickness of steel.

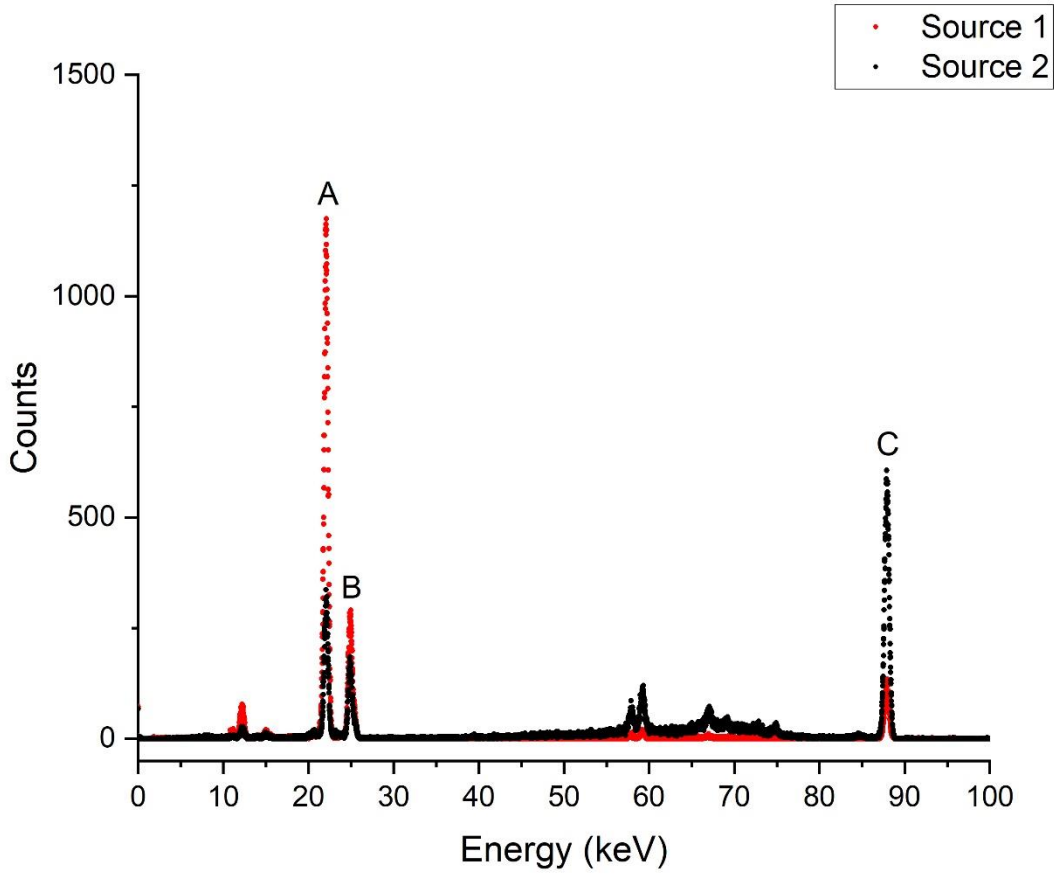

Figure 6: Comparison of relative heights of the spectrum for two different ^{109}Cd sources: Source 1 (Red) and Source 2 (Black). Measurement time of 60s. Peak A corresponds to the 22.2 keV Ag K_α, peak B corresponds to the 24.9 keV Ag K_β, and peak C corresponds to the 88 keV γ-ray from the decay of ^{109}Cd. Source 2 has a thicker capsule, with approximately 200 µm more thickness of steel. The above spectrum was collected on a HPGe detector.

The small improvement in MDL with Source 2 is unexpected; however, an estimate of the MDL can be made for a higher activity source of the encapsulation type of Source 1. When Source 1 was purchased, it was a factor of 70 higher in activity than when measurements were performed. However,

a 70 times greater Ag x-ray fluence would create too high a dead time to make measurements feasible. Simple calculations using a paralyzable deadtime model suggest that a source of encapsulation type 1 that is 16 times higher in activity would result in a deadtime in this system of 40 to 50 %, however this could be further reduced with faster electronics. This suggests that the system could attain a MDL of 7 µg Sr/g Ca using a source of that encapsulation type for an 1800 s live time measurement, which would be a significant improvement over other radioisotope-based systems.

This MDL approaches the performance of hand-held x-ray set based systems, which use 22.2 keV Ag x-rays. While the handheld x-ray systems would still have better performance, likely due to higher incident x-ray fluence, there can be regulatory challenges (such as handheld X-ray systems being regulated by a different governing body than radioisotopes) to their use in human studies in some jurisdictions e.g. Ontario, Canada. For those jurisdictions, this ^{109}Cd-based SDD system would offer advantages of a MDL than prior radioisotope systems, that is close to that of handheld x-ray systems, and attainable in a 5 minute live counting time (10 minute true counting time) measurement, if higher activity sources could be obtained. In addition the doses delivered by these systems are extremely high, delivering 21 mSv to a 1cm^2 area of skin in 120s[36], as opposed to our system which delivers 1.1 mSv to 0.8 cm^2 of skin[42]. The dose for handheld XRF systems can be reduced, but at the cost of an increase in the MDL. The regulatory limit set for doses to the skin in Canada for a member of the public is 50 mSv over a 1cm^2 area[46], meaning that any handheld system would deliver 42% of the maximum dose allowed.

Table 4: A summary of the MDLs attained for various measurement times for various K XRF systems for the *in vivo* measurement of strontium.

	Fluorescing source	**Acquisition Time (s)**	**MDL (µg Sr/g Ca)**
Pejovic-Milic et al. 2004[29]	^{109}Cd	1800	250 (finger, in vivo) 560 (tibia, in vivo) 110 (low purity phantom) 170 (high purity phantom)
Zamburlini et al. 2006[30]	^{125}I	1800	44.6 (phantom)
Zamburlini et al. 2007[31]	^{125}I	1800	22.9 (finger phantom)
Heirwegh et al. 2012[33]	^{125}I	1800 or 3600	22.9 (ex vivo finger)[19]
Moise et al. 2012[21] and Moise et al. 2014[22]	^{125}I	1800	21 – 23 (phantom)[26]
Specht et al. 2017[36]	PXRF	120	3.8 (no soft-tissue equivalent) 42.5 (9mm thickness soft-tissue equivalent)
Zhang et al. 2022[38]	PXRF	120, 180, 300	15.2 (5mm thickness soft-tissue equivalent)

This work Source 1	^{109}Cd	300	60 (0mm) and 111 (4mm)
This work Source 2	^{109}Cd	300	45 (0mm) 136(4mm)
This work Source 1	^{109}Cd	1800	29 (0mm) and 46 (4mm)
This work Source 2	^{109}Cd	1800	22 (0mm) and 52 (4mm)

4.2. Phantoms

We have developed new 3D printed finger phantoms that are a better match to human tissue type and shape. The PLA outer material is a very good match to ICRU 4 component soft tissue, and the bone-mimicking matrix is calcium hydroxyapatite as in real bone. These phantoms are an improvement over previous calibration standards. However, strontium contamination in the matrix is a problem.

Previous studies determined levels of contamination for plaster of Paris phantoms of 363 µg Sr/g Ca[35], while for the strontium doped calcium hydroxyapatite phantoms in this study, the level of contamination was determined to be (0.86 ± 0.05 mg Sr/g Ca, almost 3 times greater. This is unfortunate as it was hoped that the creation of hydroxyapatite phantoms would result in lower contamination levels as this was found to be the case for calcium hydroxyapatite phantoms reported in 2008[32]. We hypothesize that the contamination difference is likely due to contamination of the reagents, as it was reported in 2008[32] that one of the reagents ($CaCO_3$) had an inherent strontium contamination of approximately 420 µg Sr/g Ca, leading to a phantom containing 370 µg Sr/g Ca. Those researchers were able to purify the $CaCO_3$ reducing the contamination of the resulting phantom to 2 µg Sr/g Ca. We therefore suggest that future phantoms source appropriate reagents and purify the materials before use.

4.3. Compton thickness correction

It appears likely that the Compton Correlation method will be able to predict the thickness of overlying soft tissue using this system allowing for selection of the appropriate calibration line. This will be a distinct advantage, as secondary methods of tissue thickness estimation will not need to be employed. This will reduce the costs and time associated with the measurement, improving its suitability for clinical use.

4.4. Normalization to the nickel signal

The normalization to the nickel signal was not found to result in any significant improvement to Kα x-ray calibration lines. This may be due to careful and precise positioning of the phantoms between measurements relative to the source holder. The Sr Kα x-ray calibration lines are good, and there was little room for improvement.

However, this normalization may still be useful for *in vivo* work. While it is straightforward to ensure a phantom is measured in the same position relative to the detector face in repeated measurements, this will not be possible with human participants. More importantly, with measurement times ranging from 120 s[36,38] to 1800 s[33,21,22,29,30,31] live times, there is potential for

participants to move during the measurement. Any restraints would be required to be minimal and so participant motion is possible. A normalization that could help reduce the variation in the data would be advantageous and this should be explored in future work.

5. Conclusion

A K-XRF system for the measurement of Sr *in vivo* has been developed and tested. The system employs a silicon drift detector and a ^{109}Cd source. The system was able to achieve a best performance MDL in bare phantoms of 45 µg Sr/g Ca for a 5 minute measurement time, and 22 µg Sr/g Ca for a 30-minute measurement time. Use of the system with a higher activity source could result in MDLs of 11 and 7 µg Sr/g Ca for 5-minute and 30-minute measurements respectively. This represents an improved performance over prior radioactive source-based systems, although handheld (p)XRF systems still perform a factor of 2 to 3 better, at the cost of a significantly higher skin dose to the patient.

Calibration against 3D PLA plastic phantoms suggests that the system can employ a Compton estimation method and thus the system would require no ultrasound measurements to be performed. This, in combination with the portability of the system, offers advantages over prior radioisotope-based systems. However, challenges with Sr contamination in phantom materials and the lack of a normalisation method to account for patient motion mean that further work is required before the system can be tested in human studies.

Funding:

The reagents for phantom creation were bought through an NSERC Discovery Grant by Dr. E. Da Silva.

Acknowledgements:

The authors would like to acknowledge the tremendous help of Minahil Manzoor in filling the phantoms, as well as the help of Shereecia Bangura and Justin Bennett for 3D printing the phantom shells and source holders.

References:

[1] "Strontium" *Encyclopedia Britannica* https://www.britannica.com/science/strontium Accessed January 2024

[2] Agency for Toxic Substances and Disease Registry (ATSDR). 2004. Toxicological profile for Strontium. Atlanta, GA: U.S. Department of Health and Human Services, Public Health Service.

[3] Ferraro E. F., Carr R., and Zimmerman K. "A Comparison of the Effects of Strontium Chloride and Calcium Chloride on Alveolar Bone" *Calcified Tissue International* vol 35, 1983, pp 258 – 260.

[4] Grypnas, M., D., and Marie P., J. "Effects of Low Doses of Stronitum on Bone Quality and Quantity in Rats" *Bone* vol 11, 1990, pp 313 – 319.

[5] Grypnas, M., D., Hamilton, E., Cheung, R., Tsouderos, Y., Deloffre, P., Hott, M., and Marie, P., J. "Strontium Increases Vertebral Bone Volume in Rats at a Low Dose That Does Not Induce Detectable Mineralization Defect" *Bone* vol 18, 3, 1996, pp 253 – 259.

[6] Marie, P., J. and Hott, M. "Short-term Effects of Fluoride and Strontium on Bone Formation and Resorption in the Mouse" *Metabolism* vol 35, 6, 1986, pp 547 – 551.

[7] Skornya, S., C. "Effects of oral supplementation with stable strontium" *CMA Journal*, Vol 125, 1981 pp 703 – 712.

[8] "Protelos| European Medicines Agency" *European Medicines Agency* May 15 2020. https://www.ema.europa.eu/en/medicines/human/EPAR/protelos Accessed January 2024

[9] "Strontium ranelate (Protos) for postmenopausal osteoporosis" *NPS MedicineWise* November 1 2007. https://www.nps.org.au/radar/articles/strontium-ranelate-protos-for-postmenopausal-osteoporosis Accessed January 2024

[10] Reginster, J., Y., Deroisy, R., Dougados, M., Jupsin, I., Colette, J., and Roux, C. "Prevention of early postmenopausal bone loss by strontium ranelate: the randomized, two-year, double-masked, dose-ranging, placebo-controlled PREVOS trial." *Osteoporosis international* 13, 2002, pp 925-931.

[11] Meunier, P. J., D. O. Slosman, P. D. Delmas, J. L. Sebert, M. L. Brandi, C. Albanese, R. Lorenc et al. "Strontium ranelate: dose-dependent effects in established postmenopausal vertebral osteoporosis—a 2-year randomized placebo controlled trial." *The Journal of Clinical Endocrinology & Metabolism* 87, no. 5, 2002, pp 2060-2066.

[12] Reginster J. Y., Seeman E., De Vernejoul M. C., Adami S., Compston J., Phenekos C., Devogelaer J. P., Diaz-Curiel M., Sawicki A., Goemaere S., Sorensen O. H., Felsenberg D., and Meunier P. J. "Strontium Ranelate Reduces the Risk of Nonvertebral Fractures in Postmenopausal Women With Osteoporosis: Treatment of Peripheral Osteoporosis (TROPOS) Study" *Journal of Clinical Endocrinology and Metabolism*, vol 90, 2005, pp 2816 – 2822.

[13] Meunier P. J., Roux C., Seeman E., Ortolani S., Badurski J. E., Spector T. D., Cannata J., Balogh A., Lemmel E. M., Pors-Nielsen S., Rizzoli R., Genant H. K., and Reginster J. Y. "The Effects of Strontium Ranelate on the Risk of Vertebral Fracture in Women with Postmenopausal Osteoporosis" *New England Journal of Medicine* vol 350(5), 2004 pp 459-468.

[14] Bruyere O., Roux C., Detilleux J., Slosman D. O., Spector T. D., Fardellone P., Brixen K., Devogelaer J. P., Diaz-Curiel M., Albanese C., Kaufman J. M., Pors-Nielsen S., and Reginster J.Y. "Relationship between Bone Mineral Density Changes and Fracture Risk Reduction in Patients Treated with Strontium Ranelate" *The Journal of Clinical Endocrinology & Metabolism* vol 92(8), 2007, pp 3076-3081.

[15] Malaise O., Bruyere O., and Reginster J.Y. "Strontium ranelate normalizes bone mineral density in osteopenic patients" *Aging Clinical and Experimental Research* vol 19, 2007, pp 330 – 333.

[16] Reginster J. Y., and Meunier P. J. "Strontium ranelate phase 2 dose-ranging studies: PREVOS AND STRATOS studies" *Osteoporosis International* vol 14(Suppl 3), 2003, pp S56-S65.

[17] "Protelos and osseor – referral | European Medicines Agency" *European Medicines Agency* September 19 2014. https://www.ema.europa.eu/en/medicines/human/referrals/protelos-osseor Accessed January 2024

[18] Blake, G., M. and Fogelman, I. "Effect of Bone Strontium on BMD Measurements" *Journal of Clinical Densitometry* vol 10, 1, 2007, pp 34 – 38.

[19] Nielsen, S., P., Slosman, D., Sorensen, O., H., Basse-Cathlinat, B., De Cassin P., Roux, C., and Meunier, P., J. "Influence of Strontium on Bone Mineral Density and Bone Mineral Content Measurements by Dual X-ray Absorptiometry" *Journal of Clinical Densitometry* vol 2, no 4, 1999, pp 371 – 379.

[20] "Black-box warning for strontium ranelate (Protos) added to Product Information" *NPS MedicineWise* December 1 2014. https://www.nps.org.au/radar/articles/black-box-warning-for-strontium-ranelate-protos-added-to-product-information Accessed January 2024

[21] Moise H., Adachi, J., D., Chettle, D., R., and Pejovic-Milic, A. "Monitoring bone strontium levels of an osteoporotic subject due to self-administration of strontium citrate with a novel diagnostic tool, *in vivo* XRF: A case study" *Bone* vol 51, 2012, pp 93-97.

[22] Moise, H., Chettle, D., R., and Pejovic-Milic, A. "Monitoring bone strontium intake in osteoporotic females self-supplementing with strontium citrate with a novel in-vivo X-ray fluorescence based diagnostic tool" *Bone* vol 61, 2014, pp 48 – 54.

[23] "Summary Safety Review – Strontium – Risk of Heart and Circulatory Side Effects" *Government of Canada* October 22 2015https://www.canada.ca/en/health-canada/services/drugs-health-products/medeffect-canada/safety-reviews/summary-safety-review-strontium-risk-heart-circulatory.html Accessed January 2024

[24] "Strontium health products: New Restrictions to address possible heart and circulatory-related risks" *Health Canada* October 22 2015 https://recalls-rappels.canada.ca/en/alert-recall/strontium-health-products-new-restrictions-address-possible-heart-and-circulatory Accessed January 2024

[25] "Strontium in drinking water – Guideline Technical Document for Public Consultation" *Health Canada* July 20 2018 https://www.canada.ca/en/health-canada/programs/consultation-strontium-drinking-water/document.html Accessed January 2024

[26] Wohl, G., R., Chettle, D., R., Pejovic-Milic, A., Druchok, C., Webber, C., E., Adachi, J., D., and Beattie, K., A. "Accumulation of bone strontium measured by in vivo XRF in rats supplemented with strontium citrate and strontium ranelate" *Bone* vol 52, 2013, pp 63 – 69.

[27] Snyder R., E., and Secord D., C. "The in situ measurement of strontium content in bone using x-ray fluorescence analysis" *Physics in Medicine and Biology* vol 27, no 4, 1982, pp 515 – 529

[28] Wielpolski L., Vartsky, D., Yasumura, S., and Cohn, S., H. "Application of XRF to Measure Strontium in Human Bone In Vivo" *Advances in X-ray Analysis,* vol 26, 1982, pp 415 – 421.

[29] Pejovic-Milic, A., Stronach, I. M., Gyorffy, J., Webber, C., E., and Chettle, D., R. "Quantification of bone strontium levels in humans by in vivo x-ray fluorescence" *Medical Physics* vol 31, no 3, 2004, pp 528 – 538.

[30] Zamburlini, M., Pejovic-Milic A., and Chettle D., R. "Evaluation of geometries appropriate for 125I in vivo bone strontium X-ray fluorescence measurement" *Journal of Radioanalytical and Nuclear Chemistry*. Vol 269,3, 2006, pp 625-629.

[31] Zamburlini, M., Pejovic-Milic, A., Chettle, D., R., Webber, C., E., and Gyorffy, J. "In vivo study of an x-ray fluorescence system to detect bone strontium non-invasively" *Physics in Medicine and Biology* vol 52, 2007, pp 2107 – 2122.

[32] Da Silva, E., Pejovic-Milic, A., and Heyd, D., V. "The use of teeth as the site for the *in vivo* or *ex vivo* quantification of skeletal strontium by energy-dispersive X-ray fluorescence spectrometry: A feasibility study" *Journal of Analytical Atomic Spectrometry*, vol 23, 2008, pp 527 – 534.

[33] Heirwegh, C., M., Chettle D., R., and Pejovic-Milic A. "*Ex vivo* evaluation of a coherent normalization procedure to quantify *in vivo* finger strontium XRS measurements" *Med Phys* vol 39 (2), 2012, pp 832-841.

[34] Heirwegh, C. In Vivo Quantification of Bone Strontium Using X-Ray Fluorescence. 2008. McMaster University, MSc.

[35] Moise, H. Energy Dispersive X-ray Fluorescence Spectrometry and Kinetic Modeling of Elemental Strontium in Human Bone. 2014. McMaster University, PhD.

[36] Specht, A., J., Mostafaei, F., Lin Y., Xu., J and Nie, L., H. "Measurements of Strontium Levels in Human Bone In Vivo Using Portable X-ray Fluorescence (XRF)" *Applied Spectroscopy* Vol 71, no 18, 2017, pp 1962-1968.

[37] Gevaert, J., and Chettle D., R. "XRF analysis of strontium: Exploring cellulose as a soft tissue equivalent" *X-ray Spectrometry* vol 48, 2019, pp 443 – 451.

[38] Zhang, X., Wells, E., M., Specht, A., J., Weisskopf, M., G., Weuve, J., and Nie, L., H. "In vivo quantification of strontium in bone among adults using portable x-ray fluorescence" *Journal of Trace Elements in Medicine and Biology* vol 74, 2022, pp 127077

[39] Da Silva, E., Mankovskii, G., Kirkham, B., Groves, J., Gherase, M., Fleming, D. E. B., and Pejović-Milić, A. "Evaluation of portable x-ray fluorescence spectrometers for in vivo quantification of bone strontium

and lead on the basis of the minimum detectable limit: a phantom study." *Adv. X-Ray Anal.*, vol *61*, 2018, pp 116-121.

[40] "Bone Density Scan" *Mount Sinai Hospital* https://www.mountsinai.on.ca/care/me/bone-density-scan Accessed January 2024.

[41] "Bone density scan" *Canadian Cancer Society* https://cancer.ca/en/treatments/tests-and-procedures/bone-density-scan Accessed January 2024

[42] Bangash, S., U., K., McNeill, F., E., Farquarson, M., J., and Chettle D., R. "Feasibility of a 109Cd-based portable XRF device for measuring skin iron concentration in anaemic and beta-Thalassaemic patients" *Biomedical Physics and Engineering Express* vol 8, 2022, pp 065034.

[43] Da Silva E., Kirkham B., Heyd, D., V., and Pejovic-Milic A. "Pure Hydroxyapatite Phantoms for the Calibration of in vivo X-ray Flourescence Systems of Bone Lead and Strontium Quantification" *Analytical Chemistry* vol 85, 2013, pp 9189 – 9195

[44] Solc J., Vrba, T., and Burianova, L. "Tissue equivalence of 3D printed plastics for medical phantoms in radiology" *Journal of Instrumentation* vol 13, 2018.

[45] Bider R., C., Sheehan, B., Bock, N., and McNeill, F., E. "The Feasibility of K XRF Bone Lead Measurements in Mice using 3D-Printed Phantoms" *Biomedical Physics and Engineering Express*. Vol 10, no 3, 2024, pp 035027.

[46] Canadian Nuclear Safety Commission, *Radiation Protection Regulations SOR/2000-203,* May 29 2024. https://laws-lois.justice.gc.ca/eng/regulations/sor-2000-203/page-2.html#h-656867

Chapter 3:

3.1 Introduction to Chapter 3:

The work presented in this paper focuses on the benchmarking of a Monte Carlo model of our new in-vivo strontium XRF system, and the application of the benchmarked model to the testing of the validity of coherent normalization in strontium XRF measurements using the system described in Chapter 2. An earlier Monte Carlo model using MCNP6.2 was not pursued beyond initial testing due to issues with the cross-sectio data libraries. Benchmarking was performed through regressions of the simulated data against experimental data for each thickness and concentration of phantom.

Once the system was benchmarked, simulations of phantoms in different positions were performed. Cylindrical phantoms with a strontium concentration of 1500 ppm and simulation 'tissue' overlay thickness of 2mm were placed at varying poitions both off-axis and moving backwards from the detector. At each site, the area of the strontium Kα x-rays, and the 22.2 keV and 24.9 keV coherently scattered peaks were calculated. The Kα x-ray was then normalized to either of the 22.2 keV or 24.9 keV peak areas. The un-normalized and normalized data were then plotted against distance off-axis or back from the detector and fitted with a linear function. The slope was then tested to to determine whether it was significantly different than zero.

A similar process was repeated for a phantom of concentration of 1500 ppm, but with varying soft tissue thicknesses at a fixed distance from the detector face.

Results showed that the coherent normalization could not account for attenuation due to soft tissue overlay, however the normalization may be able to correct for changes in positioning. This combined with a previously tested Compton correlation method to estimate soft tissue thickness could potentially help reduce the variability in the XRF signal.

Benchmarking of the EGS5 code, as well as all simulations were run by myself. Data analysis was also performed by myself with guidance from Dr. Fiona McNeill. In addition, I wrote the first draft of the manuscript, with Dr. Fiona McNeill acting as editor.

Help with installation of EGS5, as well as troubleshooting, was provided by Mr. Bobby Tang, Dr. Soo Hyun Byun and Dr. Sami Bangash. Base EGS5 code was provided by Dr. Soo Hyun Byun and Mr. Bobby Tang. Help determining sampling issues with MCNP was provided by Mr. Brendan Sheehan and Ms. Renee-Claude Bider.

This article is ready for publication.

3.2 Paper 2: Validity of coherent normalization for an improved *in-vivo* strontium X-ray fluorescence (XRF) system: A simulation study

L. M. Bickley[1], F. E. McNeill[1]

[1]Department of Physics and Astronomy, McMaster University, 1280 Main Street West, Hamilton, ON, Canada L8S 4M1

Abstract

When performing in-vivo X-ray fluorescence measurements, a challenge that presents itself is the sensitivity of the system to changes in source-subject distance. These changes are influenced by the thickness of soft-tissue of the organ of interest of a volunteer or patient, and movement of patients or volunteers during measurement. These can negatively influence the precision of in-vivo measurements, and introduce inaccuracies into the data. To correct for these changes, a technique called coherent normalization was developed for in-vivo lead X-ray fluorescence. The validity of this technique lies in four criteria being fulfilled, however, in occasional cases the normalization is still considered valid even if one criterion is not met.

To check if coherent normalisation is valid for our in-vivo strontium X-ray fluorescence system, a Monte Carlo simulation was benchmarked in EGS5. After benchmarking, a phantom approximating real-world PLA phantoms (representing a human finger) was moved to various position back and off-centre from the detector face. In addition, a phantom was modelled with varying PLA overlay thicknesses to test the effect of normalization on soft-tissue overlay thickness. At each position, and overlay thickness, the area of the strontium Kα peak was normalized to either the 22.2 keV or 24.9 keV coherently scattered silver X-rays. These normalized values were then plotted against the corresponding position away from the detector, or overlay thickness. The slopes of the resulting regressions were then analysed to determine if they were significantly different from zero.

Results showed that normalization to either coherently scattered silver X-ray cannot correct for soft-tissue overlay, in agreement with previous studies. However, the normalization was able to correct for changes in position, whether they were positioned off-centre or further back from the detector.

Introduction

Use of X-ray Fluorescence to measure elements in-vivo

X-ray fluorescence (XRF) is a non-invasive technique commonly used to measure elements such as lead[11,12,22], gadolinium[16,17], lanthanum[23,24], uranium[26] and strontium[19,20,29,33,36] in-vivo. Examples of studies performed include measurements of gadolinium in volunteers who had received gadolinium-based contrast agents for MRI[16], and a pilot study measuring bone-strontium levels of a volunteer who was self-supplementing with strontium citrate over the course of 4 years[19]. Through the use of X-ray fluorescence it was shown that individuals who received gadolinium containing contrast agents, retained a significant amount of gadolinium in their bones, that remained up to 5 years after receiving them. Results from strontium measurements[19] showed that continued intake of strontium citrate correlated

with an increases in bone-strontium levels, and that those levels continued to rise even after 2 to 3 years.

The validity of coherent normalization in in vivo XRF systems

A challenge of in vivo x-ray fluorescence (XRF) measurements is that they can be particularly sensitive to changes in patient or volunteer position and to the thickness of soft tissue overlying the organ of interest. It is difficult for people to be completely immobile during a measurement, and volunteers can be a variety of shapes and sizes. Both factors can introduce inaccuracies as well as worsening the precision of in vivo measurements.

In addition, in many XRF measurements, the patient or volunteer is positioned using a fixed source to skin distance. This means that as soft tissue overlay thickness increases, the source to target organ distance changes, resulting in a smaller solid angle subtended by the source on the target organ and often a smaller solid angle subtended by the target organ on the detector. The x-ray fluorescence signal is thus reduced not only by attenuation, but by solid angle effects. These effects therefore need to be accounted for to produce an accurate measurement estimate. In theory, this can be performed through calibration against anthropomorphic phantoms. However, this can be a lengthy, costly, and impractical process, requiring multiple sets of calibration standards and a method, such as ultrasonography[19,20,29,36], for assessing the target organ position and tissue overlay thickness in every *in vivo* measurement subject. In addition, while *in vitro* or phantom based measurements can have both position and overlying soft tissue thickness more readily controlled, controlling for motion and thus position, can be difficult in *in vivo* measurements. *In vivo* XRF measurements typically take between 2[33] and 30 minutes[5,16,17,19,20,29,36] to perform, and participants may move and make small shifts in position in this length of time. As previously discussed, this can introduce inaccuracies in *in vivo* measurements and thus a method of XRF signal normalization can be extremely useful.

Ideally, a signal normalization method can be found that allows for correction of the XRF signal using data within the collected spectrum, or normalization to a feature in the spectrum that changes with position and tissue overlay thickness in exactly the same way as the XRF signal. An early example of XRF signal normalization that accounted for variations in soft tissue thickness and geometry was implemented in 1985 for *in vivo* bone lead XRF measurements using ^{109}Cd as the fluorescing source[32]. In this system, the K x-ray signals from lead are normalized to the 88 keV coherently scattered ϒ-ray emitted from ^{109}Cd, with the normalization reducing the variation in bone lead measurements to less than 1%. This normalisation generally works extremely well for XRF measurements of bone lead using ^{109}Cd because the system meets the following conditions for the validity of the normalization to a coherent scatter signal:

1. Both the fluorescence x-ray and coherent scatter signal must arise from the same incident photon fluence.

2. Both the x-ray and the coherent scatter signal must be produced in the same location in the sample.

3. The angular distribution of both signals must be the same, and;

4. The x-rays and coherent scattered ϒ-rays must be attenuated similarly through the overlying soft tissue.

If one or more of these criteria are not met, then the normalization may not be considered valid. However, there are circumstances that can arise, through a combination of factors, wherein the normalization of fluorescence x-ray signal to coherent scatter signal may still be considered valid, despite not meeting all four criteria. Examples include measurements of lead in the finger using ^{57}Co and gadolinium in tibia using ^{109}Cd.

In addition, the normalization may only be valid under specific circumstances. For example, the *in vivo* K XRF Pb lead measurements which employ ^{109}Cd[1,4,5,11,12,22,30,32,34] as the fluorescing source in a backscatter geometry have typically found that the normalization to the coherent scatter peak is valid. The argument for the validity of coherent normalisation in this system is that ^{109}Cd emits an 88.035 keV γ-ray in 3.6% of decays: this ϒ-ray is only 0.03 keV above the K absorption edge of lead at 88.005 keV. It has been calculated[31] that any Compton scatter of this γ-ray through an angle of greater than 3.6^{o} will result in scattered photon energies that are below the K absorption edge of lead. This means that the characteristic lead x-rays are predominantly produced from interactions with uncollided γ-rays. As the coherent scatter also arises from uncollided γ-rays, normalisation criterion 1 above is satisfied. In addition, the ratio of the differential coherent scatter cross section at approximately 150^{o} is 28:1 for bone to soft tissue[13,32], meaning that in human tibia measurements the majority of the coherent scatter signal comes from bone as there is more bone mass sampled which has a significantly higher cross section. Over 90% of lead is stored in bone and thus criterion 2, that the two signals arise from the same material and location, in this case bone, is satisfied[32]. Criterion 3 is considered satisfied as the lead fluorescence x-rays are emitted isotropically, and the differential coherent cross section is relatively constant for scattering angles greater than 120^{o}[32] as used in the ^{109}Cd backscatter system. Finally, criterion 4 is also considered satisfied as the differential attenuation of the 72.8 keV Pb K_{α} x-ray and the 88 keV γ-ray is only approximately 4%[32].

A number of authors have reported successfully employing the normalization for measurements of bone lead in studies *in vivo*[11,12,22,32,34] and *ex vivo*[5,30]. However, in 1999[18], it was noted that the measurement appeared to be incorrect when measuring morbidly obese young women. Recently, studies have shown that in measurements where the ratio of the mass of bone to the mass of soft tissue is significantly reduced (compared to tibia measurements in adults with Body Mass Index (BMI) values of less than 30) the usual normalization appears to fail and must be adjusted[4,31]. While the differential cross section ratio is 28:1 for bone to soft tissue, in measurements where a large soft tissue mass compared to the bone mass is sampled, e.g. in morbidly obese individuals, the proportion of the coherent scatter signal that arises from soft tissue becomes significant, and the normalization to the coherent signal is no longer a normalization to 'bone' only.

Semi-valid systems that employ coherent normalisation

As argued earlier in this article, typically if one or more of the criteria listed for coherent normalization are not met then a normalization to a coherent scatter signal cannot be considered valid. However, there are circumstances where other factors within the measurement can compensate for any unmet criteria. These may permit the normalization to be considered valid. For example, a number of systems employ coherent normalization for the measurement of gadolinium[14,15,16,17,21,23] and lanthanum[23,24], and in these systems only criteria 2 and 3 are completely valid. The gadolinium system consists of a set of four HPGe detectors in a cloverleaf formation, using a ^{109}Cd fluorescing source in a 180° backscatter geometry. The lanthanum system consists of a single HPGe detector, with a ^{241}Am source in a 180° backscatter

geometry. Criterion 1 is violated in these systems as the difference in energy between the K absorption edge of gadolinium and lanthanum (at 50.24 keV and 38.9 keV respectively) and the fluorescing photon energies (88 keV and 59.5 keV respectively) are such that any singly Compton scattered photons have energies above the K absorption edges. Criterion 4 is violated as the x-rays (at approximately 33 keV for lanthanum, and 43 keV for gadolinium) are differentially attenuated through soft tissue compared to the coherently scattered photons (which are 59.5 keV for the lanthanum system, and 88 keV for the gadolinium system). In addition, there are systems for the in vivo measurement of uranium that employ coherent normalization. The system consists of a single HPGe detector, with a ^{57}Co source in a 180°backscatter geometry. For these systems, only Criterion 1 is not valid. Similarly to the systems for gadolinium and uranium, the 122 keV photon from ^{57}Co is sufficiently above the K absorption edge of uranium (115.6 keV), that any Compton photons scattered through an angle of 40° will be above the K absorption edge of uranium[25,26].

However, it was determined that for all these systems coherent normalization was able to correct for both soft tissue overlay and positional changes experimentally, despite the systems not meeting all normalization criteria. For example, one gadolinium measurement system[14] showed that when plotting the normalized signal against a variety of soft tissue overlay thicknesses, the variation in the signal was reduced to only 2.5%. Additionally, the slope of the normalized signal versus soft tissue overlay thicknesses (ranging from 0 – 12.2mm) resulted in a slope that was statistically insignificant from zero. The normalization in this same system was then deemed successful enough that it was used to conduct pilot studies of bone gadolinium levels in two groups of volunteers[16]. One group had received gadolinium-based MRI contrast agents while the second group had not. Bone gadolinium levels were found to be different between the two groups.

An alternate setup to the ^{109}Cd system for bone lead measurement employed coherent normalization in a system that that utilized two ^{57}Co co-planar sources at 90^{o} to the detector[27,28]. The system did not meet all four criteria. The 122 keV γ-ray emitted from ^{57}Co is 49.2 keV above the lead K absorption edge. Source photons that are Compton scattered through 90^{o} have energies higher than the lead K absorption edge, so Criterion 1 is not met. Criterion 2 is met as the ratio of differential cross sections at 90^{o} for a 122 keV photon for bone and soft tissue is 40:1. Since greater than 90% of lead is stored in bone, both the lead x-rays and the coherently scattered 122 keV photons arise in the bone. Criterion 3 is not met as the lead x-rays are emitted isotropically in bone, while the coherent scatter of 122 keV photons is anisotropic. Criteria 4 is not met as the lead x-rays at 72.8 keV and the 122 keV coherent scattered γ-ray are attenuated very differently through soft tissue. However, the ^{57}Co bone lead measurement system was able to exploit the fact that while the unscattered γ-ray flux from the source decreases with depth into a sample, the scatter flux increases. That is, in the bone measurement, as the thickness of the overlying soft tissue increases, the incident number of fluorescing γ-rays at the bone decreases as the source photons are attenuated. The number of fluorescent x-rays produced in the bone from the source γ-rays decreases. However, at the same time, the flux of Compton scattered photons increases at the bone, resulting in an increase in x-ray production from Compton scattered photons, counteracting the decrease due to attenuation of source photons. Therefore, even though several criteria for coherent normalization were not met, the use of coherent normalization in this system was able to reduce the variation in x-ray signal to within 5% in terms of changes in position[28].

Table 1 provides a short summary of these in vivo XRF systems that have been able to use a normalisation of the fluorescence x-rays to coherent scatter signal.

Element	Source	Geometry	Source energy (keV)	K absorption edge (keV)	X-ray Energies (keV)	Coherent Scatter Ratio (Bone:Soft Tissue)	coherent Soft Tissue μ/ρ (cm^2g^{-1})	x-ray Soft Tissue μ/ρ (cm^2g^{-1})	Valid Criteria
U[25,26]	^{57}Co	180°	122.1	115.6	94.6 98.4 111.3	40:1	0.160	0.173 0.170 0.165	2,3 & 4
Pb[27,28]	^{57}Co	90°	122.1	88.0	72.8	40:1	0.160	0.190	2
Gd[14,15,16,17,21]	^{109}Cd	180°	88.0	50.2	43.0	28:1	0.177	0.256	2 & 3
La & Gd[23]	^{241}Am	180°	59.5	(La) 38.9	33.03 33.4	18:1	0.206	0.346 0.342	2 & 3
La[24]	^{241}Am	180°	59.5	38.9	33.03 33.4	18:1	0.206	0.346 0.342	2 & 3

Table 1: Information regarding normalization criteria for several XRF systems that utilised a normalisation despite failing to meet all four criteria.

The status of coherent normalization in in vivo bone strontium XRF systems:

The previous section details in vivo XRF systems where coherent normalization was still possible despite some criteria not being met and this leads to the question of whether a coherent normalization could work for in vivo XRF measurements of strontium in bone. The K absorption edge of strontium is at 16.1 keV, with the most intense K x-rays being emitted at 14.1 keV and 15.9 keV. Prior in vivo strontium XRF measurement systems have typically used two sources: ^{109}Cd[29] and ^{125}I[19,20,29,36].

^{125}I brachytherapy seeds that were used in prior systems emit a γ-ray of energy 35.5 keV, tellurium K x-rays at 27.2 keV and 31 keV, and as the iodine is adsorbed onto silver seeds, also silver x-rays at 22.1 keV and 24.9 keV. ^{109}Cd emits a γ-ray of energy 88.035 keV, and silver x-rays at 22.1 keV and 24.9 keV. All fluorescing energies in these systems are sufficiently above the strontium K absorption edge such that Compton scatter will result in scattered photon energies above the strontium K absorption edge. This means criterion 1 is likely not met. Further, the geometry employed for both sources has been a 180° backscatter geometry. This results in the ratio of the differential coherent cross sections for bone and soft-tissue being between 2.4:1 – 3:1, which means that Criterion 2 is not likely met[13]. A significant proportion of the coherent scatter signal arises from the soft tissue as confirmed in 2012[9] using measurements of *ex vivo* cadaver fingers. There was found to be an 18.6% difference between measurements performed with and without soft tissue. Measurements of strontium *in vivo* by XRF therefore need to have a method of determining the overlying tissue thickness in order to correct for attenuation. This has typically been performed using ultrasound.

However, criterion 3 is met, as the strontium x-rays are scattered isotropically from the bone, and the differential coherent cross section exhibits little change for scattering angles greater than 140°[13]. While

coherent normalization may not be able to correct for overlying soft tissue thickness, it may be able to correct for changes in bone geometry and source-subject distance. A phantom and simulation based study in 2008[37] found that by normalizing to the 35.5 keV gamma from ^{125}I eliminated variation in the measurements, while normalizing to the 22.1 keV silver X-ray reduced the variation to approximately 10% across a series of bone diameters. This shows that it may be possible that coherent normalization can account for differing source-subject distances. The goal of this work has thus been to investigate this possibility further for an in vivo XRF ^{109}Cd-based system for the measurement of strontium in the finger in a 180^{o} geometry.

Materials and Methods:

Initially, two Monte Carlo codes were tested for their ability to model the detection system, MCNP6 and EGS5. Preliminary tests were performed with MCNP6[35]. However, it was immediately noted that while MCNP6 was able to successfully model the coherent scatter of the silver X-rays, the modelled magnitude of the strontium Kα and Kβ were significantly less than expected from experimental phantom-based experiments. Investigation of the MCNP6 cross-section libraries determined that the cross-section data for photon interactions at low energies were not accurate as compared to tabulated values from the XCOM Photon cross-sections data base[3] maintained by the US National Institutes for Standards and Technology as has been observed by others[4,31]. Further work with MCNP6 was therefore discontinued.

The Source and Measurement Geometries

An EGS5[10] model of the experimental detection system was created that followed a simplified design of the experimental system. The experimental detector (KETEK VITUS H150 SDD) was modelled using the geometry and materials described by the manufacturer. The system consisted of a 150mm^2, 450µm thick silicon wafer, surrounded by a nickel shell, with a 25 µm beryllium entrance window. The model was then extended to include additions developed for the experimental system. For example, an aluminum cap with a 250µm polystyrene plastic window, designed to protect the beryllium window, was placed over the detector window[2]. The air gap between the styrene window and the detector was not modelled as this caused the simulation to run more slowly and could be neglected as attenuation in air would be minimal.

The ^{109}Cd source was modelled as a collimated point source, pointed along a single axis. In the system geometry, the source is aligned and pointed along the z-axis, and both the phantom and detector face are centred along the z-axis, with both extending vertically along the x-axis and horizontally along the y-axis as shown in Figure 1. The source was therefore directed along the negative z- axis. As signal from the 88 keV ϒ-rays from the source were never observed experimentally in the spectra, only the silver X-rays from the decay of ^{109}Cd were modelled. Figure 2 shows the decay scheme of ^{109}Cd which results in these x-rays. In the model, the source was placed approximately 3mm in front of the detector face, approximating the location of the source in its collimator in the experimental system.

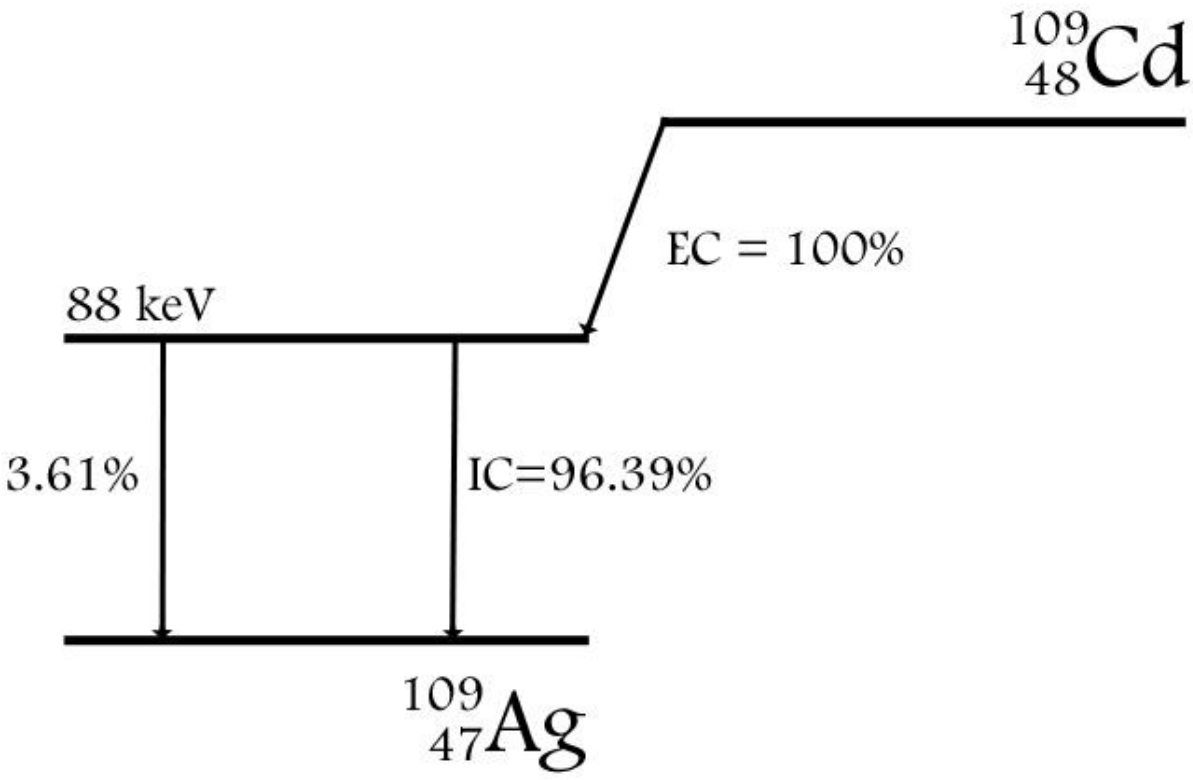

Figure 1: Decay scheme of ^{109}Cd. ^{109}Cd has a half-life of 462.6 days. X-rays emitted from the excited state of ^{109}Ag are 22.2 keV (K-$\alpha_{1,2}$), 24.9 keV (K-$\beta_{1,3}$) and 25.5 keV (K-β_2).

3D printed finger phantoms were developed for the experimental system. The inner 'bone' of these finger phantoms was modelled as strontium-doped calcium hydroxyapatite cylinders with radius 3.5mm and length 60mm. The experimental phantoms were designed with different thicknesses of PLA plastic to simulate overlying tissue. In the simulation, the different thicknesses of PLA were modelled as a cylinder over the inner bone and a 2mm PLA cap was modelled on the top of the phantom. Soft tissue thicknesses in the simulations were: 0mm, 2mm, 2.5mm, 2.9mm, 3.5mm and 4mm. The inner bone had strontium concentrations ranging from 0ppm strontium to 1500ppm strontium. The outer edge of each phantom was placed at 2mm from the source.

Strontium contamination had been a significant problem in the experimental system; phantom calibration lines were found to have a significant offset. A phantom to determine the offset of strontium contamination of the calcium hydroxyapatite was also modelled at each soft-tissue thickness. This phantom had a concentration of 950ppm strontium.

In order to accurately model the interactions in the bone region, the EGS5 code setting to produce fluorescence photons was turned on, in addition to those for Rayleigh scattering, Compton scattering and Doppler broadening. All simulations were run for a total of 10^7 source particles.

Positioning of the phantom is crucial when the strontium experimental system is calibrated by correlating the strontium Kα x-ray signal with concentration. Accurate positioning will be challenging for *in vivo* measurements where patients are likely to have slight changes in position during the course of the measurement. As mentioned in the introduction, a method of signal normalization could be extremely useful and create a much more robust clinical system. In order to test if normalization of the strontium Kα signal to the coherently scattered silver X-rays could correct for changes in position for the current experimental system, measurements at different distances from the detector were modelled. These were modelled by moving the phantom backward in the simulation from the initial starting position at additional distances of 2mm, 4mm, 6mm, 8mm and 10m). In addition, the phantoms were modelled at positions offset from the centre of the detector at ±3mm, ±2mm, and ±1mm off-axis for four of the modelled backward distances: 0mm,2mm,4mm, and 6mm.

Benchmarking of the model:

In order to see if the simulations were able to accurately model the real-world response of the detector system, tests were performed to see if experimental signals correlated to signals from the model. The strontium Kα x-ray peak area was normalized to the coherently scattered 22.2 keV silver X-ray area for each phantom concentration and PLA overlay thickness for both experiment and simulation. The normalized simulation data was plotted against the normalized experimental data and tested to see if the experimental and simulation data were linearly correlated and thus whether simulation could be used to predict experimental results. Experiments had been performed using two sources of different activity for two different counting periods. Regressions of simulation to experiment were performed for all four sets of experimental data.

Data from the simulation that was not measured experimentally was then evaluated. Peak areas for the simulated strontium Kα, and coherently scattered 22.2 keV and 24.9 keV silver X-rays were first normalized to the corresponding peak are from Source 1 with 5 minute measurements. This was done to create a conversion factor between simulation and experiment. This conversion factor was applied before the next steps.

The peak areas of the strontium Kα x-rays and the coherently scattered 22.2 keV and 24.9 keV silver X-rays were extracted from the model output and the ratio of the Kα peak area to each of the 22.2 and 24.9 coherently scattered Ag X-rays peak areas were then calculated at each position. These ratios were then plotted for each soft tissue thickness at the corresponding on-axis and off-axis position to determine whether the ratio was invariant with position.

The slope of the ratio of Kα x-ray to coherent scatter signal for each phantom overlay thickness was then calculated using a weighted linear regression in OriginPro 2024, and the slopes were tested to see if they were significantly different from 0. It was assumed that a slope of 0 would be an indication that there was no significant variation in the normalized signal with position, thus a slope of 0 would show that the normalization could correct for geometric shifts.

Z-scores were calculated (EQ 1) to test whether slopes were significantly different from 0, with x being the estimated slope of the line, μ being 0, and σ being the uncertainty of the estimated slope:

$$Z = \frac{x-\mu}{\sigma} \quad (1)$$

The corresponding p-value for a given Z-score was then determined using lookup tables. The variation in slope was considered to be significantly different from zero at the 95% confidence interval for a two-tailed test.

The Z-score determines whether the slope is significantly different from zero in absolute terms. However, this is a stringent requirement. Small variations in slope could be significantly different than zero yet produce an estimate of strontium concentration that would be within the experimental uncertainties of the 'true' value and could provide an estimate that is less dependent on geometry changes than estimates obtained using the strontium Kα x-ray signal alone. The normalized estimate could therefore prove useful under certain circumstances.

Given a value of the slope of the plot of the x-ray to coherent normalization of $m \pm \delta m$, then the values of $m \pm \delta m$ could be compared to the values of the experimental data and the individual measurement uncertainty. For example, if the slope were to show an absolute increase in the estimated concentration of 5% , but the individual measurement uncertainty is 10%, then the normalization could be considered to work in practice.

Results and Discussion:

Benchmarking:

Figure 2 shows a comparison between the spectrum obtained in EGS5 versus the spectrum obtained via experiment for a 1500ppm Sr phantom with 2mm soft tissue overlay. As can be seen in Figure 2, while the general characteristics of each spectrum are similar, there are differences in some relative peak heights. (The horizontal scale differs due to the method of energy binning in EGS5). The Kα and Kβ x-ray peaks appear with sufficient magnitude in the simulated spectrum, and in the correct position, and the behaviour of the coherently scattered silver X-rays and Compton scattered silver X-rays is as expected. As can be seen from Table 2, and Figure 3 the EGS5 simulations correlate and thus calibrate well with the experimental data.

There are differences between the model and experiment that include the relative height of the coherently scattered 22.2 keV Ag x-ray. This is likely due to the experimental source encapsulation which differentially attenuates signals. It had been previously found (Chapter 2) that small differences in source encapsulation led the observed differences in the relative heights of Kα x-rays, Kβ x-rays and coherent scatter signal in the spectra, when two different source encapsulations were compared. The ratio of Kα x-ray signal to Kβ x-ray signal was modelled in EGS5 as the theoretical value of ~6.2:1 while the ratio is lower in the experiment. Due to these differences, the benchmarked model cannot be directly compared on a per emitted photon basis to real-world experiments. However, for the purposes of this work, the Monte Carlo model is sufficient because it was determined that experimental and simulated signals could be correlated to each other and thus the simulation could be used to predict experimental changes. Table 2 shows how well the EGS5 simulation results correlated with the experimental data.

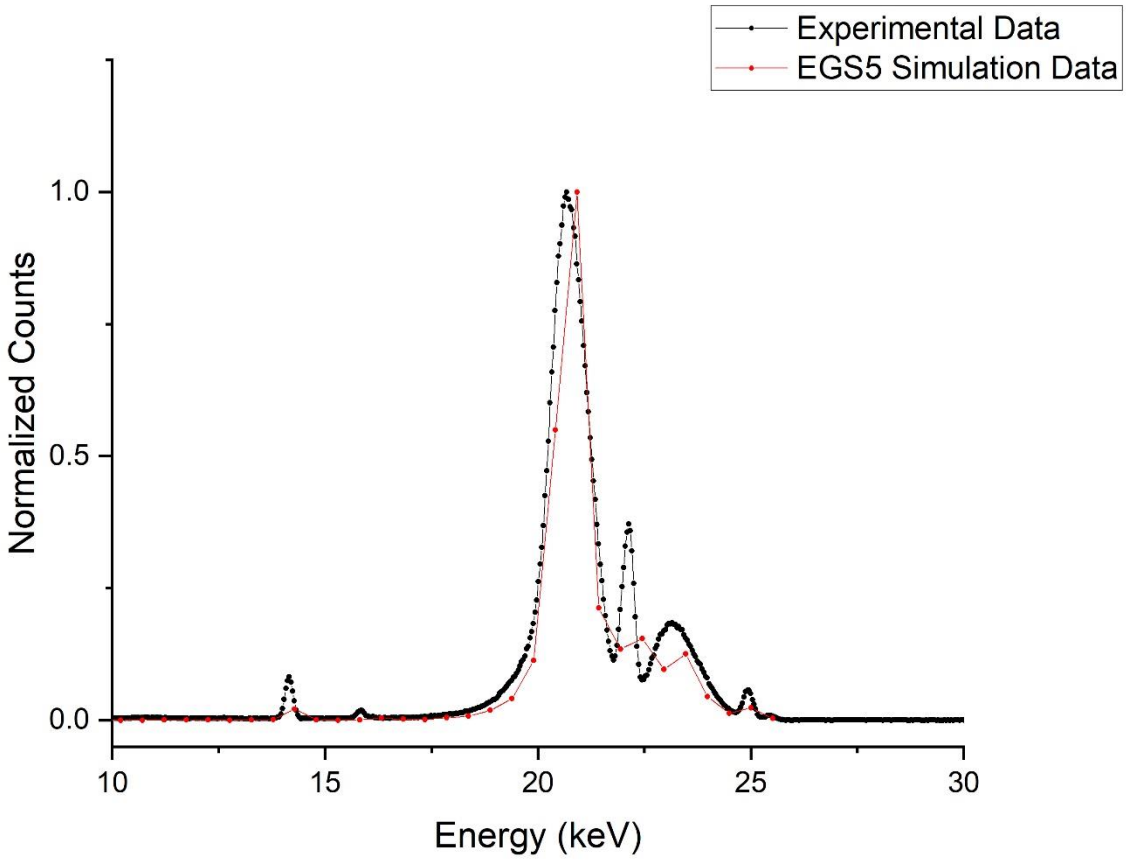

Figure 2: Observed experimental spectrum (black) for a 5 minute measurement using a ^{109}Cd source, with a nominal activity of 79.82 MBq at time of measurement (April 2023). The measured phantom had a concentration of a 1500 µg Sr/g Ca with a PLA soft tissue overlay thickness of 2mm. EGS5 simulation of a 1500 µg Sr/g Ca finger phantom (red), a PLA soft-tissue equivalent plastic and a calcium hydroxyapatite (HaP) bone-equivalent core. The PLA soft tissue overlay thickness was 2mm, and the number of particles run in the simulation was 10^7.

	Slope	Intercept	R^2	p-value
Source 1 5 minute	0.79 ± 0.04	0.013 ± 0.003	0.98	<0.0001
Source 1 30 minute	0.77 ± 0.04	0.016 ± 0.002	0.98	<0.0001
Source 2 5 minute	0.38 ± 0.04	0.017 ± 0.005	0.92	<0.0001
Source 2 30 minute	0.39 ± 0.03	0.019 ± 0.003	0.96	<0.0001

Table 2: Correlation data for the slope, intercept and R^2 for regressions of Monte carlo model signal estimates versus experimental signal estimates for a 2mm PLA soft tissue overlay thickness phantom,

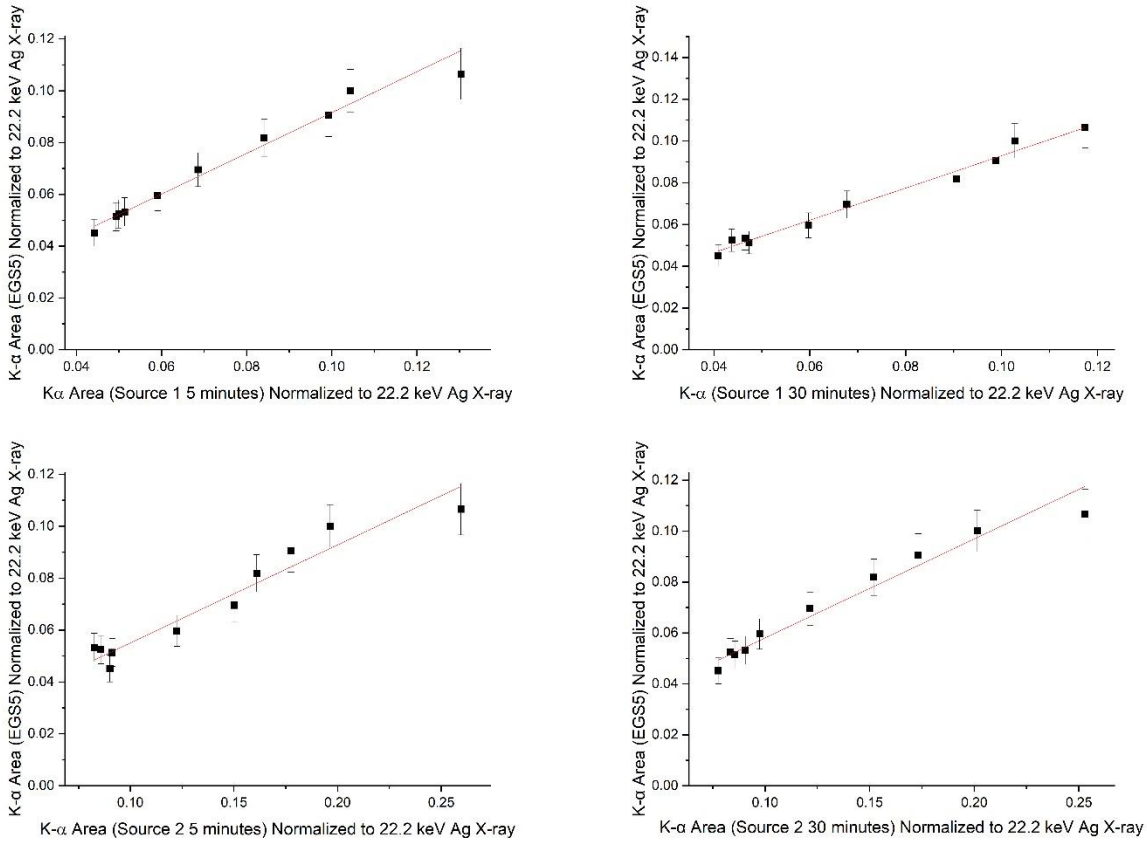

Figure 3: Regressions of EGS5 simulation versus experiment for two different experimental source strengths and two different counting times.

Coherent Normalisation and Soft Tissue Thickness Correction:

Table 3 below shows the slopes, Z-scores, and p-values of the regression of signal versus soft-tissue thickness for a 1500ppm Sr phantom at a fixed position directly in front of the source. The slopes of all regressions of signal versus phantom tissue overlay thickness are significantly different from zero, showing that the ratio changes with tissue thickness and thus normalization of the strontium Kα signal to coherent scatter signals cannot account for signal changes due to attenuation and scatter in soft tissue. Additional methods are required to correct XRF signals for soft tissue overlay.

Signal	Slope	Z-value	P-value
Kα x-ray peak area	-1651±341.	-4.84	<0.00001
Kα x-ray peak area to 22.2 keV coherent scatter peak area	-0.0190±0.004	-4.96	<0.00001
Kα x-ray peak area to 24.9 keV coherent scatter peak area	-0.186±0.043	-4.32	0.000015

Table 3: Results of regression of strontium signals versus soft tissue overlay thickness.

Coherent normalization and phantom position, centered, moving back from detector

Tables 4 and 5 below show the results of the regression of the normalized strontium x-ray signal versus position moving back from the detector for the 22.2 keV and the 24.9 keV silver X-rays respectively. These results suggest that the normalization cannot completely account for all changes in position for all phantoms using either the coherently scattered 22.2 or 24.9 keV signals. However, as discussed earlier, this testing the normalization against a very stringent criterion. In all cases, the difference between the initial value (at '0mm' position) to the value furthest back from the detector at 10mm, the difference was found to not be significant and thus the change is unlikely to be observed experimentally (see Tables 6 and 7).

Figures 4A and 4B show the variation of the normalized signals with distance back from the detector for a phantom with a soft tissue overlay thickness of 2mm PLA, while Figure 4C shows the variation of the Kα signal over the same distances (see Appendix for data for all overlay thicknesses). As can be seen, and as expected, there is strong downward trend of the Kα x-ray signal with distance from the detector. The trend is not strongly observed for the normalized signals. Normalization to either coherent scatter signal would thus be an improvement over estimates made using an uncorrected strontium Kα x-ray signal.

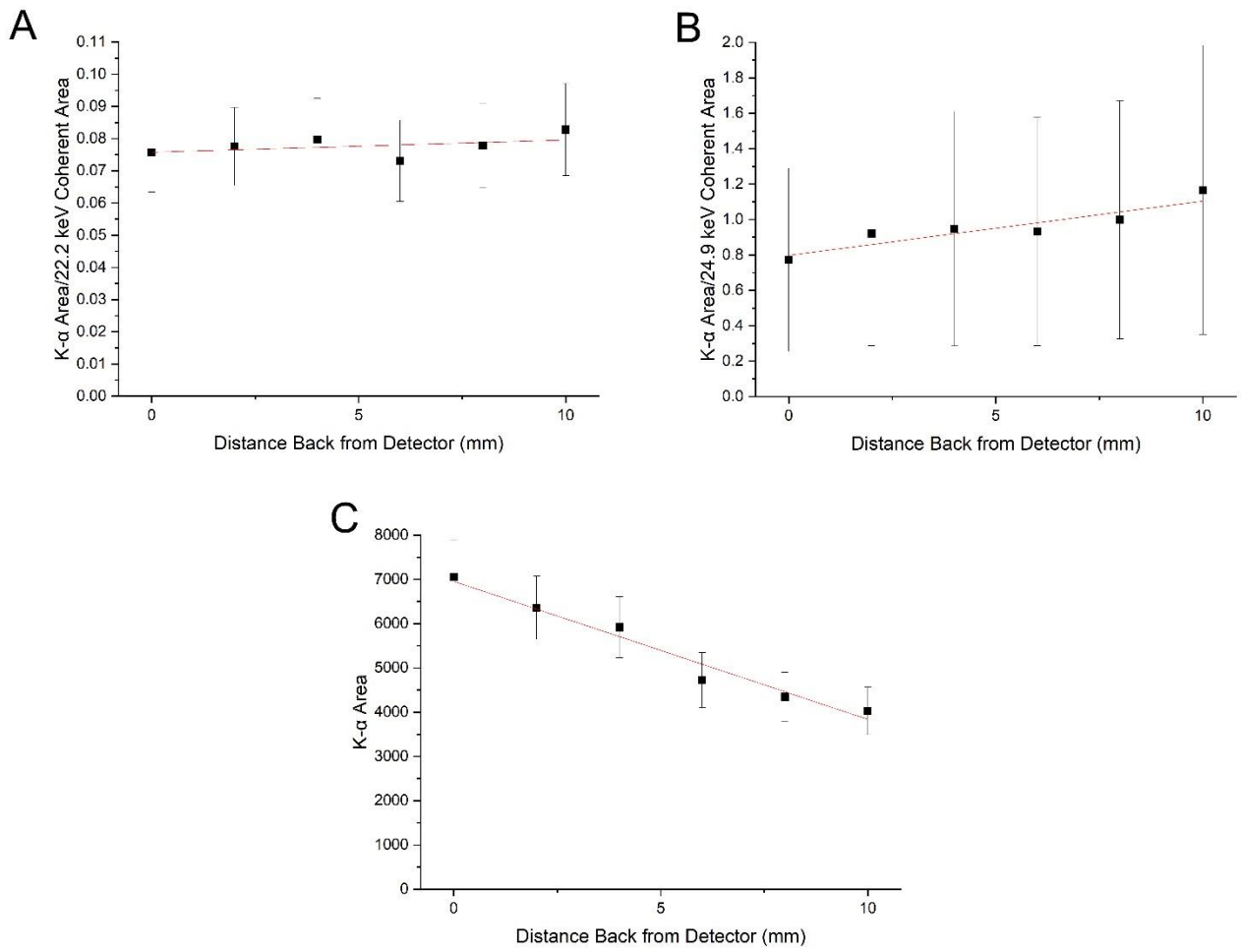

Figure 4: Regressions of strontium Kα peak normalized to 22.2 keV coherently scattered silver X-ray (A), 24.9 keV coherent scattered silver X-ray (B), or not normalized (C) vs distance back from detector. Simulated with a concentration of 1500ppm and PLA overlay thickness of 2mm.

Soft Tissue Thickness	Slope (x 10^{-4})	Z-value	P-value (two-tail)
0	-8.84 ±8.56	-1.03	0.303
2	3.81± 3.91	0.976	0.329
2.5	10.8 ± 4.11	2.63	0.009
2.9	8.20 ±2.01	4.09	< 0.001
3.5	6.35 ±2.73	2.33	0.020
4.0	4.93 ±3.35	1.47	0.142

Table 4: Results of the regression of x-ray to coherent ratio versus distance back from the detector for an EGS5 simulation of the Kα strontium signal normalized to the coherently scattered 22.2 keV Ag X-ray signal for different PLA soft tissue thickness overlays for a 1500ppm Sr phantom. The phantom was moved back from the start position (3mm from detector face) by 2mm, 4mm, 6mm, 8mm and 10mm respectively.

Soft Tissue Thickness	Slope	Z-value	P-value
0	0.0276±0.0116	2.38	0.017
2	0.0307±0.0066	4.63	<0.001
2.5	0.0257±0.0045	5.67	<0.001
2.9	0.0198±0.0116	1.71	0.087
3.5	0.0222±0.0036	6.20	<0.001
4.0	0.0113±0.0032	3.49	< 0.001

Table 5: Results of the regression of x-ray to coherent ratio versus distance back from the detector for an EGS5 simulation of the Kα strontium signal normalized to the coherently scattered 24.9 keV Ag X-ray signal for different PLA soft tissue thickness overlays for a 1500ppm strontium phantom. The phantom was moved back from the start position (3mm from detector face) by 2mm, 4mm, 6mm, 8mm and 10mm respectively.

	Initial Value of ratio	Value of ratio at 10mm from detector	Difference
2.5	0.0529±0.0083	0.0689±0.0120	0.0160 ± 0.0146
2.9	0.0402±0.0070	0.0498±0.0097	0.0097±0.0120
3.5	0.0344±0.0073	0.0405±0.0086	0.0061±0.011

Table 6: Values of the strontium Kα x-ray signal normalized to the 22.2 keV Ag X-ray signal at the initial position in front of the detector and at the final position 0mm further back, and the difference between them. No difference is statistically significant. Experimental uncertainties mean the change would not be observed.

	Initial Value of ratio	Value of ratio at 10mm from detector	Difference
0	2.013±1.456	2.343±1.737	0.3302±2.267
2	0.7722±0.5168	1.167±0.816	0.395±0.966
2.5	0.5439±0.3834	0.8753±0.6656	0.331±0.768
3.5	0.3530±0.2446	0.5956±0.4143	0.243±0.481
4	0.2773±0.1920	0.3942±0.2848	0.117±0.343

Table 7: Values of the strontium Kα signal normalized to the 24.9 keV Ag X-ray signal at initial position and final position 10mm further back, and the difference between them. No difference is statistically significant and experimental measurement uncertainties mean the change would not be observed.

Distances Off-Axis from Detector:

Tables 8 and 9 provide a summary of results of the regression of the strontium x-ray to coherent ratio versus position off-axis from the detector. Table 8 shows the slopes, Z-values and p-values for a phantom with 2mm soft-tissue overlay thickness for the normalization to the 22.2 keV silver X-ray, Table 9 shows the same data for the normalization to the 24.9 keV Ag X-ray.

The results are similar to those found from regression of x-ray to coherent ratio versus distance back from the detector. While some slopes are significantly different from zero, no difference between the centre and outer position is statistically significant as shown in Table 10 and experimental uncertainties mean the change would not be observed in a single measurement. Data for all other soft-tissue overlay thicknesses can be found in the supplemental material.

Normalization of the strontium Kα x-ray signal to either coherent scatter signal would provide a more robust measurement that would reduce inaccuracies introduced by patient motion and positioning. Further evidence for this is shown in Figures 5A and 5B which plot the strontium Kα to coherent ratios for different distances back from the detector and offset from the detector centre for the 22.2 keV, and 24.9 keV normalizations respectively, while Figure 5C shows the change in the strontium Kα x-ray signal with off-axis distance. As can be seen from these figures, normalization to the coherent scatter signal reduces the variation in the signals with off-axis distance compared to the x-ray signal alone.

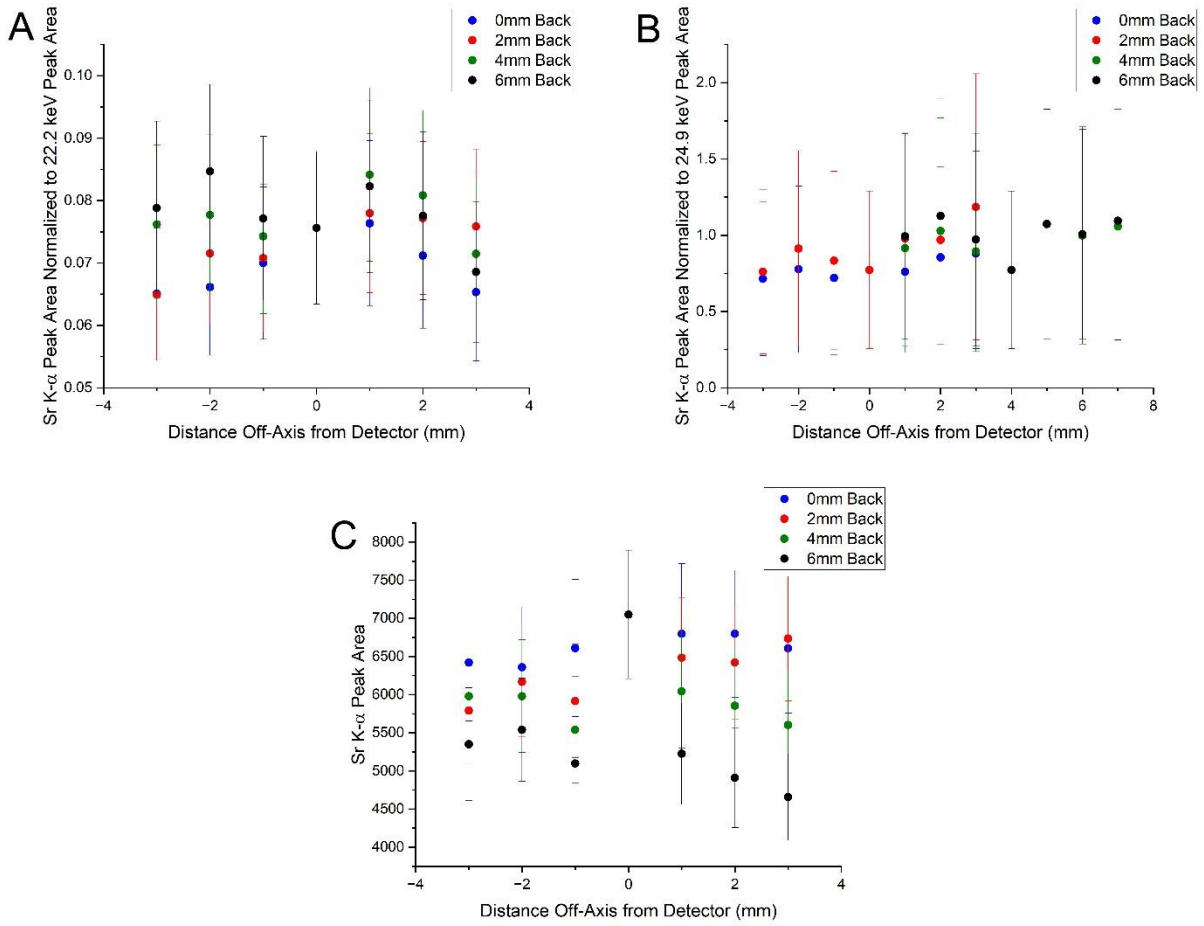

Figure 5: Regressions of strontium Kα peak normalized to 22.2 keV coherently scattered silver X-ray (A), 24.9 keV coherent scattered silver X-ray (B), or not normalized (C) vs distance off-centre from detector. Simulated with a concentration of 1500ppm and PLA overlay thickness of 2mm.

Distance Back from Detector Face (mm)	Slope (x 10^{-4})	Z-value	P-value
3	5.73±8.73	0.66	0.512
5	19.1±4.89	3.91	< 0.001
7	-0.82±8.41	-0.098	0.922
9	-16.2±8.37	-1.94	0.053

Table 8: Results of the regression of x-ray to coherent ratio versus distance back from the detector for an EGS5 simulation of the Kα strontium signal normalized to the coherently scattered 22.2 keV Ag X-ray signal for a phantom with 2mm PLA soft tissue thickness overlays for a 1500ppm strontium phantom. The phantom was set at 0mm, 2mm, 4mm and 6mm from start position (3mm, 5mm, 7mm and 9mm from detector face) and moved off axis 1mm, 2mm and 3mm in either direction.

Distance Back from Detector Face (mm)	Slope (x 10^{-4})	Z-value	P-value
3	237±71.5	3.31	<0.001
5	476±196	2.43	0.0153
7	175.9±244	0.72	0.471
9	51.5±295	0.17	0.861

Table 9: Results of the regression of x-ray to coherent ratio versus distance back from the detector for an EGS5 simulation of the Kα strontium signal normalized to the coherently scattered 24.9 keV Ag X-ray signal for a phantom with 2mm PLA soft tissue thickness overlays for a 1500ppm strontium phantom. The phantom was set at 0mm, 2mm, 4mm and 6mm from start position (3mm, 5mm, 7mm and 9mm from detector face) and moved off axis 1mm, 2mm and 3mm in either direction.

Distance Back from Detector Face (mm)	Initial Value of Ratio	Value of Ratio 3mm right of the centre of the detector face	Difference
5[a]	0.076±0.012	0.076±0.012	0.00±0.017
3[b]	0.772±0.517	0.879±0.622	0.107±0.809
5[b]	0.772±0.517	1.19±0.873	0.418±1.01

Table 10: Values of the strontium Kα signal normalized to the either the 22.2 keV (a), or the 24.9 keV (b) Ag X-ray signal at initial position and final position (at varying distances from detector face), 3mm off-centre, and the difference between them for a phantom with 2mm PLA overlay thickness. No difference is statistically significant and experimental measurement uncertainties mean the change would not be observed.

Discussion

The EGS5 Monte Carlo model was successfully benchmarked against the experimental system. There were observed differences in spectral shape. For example, there were significant differences between the amplitude of the coherent 22.2 keV peak between simulation and experiment. However, regressions of the Monte Carlo normalised signals against experimental normalized signals found the simulation results were highly correlated with the experimental data. It was therefore inferred that changes in the model could be used to predict experimental changes.

Normalisation of the strontium Kα x-ray signals to coherent scatter signals was not able to correct for overlying tissue thickness. These results for the soft-tissue correction are not surprising, as previous results from Monte Carlo simulation performed by Zamburlini et al. 2008[37] and experimental results from Heirwegh et al. 2012[9], showed that while coherent normalization may be capable of correcting for bone size and geometry, it was unable to correct for soft-tissue attenuation. This is most likely due to the fact that the ratio of the differential cross sections for coherent scatter at ~180^{o} are [2.4 is bone and 1 is soft tissue?] 2.4:1 for 22.2 keV and 2.6:1 for 24.9 keV respectively. This means that the coherent signal is

not coming primarily only from bone but is rather a combination of scattering from both soft-tissue and bone. If coherent normalization is to be used for in vivo strontium XRF measurements, then the thickness of the soft-tissue will need to be measured and corrected separately. A Compton correction method[8] previously tested on this experimental system (Paper 1/Chapter 3) could be used for this correction. While this means employing a multi-step method to account for both soft tissue overlay thickness and position/motion, from a patient point of view it is simpler as it means one visit for measurement, rather than the two required if ultrasound were employed.

The normalization was, however, found to correct for changes in geometry, both for changes in position as the phantoms was moved back from the source and for positions off-centre from the detector. The ability to correct for position would provide significant benefit for the system as the patient would not need to be restrained for the measurement, leading to more comfort for the patient. It also means shorter appointment times as less time has to be spent by technical staff on positioning the patient.

Conclusion:

A benchmarked Monte Carlo model of a new in vivo bone strontium XRF measurement system has determined that while normalization of the strontium Kα x-ray signal to coherent scatter signals cannot correct for soft-tissue attenuation, it can correct for changes due to position, leading to more accurate and robust measurements. Soft tissue thickness correction can achieved through an alternative method: Compton scattering correction. Using a two-step methodology, both soft tissue and positioning effects can be corrected using only information available in the measurement spectrum. This will obviate the necessity of adjunct measurements, such as ultrasound, reducing the time and costs associated with an in vivo XRF measurement of strontium.

Supplemental Material:

PLA Overlay Thickness (mm)	Slope (x 10^{-4})	Z-value	P-value
0	-27.8±15.4	-1.81	0.071
2	5.73±8.73	0.66	0.512
2.5	-6.29±11.5	-0.55	0.584
2.9	-1.62±6.59	-0.25	0.803
3.5	-5.23±4.55	-1.15	0.250
4.0	-2.58±7.49	-0.35	0.726

Table S1: Results of the regression of x-ray to coherent ratio versus distance back from the detector for an EGS5 simulation of the Kα strontium signal normalized to the coherently scattered 22.2 keV Ag X-ray signal for different PLA soft tissue thickness overlays for a 1500ppm strontium phantom. The phantom was set at start position (3mm from detector face), and moved off axis 1mm, 2mm and 3mm in either direction.

Soft Tissue Thickness	Slope (x 10^{-4})	Z-value	P-value
0	-33.5±7.93	-4.22	< 0.001
2	19.1±4.89	3.91	< 0.001
2.5	3.75±13.2	-0.59	0.558
2.9	9.81±2.6	-3.77	< 0.001
3.5	-7.84±6.86	-1.14	0.253
4.0	-3.37±5.75	-0.59	0.558

Table S2: Results of the regression of x-ray to coherent ratio versus distance back from the detector for an EGS5 simulation of the Kα strontium signal normalized to the coherently scattered 22.2 keV Ag X-ray signal for different PLA soft tissue thickness overlays for a 1500ppm strontium phantom. The phantom was set at 2mm from start position (5mm from detector face), and moved off axis 1mm, 2mm and 3mm in either direction.

Soft Tissue Thickness	Slope (x 10^{-4})	Z-value	P-value
0	-10.5±11	-0.096	0.924
2	-0.82±8.41	-0.098	0.922
2.5	-9.04±10.5	-0.86	0.389
2.9	3.86±7.22	0.54	0.593
3.5	-5.25±7.35	-0.71	0.475
4.0	-0.86±3.93	-0.22	0.827

Table S3: Results of the regression of x-ray to coherent ratio versus distance back from the detector for an EGS5 simulation of the Kα strontium signal normalized to the coherently scattered 22.2 keV Ag X-ray signal for different PLA soft tissue thickness overlays for a 1500ppm strontium phantom. The phantom was set at 4mm from start position (7mm from detector face), and moved off axis 1mm, 2mm and 3mm in either direction. No values are statistically significant from zero.

Soft Tissue Thickness	Slope (x 10^{-4})	Z-value	P-value
0	16.6±8.35	1.99	0.047
2	-16.2±8.37	-1.94	0.053
2.5	-11.3±12.1	-0.93	0.350
2.9	1.95±9.16	0.21	0.831
3.5	-1.74±9.08	-0.19	0.849
4.0	1.77±6.52	0.27	0.786

Table S4: Results of the regression of x-ray to coherent ratio versus distance back from the detector for an EGS5 simulation of the Kα strontium signal normalized to the coherently scattered 22.2 keV Ag X-ray signal for different PLA soft tissue thickness overlays for a 1500ppm strontium phantom. The phantom was set at 6mm from start position (9mm from detector face), and moved off axis 1mm, 2mm and 3mm in either direction.

Soft Tissue Thickness	Slope (x 10^{-4})	Z-value	P-value
0	-711±226	-3.14	0.002
2	237±71.5	3.31	<0.001
2.5	36.6±72.1	0.51	0.542
2.9	22.9±58	0.39	0.697
3.5	1.82±45.7	0.04	0.968
4.0	-35.9±67.6	-0.53	0.596

Table S5: Results of the regression of x-ray to coherent ratio versus distance back from the detector for an EGS5 simulation of the Kα strontium signal normalized to the coherently scattered 24.9 keV Ag X-ray signal for different PLA soft tissue thickness overlays for a 1500ppm strontium phantom. The phantom was set at start position (3mm from detector face), and moved off axis 1mm, 2mm and 3mm in either direction.

Soft Tissue Thickness	Slope (x 10^{-4})	Z-value	P-value
0	-871±245	-3.55	<0.001
2	476±196	2.43	0.0153
2.5	132±98.6	1.34	0.1800
2.9	240±44.5	-5.40	<0.001
3.5	-47±123	-0.39	0.699
4.0	-12±56.7	-0.22	0.827

Table S6: Results of the regression of x-ray to coherent ratio versus distance back from the detector for an EGS5 simulation of the Kα strontium signal normalized to the coherently scattered 24.9 keV Ag X-ray signal for different PLA soft tissue thickness overlays for a 1500ppm strontium phantom. The phantom was set at 2mm from start position (5mm from detector face), and moved off axis 1mm, 2mm and 3mm in either direction.

Soft Tissue Thickness	Slope (x 10^{-4})	Z-value	P-value
0	-394.6±126	-3.13	0.002
2	175.9±244	0.72	0.471
2.5	-18.9±124	-0.15	0.878
2.9	63.9±217	0.29	0.768
3.5	-64.8±139	-0.46	0.642
4.0	41.9±57.2	0.73	0.464

Table S7: Results of the regression of x-ray to coherent ratio versus distance back from the detector for an EGS5 simulation of the Kα strontium signal normalized to the coherently scattered 24.9 keV Ag X-ray signal for different PLA soft tissue thickness overlays for a 1500ppm strontium phantom. The phantom was set at 4mm from start position (7mm from detector face), and moved off axis 1mm, 2mm and 3mm in either direction.

Soft Tissue Thickness	Slope (x 10^{-4})	Z-value	P-value
0	194±150	1.29	0.196
2	51.5±295	0.17	0.861
2.5	-40.1±154	-0.26	0.794
2.9	350.7±46.6	7.53	<0.00001
3.5	-44.2±213	-0.21	0.835
4.0	31.8±83.2	0.38	0.702

Table S8: Results of the regression of x-ray to coherent ratio versus distance back from the detector for an EGS5 simulation of the Kα strontium signal normalized to the coherently scattered 24.9 keV Ag X-ray signal for different PLA soft tissue thickness overlays for a 1500ppm strontium phantom. The phantom was set at 6mm from start position (9mm from detector face), and moved off axis 1mm, 2mm and 3mm in either direction.

	Initial Value of Ratio	Value of Ratio 3mm right of the centre of the detector face	Difference
0mm Overlay – 2mm Back	0.222±0.035	0.213±0.034	0.009±0.049
2mm Overlay - 2mm Back	0.076±0.012	0.076±0.012	0.00±0.017
2.9mm Overlay - 2mm Back	0.040±0.007	0.036±0.007	0.004±0.009
0mm Overlay - 6mm Back	0.222±0.035	0.224±0.038	0.002±0.052

Table S9: Values of the strontium Kα signal normalized to the 22.2 keV Ag X-ray signal at initial position, and final position (at varying distances from detector face), 3mm off-centre, and the difference between them. No difference is statistically significant and experimental measurement uncertainties mean the change would not be observed.

	Initial Value of Ratio	Value of Ratio 3mm right of the centre of the detector face	Difference
0mm Overlay - 0mm Back	2.013±1.46	1.83±1.37	0.183±2.002
2mm Overlay - 0mm Back	0.772±0.517	0.879±0.622	0.107±0.809
0mm Overlay – 2mm Back	2.013±1.46	1.94±1.46	0.073±2.06
2mm Overlay – 2mm Back	0.772±0.517	1.19±0.873	0.418±1.01
2.9mm Overlay – 2mm Back	0.396±0.268	0.432±0.297	0.036±0.524
0mm Overlay – 4mm Back	2.013±1.46	2.17±1.55	0.157±2.13
2.9mm Overlay – 6mm Back	0.396±0.268	0.526±0.369	0.130±0.456

Table S10: Values of the strontium Kα signal normalized to the 24.9 keV Ag X-ray signal at initial position and final position (at varying distances from detector face), 3mm off-centre, and the difference between them. No difference is statistically significant and experimental measurement uncertainties mean the change would not be observed.

References:

[1] Aro, A.,C.,A. et al. “Improvements in the calibration of 109Cd K x-ray fluorescence systems for measuring bone lead *in vivo*” *Phys. Med. Biol.* vol 39 1994 pp 2263-2271.

[2] Bangash, S., U., K., McNeill, F., E., Farquarson, M., J., and Chettle D., R. “Feasibility of a 109Cd-based portable XRF device for measuring skin iron concentration in anaemic and beta-Thalassaemic patients” *Biomedical Physics and Engineering Express* vol 8, 2022, pp 065034.

[3] Berger, M.J., et al. (2010), *XCOM: Photon Cross Section Database* (version 1.5). [Online] Available: http://physics.nist.gov/xcom [2021, July 4]. National Institute of Standards and Technology, Gaithersburg, MD.

[4] Bider R., C., Sheehan, B., Bock, N., and McNeill, F., E. “The Feasibility of K XRF Bone Lead Measurements in Mice using 3D-Printed Phantoms” *Biomedical Physics and Engineering Express*. Vol 10, no 3, 2024, pp 035027.

[5] Chettle, D., R. et al. “Lead in Bone: Sampling and Quantification Using K X-Rays Excited by 109Cd” *Environmental Health Perspectives* vol 91, 1991, pp 49-55.

[6] Da Silva E., Kirkham B., Heyd, D., V., and Pejovic-Milic A. “Pure Hydroxyapatite Phantoms for the Calibration of in vivo X-ray Flourescence Systems of Bone Lead and Strontium Quantification” *Analytical Chemistry* vol 85, 2013, pp 9189 – 9195

[7] Da Silva, E., and Pejovic-Milic, A., “Calibration of the ^{125} I-induced x-ray fluorescence spectrometry-based system of in vivo bone strontium determinations using hydroxyapatite as a phantom material: a simulation study” *Physiological Measurement*. vol. 38, no 6, 2017, pp 1077-1093.

[8] Gevaert, J., and Chettle, D., R. “XRF analysis of strontium: Exploring cellulose as a soft tissue equivalent” *X-ray Spectrometry*, vol. 2019, no. 48, pp 443-451.

[9] Heirwegh, C., M. et al. “Ex vivo evaluation of a coherent normalization procedure to quantify in vivo finger strontium XRS measurements” *Medical Physics*vol 39, no 2, 2012, pp 832 – 841

[10] Hirayama, H., Yoshihito, N., Bielajew, A., F., Wilderman, S., J,., and Nelson, W., R. The EGS5 Code System. SLAC-R-730. 2005.

[11] Hoppin, J. A., et al. “Validation of K-XRF bone lead measurement in young adults” *Environmental Health Perspectives*, vol 103, no 1, 1995, pp 78 – 83.

[12] Hu H. et al. “The use of K X-ray fluorescence for measuring lead burden in epidemiological studies: high and low lead burdens and measurement uncertainty” *Environmental Health Perspectives* vol 94, 1991, pp 107-110.

[13] Hubbell, J., H. et al. “Relativistic atomic form factors and photon coherent scattering cross sections” *Journal of Physical and Chemical Reference Data* vol 8 no 1, 1979, pp 69-105.

[14] Keldani, Z et al. "Coherent normalization for *in vivo* measurements of gadolinium in bone" *Physiological Measurement* vol 38 2017 pp 1848-1858.

[15] Lord, M., L. et al. "Confirming improved detection of gadolinium in bone using in vivo XRF" *Applied Radiation and Isotopes* vol 12, 2017, pp 111 – 118.

[16] Lord M., L. et al. "Observed deposition of gadolinium in bone using a new noninvasive in vivo biomedical device: results of a small pilot study" *Radiology,* Vol 287, 2017, pp 96 – 103.

[17] Lord M., L. et al. "Self-identified gadolinium toxicity: comparison of gadolinium in bone and urine to health gadolinium-based contrast agent exposed volunteers" *Physiological Measurement*, vol 39, 2018, pp 115008.

[18] McNeill FE, Stokes L, Chettle DR, Kaye WE. "Factors affecting in vivo measurement precision and accuracy of 109Cd K x-ray fluorescence measurements." *Physics in Medicine & Biology*, vol 44, no 9, 1999 pp 2263.

[19] Moise, H., et al "Monitoring bone strontium levels of an osteoporotic subject due to self-administration of strontium citrate with a novel diagnostic tool, in vivo XRF: A case study" Bone vol 51, 2012, pp 93-97.

[20] Moise, H. et al. "Monitoring bone strontium intake in osteoporotic females self-supplementing with strontium citrate with a novel *in-vivo* X-ray fluorescence based diagnostic tool" *Bone* vol 61 2014 pp 48-54.

[21] Mostafaei, F., McNeill, F., E., Chettle, D., R., and Noseworthy, M., D. "A feasibility study to determine the potential of in vivo detection of gadolinium by x-ray fluorescence (XRF) following gadolinium-based contrast-enhanced MRI" *Physiological Measurement* vol 36, 2015 pp N1 – N13
Nguyen, J. et al. "Ex vivo quantification of lanthanum and gadolinium in post-mortem human tibiae with estimated barium and iodine concentrations using K x-ray fluorescence" *Physiological Measurement* vol 40, 2019, pp

[22] Nie, H. et al. "In vivo investigation of a new 109Cd γ-ray induced K-XRF bone lead measurement system" *Physics in Medicine and Biology*, vol 51, 2006, pp 351 – 360.

[23] Nguyen, J. et al. "Ex vivo quantification of lanthanum and gadolinium in post-mortem human tibiae with estimated barium and iodine concentrations using K x-ray fluorescence" *Physiological Measurement*, vol 40, 2019 pp 085006.

[24] Nguyen J. et al. "Investigating coherent normalization and dosimetry for the 241Am-La K XRF system" *Physiological Measurement* vol 41, 2020, pp 1-15.

[25] O'Meara, J., M. et al. "The feasibility of measuring bone uranium concentrations in-vivo using source excited K x-ray fluorescence" *Physics in Medicine and Biology*, vol 42, pp 1109.

[26] O' Meara J., M., Chettle, D., R., McNeill, F., E., and Webber C., E. "In Vivo X-ray Fluorescence (XRF) Measurement of Uranium in Bone" *Applied Radiation and Isotopes* vol 49, 5/6, 1998a, pp 713 – 715.

[27] O'Meara, J., M. et al. "Monte Carlo simulation of source-excited in vivo x-ray fluorescence measurements of heavy metals" *Physics in Medicine and Biology* vol 43, 1998b, pp 1413 – 1428.

[28] O'Meara J., M. et al. "Normalisation with coherent scatter signal: improvements in the calibration procedure of the 57Co-based in vivo XRF bone-Pb measurement" *Applied Radiation and Isotopes* vol 54, 2001, pp 319-325.

[29] Pejovic-Milic, A., et al. "Quantification of bone strontium levels in humans by *in vivo* x-ray fluorescence" *Medical Physics* vol 31, no 3, 2004, pp 528-538.

[30] Rebocho, J. et al. "Lead post-mortem intake in human bones of ancient populations by 109Cd based X-ray fluorescence and EDXRF" *Talanta,* vol 70, 2006, pp 957 – 961.

[31] Sheehan, B. Investigation of the Potential Effects of Bone Turnover on X-ray Fluorescence Measurements of Bone Lead in Young Women. 2022. McMaster University, MSc.

[32] Somervaille, L., J. et al. "*In vivo* measurement of lead in bone using x-ray fluorescence" *Physics in Medicine and Biology* vol 30, no 9, 1985, pp 929-943.

[33] Specht, A., J., Mostafaei, F., Lin Y., Xu., J and Nie, L., H. "Measurements of Strontium Levels in Human Bone In Vivo Using Portable X-ray Fluorescence (XRF)" *Applied Spectroscopy* Vol 71, no 18, 2017, pp 1962-1968.

[34] Todd, A., C. et al. "In vivo X-ray fluorescence of lead in bone using K X-ray excitation with 109Cd sources: radiation dosimetry studies" *Environmental Research*, vol 57, 1992, pp 117 – 132.

[35] Werner, Christopher John, Jeffrey S. Bull, Clell Jeffrey Solomon, Forrest B. Brown, Gregg Walter McKinney, Michael Evan Rising, David A. Dixon et al. *MCNP version 6.2 release notes*. No. LA-UR-18-20808. Los Alamos National Laboratory (LANL), Los Alamos, NM (United States), 2018.

[36] Zamburlini, M., et al. "In vivo study of an x-ray fluorescence system to detect bone strontium non-invasively" Physics in Medicine and Biology vol 52, 2007, pp 2107-2122.

[37] Zamburlini, M., et al. "Coherent normalization of figure strontium measurements: feasibility and limitations" *Physics in Medicine and Biology* vol 53, 2008, pp N307-N313.

Chapter 4:

4.1 Introduction to Chapter 4:

This paper focuses on determining a possible best radioisotope source for *in vivo* strontium XRF measurements using the previously benchmarked EGS5 Monte Carlo simulation described in Chapter 3.

Based on calculations using simulated spectra, as well as considerations of availability and practicality of use, ^{103}Pd was identified as the best potential alternative radioisotope to ^{109}Cd or ^{125}I used in previous systems. In addition, a hand geld portable XRF system (an X-ray gun) with a rhodium target was also identified as a potential alternative to prior portable XRF systems that employed molybdenum targets. Overall, Hand held XRF systems are likely the best option for in vivo XRF measurements of strontium in bone, although this is suggested noting the caveat that there are regulatory hurdles for clinical implementation of hand held XRF systems in Ontario.

The idea of using Monte Carlo simulations to investigate the best possible source for *in vivo* strontium XRF measurements was suggested by Dr. Eric Da Silva. Simulations were run by myself using a previously benchmarked EGS5 simulation. Analysis was also completed by myself with help and guidance from Dr. Fiona McNeill. The first draft of the manuscript was written by myself with Dr. Fiona McNeill serving as primary editor, and Dr. Eric Da Silva serving as secondary editor.

This article is ready for publication.

4.2 Paper 3: Determining the optimal fluorescence source for in-vivo X-ray Fluorescence measurements of strontium in bone

L. M. Bickley[1], E. Da Silva[2], F. E. McNeill[1]

[1]Department of Physics and Astronomy, McMaster University, 1280 Main Street West, Hamilton, ON, Canada L8S 4M1

[2]Department of Physics, Toronto Metropolitan University, 350 Victoria Street, Toronto, ON, Canada M5B 2K3

Abstract

X-ray fluorescence is a non-destructive and non-invasive technique that has been used to perform in vivo elemental analysis of lead, gadolinium and strontium amongst other elements. When performing X-ray fluorescence on a particular element, the choice of an optimum fluorescence source depends on a number of factors. These include; how far in energy the fluorescing source is above the element's K or L absorption edge; whether other X- or y-rays are emitted that may obfuscate the spectrum and unnecessarily increase dose; how easy the source is to obtain; the half-life of the source; and whether scattered X- or y-rays in the source that may overlap in energy with the X-ray peaks of the element being investigated.

This article describes a Monte Carlo study that systematically investigates a series of possible sources for the measurement of strontium in bone in vivo, with the goal of determining sources that could improve upon current measurement systems. A previously benchmarked EGS5 model an experimental in-vivo strontium XRF measurement system was used to test source energies ranging from 17.2 keV to 21.7 keV to see which source energies maximized the strontium XRF signal. A systematic search was then conducted to find potential radioisotope sources whose emitted energies corresponded to the 'ideal' energy range. Simulations of each source that included all emission energies up to 100 keV were then performed.

These data were then analyzed taking into not only the acquired spectra but also the availability and practicality of potential sources. The conclusion is that ^{103}Pd is a promising alternative to the ^{109}Cd and ^{125}I used in prior systems Overall, Monte Carlo studies suggest best performance could be obtained using a portable X-ray gun with a molybdenum target. However, this implementation of this x-ray set based system would resulting higher doses and would be challenging due to human use regulations in certain jurisdictions.

Keywords: Monte Carlo modelling, strontium, bone, x-ray fluorescence, 103Pd, EGS5

Introduction

X-ray Fluorescence (XRF) is a non-destructive, non-invasive technique that can be applied to the measurement of elemental concentrations in vivo[6]. It has been used in human studies to measure several elements including lead[1], gadolinium[19], lanthanum[28], and strontium[30]. The design of an in vivo XRF system is critical as the goal is to maximize the elemental x-ray signal from the person while minimizing the radiation dose. There are several factors that must be considered in the design of the system. XRF requires a source of fluorescing photons that is aimed at the target material. This can be placed such that the resulting x-ray spectrum is measured at several possible angles relative to a specific choice of x- or γ-ray detector.

The choice of an optimum fluorescing source for XRF requires consideration of several of these factors, but the most critical choice is probably the energy of the fluorescing photons from the source. The elemental x-ray signal obtained from XRF measurement of a sample is directly proportional to the probability of a photoelectric interaction. This probability is highest for the K-shell of a given atom, with the highest probability being for a photon just above the element's K absorption edge[5,10,31]. There is no possibility of the interaction below the absorption edge, and as the incoming photon energy increases above the edge the probability of interaction decreases. The magnitude of the elemental signal is thus reduced as the source photon energy increases beyond the absorption edge. The scatter spectrum produced by the fluorescing source must also be considered as this can be a source of interference with, or can result in a significant background under, the elemental signal resulting in poor signal to noise ratios. Furthermore, an ideal source has fluorescing source photon energies that will not scatter such as to produce x-rays incident on the detector that are of the same energy as the fluorescent x-rays of the element being investigated.

Fluorescing photons can be produced by either x-ray sets or radioisotopes. If the fluorescing photons are from a radioactive source, the half-life of the source must therefore also be considered and ideally the radioisotope half-life is long enough such that it should not need frequent replacement or require half-life adjustments during a measurement series. Further, an ideal radioisotope source should not emit γ-rays that contribute to dose while adding little additional signal. Finally, the production method and availability of the radioisotope also needs to be taken into consideration.

Measurements of strontium in vivo are of particular interest due to the relationship between strontium and bone mineral density (BMD). Large scale clinical trials of strontium ranelate (named in the clinical trial literature as PREVOS[32], STRATOS[21], SOTI[22], TROPOS[33]) were able to show that strontium ranelate increased the BMD of patients, while also reducing the number of fractures. This is of particular importance as BMD is considered a clinical marker of osteoporosis[17]. If an individual has a BMD that is statistically significantly lower than that of a reference 'general population', then they may be diagnosed with osteoporosis, indicating an increased risks of fractures from even minor falls[16]. However, BMD values may be inflated in these in vivo trials, as studies on rats showed that ingestion of strontium caused an overestimation of the BMD by 1.5 times compared to those who did not ingest strontium[3,27].

Additionally, the use of strontium ranelate was restricted in the EU[9] and Australia[29] in 2014 after reports of adverse cardiac events. Strontium ranelate is currently not approved for use in Canada, although other strontium compounds such as strontium citrate are available in health food stores across the country. Some women diagnosed with osteoporosis choose to self-supplement with strontium citrate. In

vivo studies[23,24] on volunteers taking strontium citrate over the course of 4 years showed strontium levels continually increased over time, instead of plateauing as previously hypothesized. It may be important to monitor strontium levels in those who take strontium supplements for two reasons. First, the health consequences of self-supplementation are not known and second, people self-supplementing may have their BMD overestimated, creating the potential for undiagnosed cases of osteoporosis in this population.

Two radioisotope sources have been previously studied for the measurement of bone strontium in vivo: ^{109}Cd[30] and ^{125}I[13,23,24,30,41]. In addition, the x-rays from a handheld or portable (p)XRF system have also been employed[34,42]. These x-ray sources have proven to be useful and have been applied in measurements of strontium in vivo.

In vivo measurements of strontium were first performed in animal studies in the 1980s[35,40], with the first in vivo human measurements being performed in the early 2000s with a system that employed a ^{125}I source[30,41]. These initial systems provided useful information on strontium and bone health. A pilot study[23] measuring the bone strontium concentrations of Canadian women self-supplementing with strontium citrate was able to show that bone strontium levels may not plateau after 2 to 3 years as previously hypothesized. A continuation[24] of this initial study that recruited an additional 9 volunteers, further confirmed that volunteers who were self-supplementing with strontium citrate over a 4-year period had bone strontium concentrations that continually increased over time. After these initial studies, further systems were employed. These used portable XRF, (p)XRF, that employ an x-ray tube with a silver target as the x-ray source, to measure the bone strontium concentrations of children[34] and adults[42] in China. Average concentrations of 79.1 ppm strontium were found in the measured adult population[34], and 43.2 ± 57.6 ppm strontium in children[42]. Additionally, a correlation was found between age and bone strontium concentration in the female participants only[42].

However prior tested sources have limitations. For ^{109}Cd radioisotope sources and (p)XRF systems with a silver target, the main fluorescing photon energies are the silver K x-rays at 22.2 keV and 24.9 keV which are 6.1 keV and 8.8 keV respectively above the K absorption edge of strontium and consequently have photoelectric cross-sections for strontium that are 41% and 32% of the maximum just above the edge. While it is possible for Compton scattered photons from 22.2 and 24.9 keV phantoms to be of high enough energy to fluoresce strontium, the cross section for the interaction is relatively low at these energies, and interactions with Compton scattered photons will lead to only small increases in the strontium fluorescent signal.

The gamma-ray emission of ^{125}I is even further in energy above the strontium K absorption edge. However, ^{125}I decays via electron capture to an excited state of ^{125}Te, which results in not only the emission of a γ-ray of energy 35.5 keV but also a series of K x-rays of energy 31.0 keV, 27.5 keV and 27.2 keV[7,15]. In addition, the ^{125}I sources used in prior XRF systems have been sources initially developed for brachytherapy. The ^{125}I in these brachytherapy sources is adsorbed onto silver and thus the 22.2 keV and 24.9 K x-rays from silver are also emitted. All these x- and γ-rays are above the K absorption edge of strontium and are thus able to fluoresce strontium. However, the relative emission of the γ- and x-rays from these brachytherapy sources depends on the proprietary nature of the source design and is thus complex and challenging to predict analytically.

As previously discussed, handheld XRF ‘guns’ have been used in in vivo XRF measurement studies of strontium in bone[8,34,42]. These systems have the advantage of being highly portable and as they do not

use radioisotopes there is no challenge from radioisotope decay. More importantly, these in vivo XRF strontium systems have shown the best performance to date, likely due to the combination of a high x-ray fluence and high throughput silicon drift detectors (SDDs). However, the handheld XRF system designs are proprietary, and difficult to obtain, thus making it challenging to understand the factors like x-ray target material, detector design, and x-ray fluence and x-ray filtration that lead to better performance than radioisotope systems. It is thus also difficult to determine how designs could be better optimized for human application. In some jurisdictions, such as Ontario, Canada, handheld XRF system use is tightly regulated, and they are not approved for application in human studies. Approvals for human use in research studies would require a lengthy (years-long) application process that so far researchers have considered to have too high an opportunity cost to implement. Finally, these systems can also deliver high doses to skin relative to radioisotope systems in a short amount of time, e.g. 21 mSv in 120s to a $1cm^2$ area[34,42]. This is equivalent to approximately 42% of the maximum annual skin dose permitted to a member of the general public from non-medical radiation exposure in Canada. In comparison, radioisotope-based systems deliver a skin dose of approximately 1.1 mSv to a $0.8cm^2$ area in $1800s$[2].

While these systems have shown useful application in research studies, the choice of sources has been somewhat opportunistic and there has not, to date, been a systematic study aimed at determining an 'ideal' source for the in vivo measurement of strontium by XRF. The goal of this work has been to conduct that systematic study to see if there are x- or γ- ray sources that could be employed that may further improve the in vivo measurement of strontium.

Methods

X-ray Signal Prediction using a Monte Carlo Model

A previously benchmarked EGS V Monte Carlo[12] model of the in vivo measurement of strontium was adapted for this work (see Chapter 3). Initial simulations aimed at determining the ideal source energy for in vivo measurements of strontium in bone were performed by varying the incident fluorescing energy in increments of 0.5 keV from 16.2 keV to 21.7 keV. This range was chosen as it starts just above the strontium K absorption edge of 16.1 keV and continues until just below the energy of the silver $K\alpha_1$ x-ray emitted by ^{109}Cd sources that have previously been studied. This ensures that the source energy is high enough that electrons can be ejected from the strontium K shell and thus strontium K x-ray emission is possible and provides a wide range of energies that do not overlap with the most recently tested strontium K XRF source and system setup (see Chapter 3).

The Monte Carlo model was of an experimental system described in detail in prior work (Chapter 2). In short, the modelled experimental setup consists of a KETEK H150 SDD detector, with a 450 mm^2 by 250 µm thick Si detector with a 25 µm Be entrance window, overlaid with a 250 µm polystyrene cap. In the simulations used in this determination of an ideal source, two geometries were modelled: one with a source at 90° to the detector and one with a source at 180° to the detector. Both geometries modelled a single finger phantom of concentration 1500 µg Sr/g Ca with a 2mm polylactic acid (PLA) tissue overlay thickness. For the 180° geometry, the edge of the phantom was set at 2mm from the surface of the source, centered on the detector face. For the 90° geometry, the phantom and detector positions were kept as in the 180° geometry, and the collimated source was placed at an angle of 90° to the detector. Each fluorescing energy in each geometry was run for 1×10^7 particles.

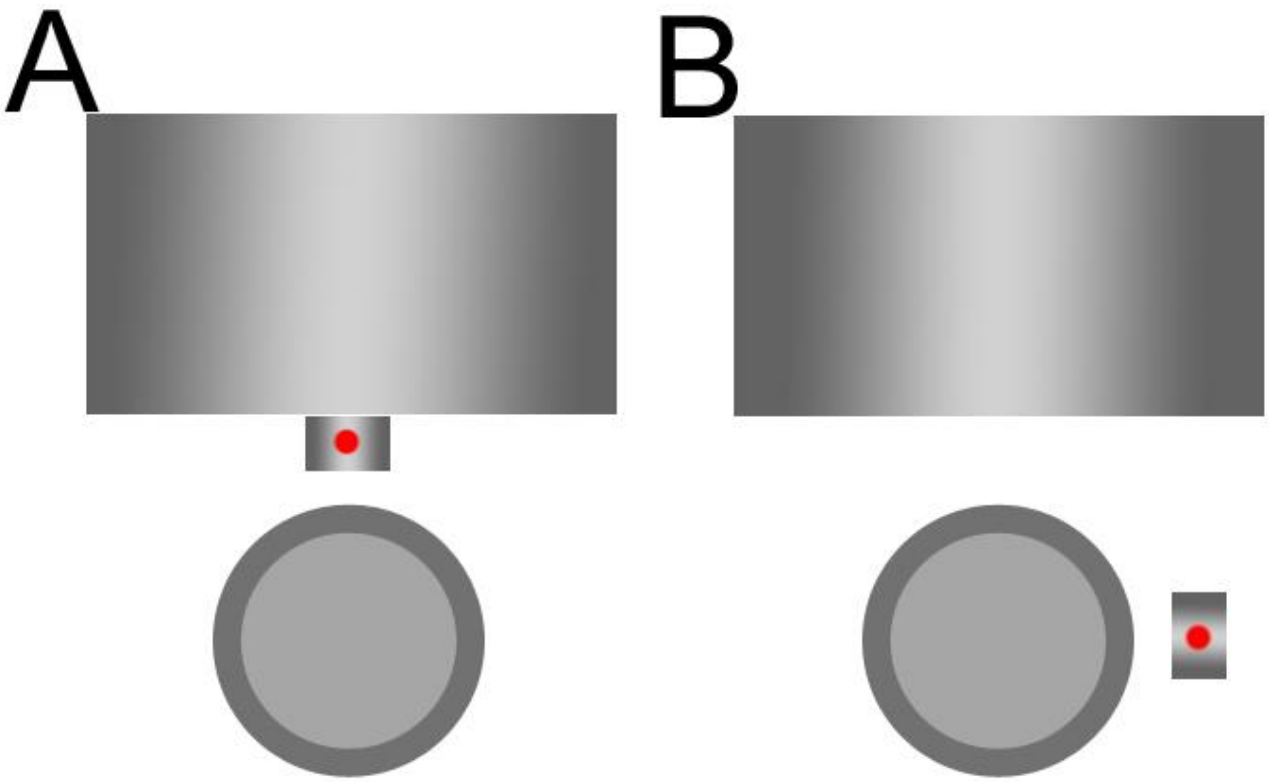

Figure 1: Schematic of source geometries simulated in EGS5. A is the 180° geometry, B is the 90° geometry. Source positions are denoted by a red dot.

The goal was to identify geometries and energies that maximise the strontium K x-ray signal. The strontium K x-ray signals were calculated from the EGS output as the area of the 14.1 keV strontium K_α x-ray peak with subtraction of a linear background. A second goal was to identify geometries and energies that resulted in features in the spectrum at the energy of the K_α peak that would either interfere with the signal, or create a significant background, thus worsening the signal to noise ratio.

Isotope Identification

Once the 'ideal' energy had been determined using the Monte Carlo model, two nuclear decay databases from Lund University[5] and the International Atomic Energy Agency[15] were searched to find isotopes that had x- or ϒ-ray emission energies close to the determined 'ideal' energy range. These specific isotopes were then modelled within the EGS5 simulation, first with x- and γ-rays up to 40 keV, then again with additional x- and γ-rays (up to 100 keV) emitted from these isotopes included.

Two x-ray set sources were also modelled. The K x-rays from molybdenum and rhodium targets were modelled as the fluorescing source. These models assumed that an x-ray set could potentially be filtered to eliminate energies below the target characteristic x-rays. This also permitted modelling for isotopes that decayed to molybdenum and rhodium.

Convolution of Signal and Background Calculation

In order to better approximate the background under the strontium Kα and Kβ peaks, the signal was convolved with a single Gaussian with a FWHM of 0.2 keV. This FWHM was determined from the resolution of the detector.

Results and Discussion

Ideal Energy:

Below are tables for the Kα x-ray areas, the position of the Compton scatter peak and data on the signal to background ratios that depend on the Compton peak position relative to the Kα x-ray. The 'ideal' energy range was found to be greater than or equal to 18.2 keV as this is where the background under the strontium Kα x-ray peak is reduced and the signal to background signal improves. The isotopes identified within this 'ideal' energy range of 18.2 keV to 21.7 keV are summarized in Table 3 below. Any x- or ϒ-rays with emission probabilities of less than 1% were excluded from the model, and photon energies above 100 keV were also not included.

The x-rays from molybdenum and rhodium were also modelled. While molybdenum x-rays are slightly less than 18.2 keV, it is a popular target material for portable XRF systems[11].

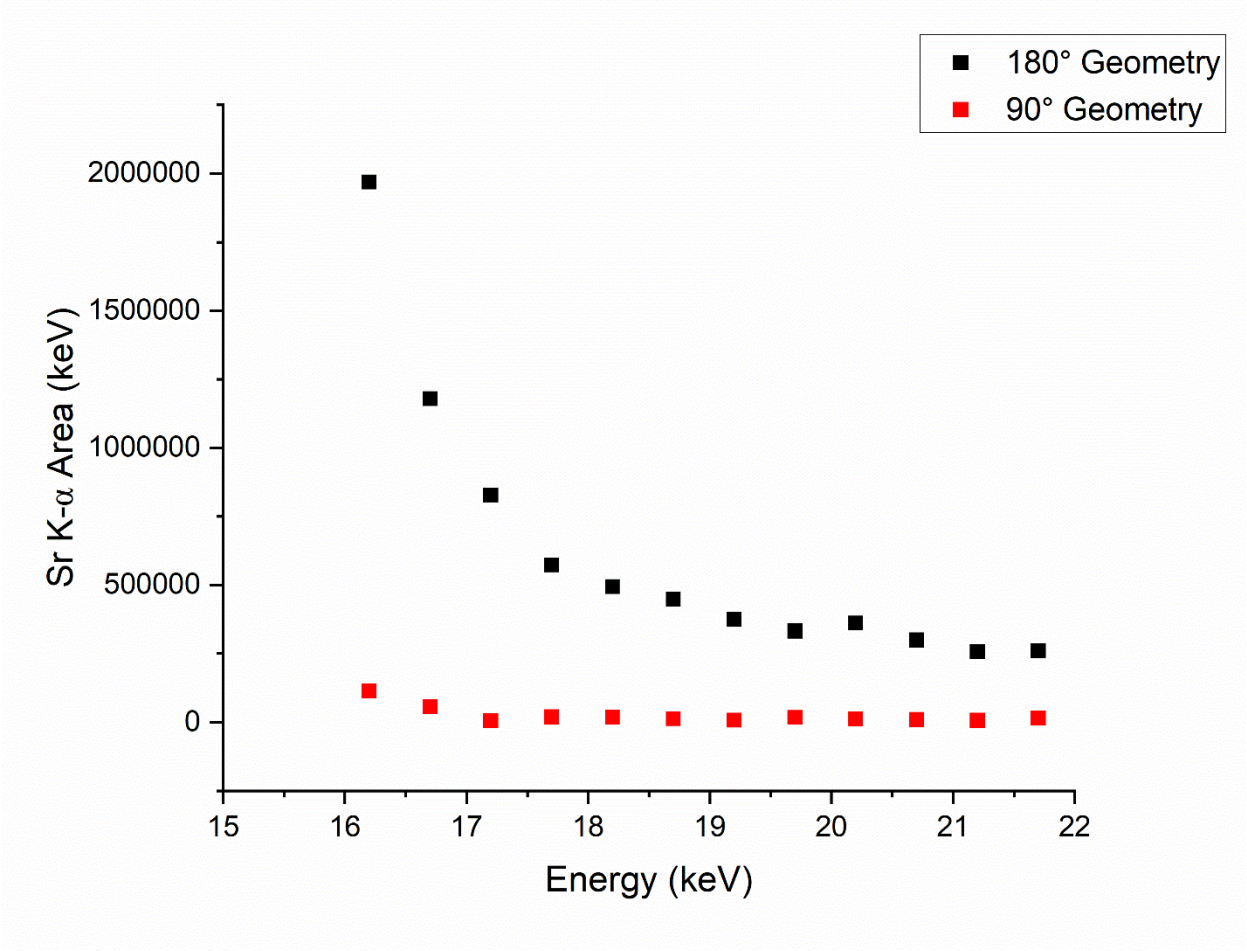

Figure 2: Magnitude of the modelled strontium Kα x-ray signal for each fluorescing source photon energy for both 180° and 90° degree geometries.

Energy (keV)	Peak of Compton Distribution (keV)	Relative Size of Compton background under K-α Peak (Signal:Background)	Relative Size of Compton background under K-β Peak (Signal:Background)
16.2	15.23	1.03	1.18
16.7	15.68	3.70	1.39
17.2	16.12	2.63	0.90
17.7	16.55	5.26	1.33
18.2	16.99	55.6	1.43
18.7	17.42	29.4	1.59
19.2	17.86	35.7	1.35
19.7	18.29	29.4	1.28
20.2	18.72	111	2.50
20.7	19.15	18.2	2.22
21.2	19.58	71.4	2.44
21.7	20.00	500	3.23

Table 1: Simulated photon energies and the resulting signal to background ratio for a 180°geometry.

Energy (keV)	Peak of Compton Distribution (keV)	Relative Size of Compton background under strontium Kα Peak (Signal:Background Ratio)	Relative Size of Compton background under strontium Kβ Peak (Signal:Background Ratio)
16.2	15.79	2.94	1.69
16.7	16.17	0.847	1.18
17.2	16.64	0.286	1.24
17.7	17.11	3.12	1.34
18.2	17.57	9.09	1.17
18.7	18.04	90.9	1.40
19.2	18.50	333	1.48
19.7	18.96	2.50×10^3	1.67
20.2	19.43	2.94×10^4	1.25
20.7	19.89	1.69×10^5	1.33
21.2	20.36	7.69	2.50
21.7	20.82	111	1.71

Table 2: Simulated fluorescing source photon energies and the resulting signal to background ratio for a 90° geometry.

A list of isotopes identified as being close to the ideal fluorescing energy, with their x- or ϒ-ray energies, intensities and half-lives are shown in Table 3.

Isotope	Decay	Photon Energies (keV)	Absolute Intensity (%)	Half-Life
^{112}Pd	Beta-	**Gammas** 18.5	**Gammas** 100	21.03 h
^{103}Pd	EC and Beta+	**Gammas** 39.748 **X-rays** 2.892 20.073 20.215 22.8 22.96 23.2	**Gammas** 0.0683 **X-rays** 8.73 22.09 41.83 11.36 13.25 1.89	16.991 d
^{171}Lu	EC and Beta+	**Gammas** 19.394 27.133 75.889 667.422* 739.793* **X-rays** 51.354 52.389 59.5 60	**Gammas** 14 0.789 6.19 11.2 48.7 **X-rays** 34.6 60.9 20.2 25.2	8.247 d
^{142}Xe	Beta-	**Gammas** 12.9 19.77 20.80 23.95 33 38.83 46.13 57.5 57.9 70.1 72.86 94.6	**Gammas** 1.5 32 135 40 0.3 233 50 0.14 14 24 274 15	1.22 s
^{180}Os	EC and Beta+	**Gammas** 20.1 **X-rays** 59.7 61.13 69.5 70 71.2	**Gammas** 100 **X-rays** 11 change these 19 6 8 1.8	21.5 min
^{181}Ir	EC and Beta+	**Gammas** 19.6	**Gammas** 6.0	4.90 min

		65.3 93.88 102.7* 107.64*	20 29 25 100	

Table 3: Isotopes modelled in by the EGS code. ϒ- and x-ray energies that were not included in the Monte Carlo model are marked by *. Data were taken from IAEA[15] and Lunds[7].

As predicted by the Klein-Nishina formula, the model determined that the 90° measurement geometries had Compton scatter distributions that were smaller relative to K x-ray emissions, with a 90° scatter being approximately 50% less likely than scatter through 180°.

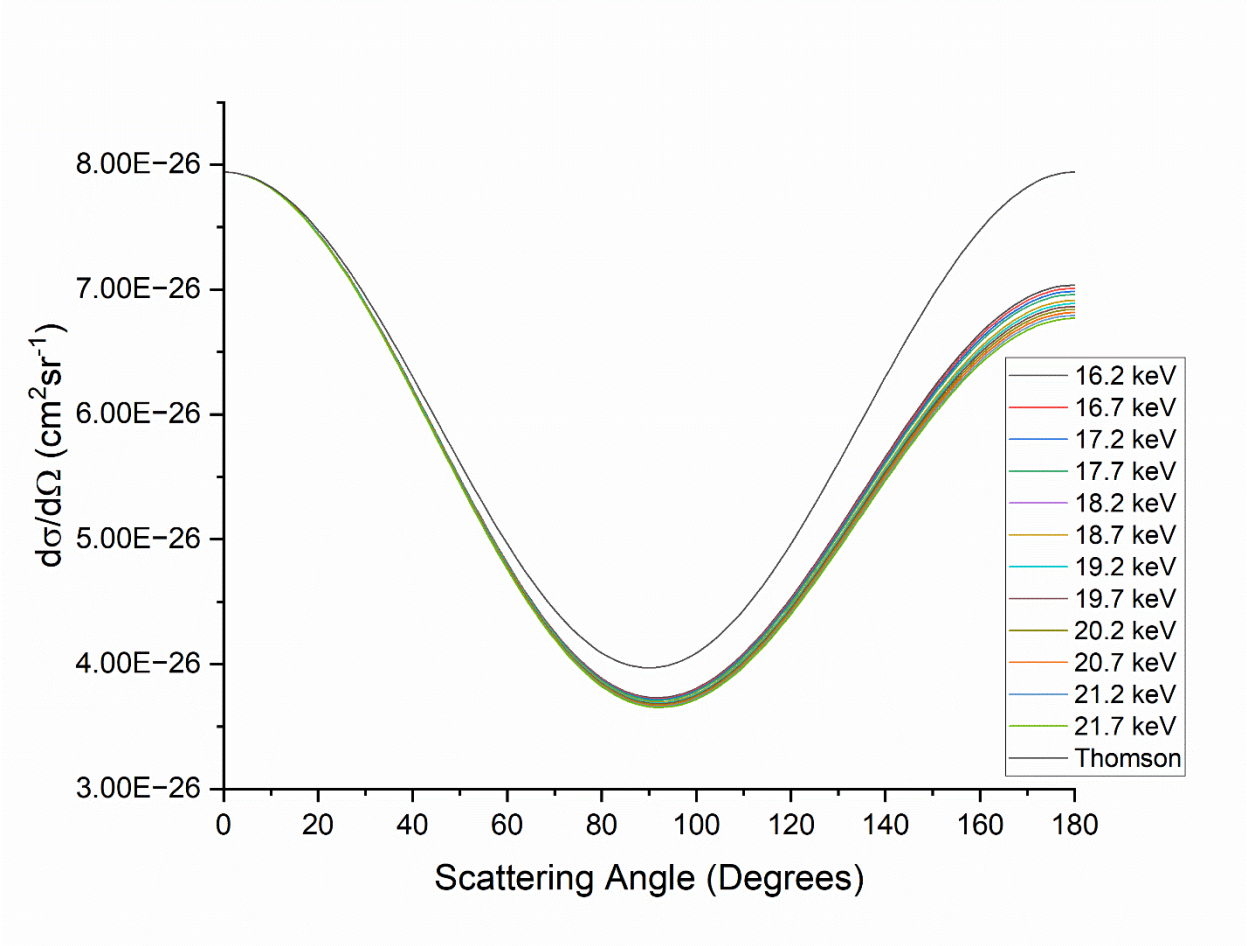

Figure 3: The behaviour of Compton scattering of photons over a range of 0 – 180° as predicted by the Klein-Nishina[5] formula. Thomson scattering is when the energy of the photon tends to 0 keV.

Results and Discussion

180° Measurement Geometry

The top three isotopes that resulted in the largest strontium Kα signal with a limited background from Compton scattering, were, in order, ^{112}Pd, ^{181}Ir, and ^{180}Os. Practically, two of these isotopes ^{181}Ir, and ^{180}Os cannot not be considered for use in an XRF system as their half-lives are extremely short. Similarly,^{142}Xe cannot be considered for use.

^{112}Pd undergoes β decay with a half-life of 21 hours to ^{112}Ag which β decays to ^{112}Cd. Due to internal conversion, ^{112}Pd will not only emit an 18.5 keV ϒ-ray but also silver L x-rays of energy 2.6 keV. These can however be filtered out by differential attenuation through source encapsulation which also removes any dose from the 265 keV β-particles. However, ^{112}Ag has a half-life of 3 hours, and after a short period of time, will enter into decay equilibrium with ^{112}Pd. ^{112}Ag β decays with the emission of a series of higher energy ϒ-rays which will contribute dose, but very little signal. Internal conversion will result in the emission of K_α x-rays from cadmium at 23 and 26 keV, which could contribute signal but at relative intensities <1% of the 18.5 keV ϒ-ray[15]. One disadvantage of ^{112}Pd is the relatively short half-life of 21.03 hours which would mean replacement every few days. Although this adds a challenge to in vivo measurements, this has been proved possible by researchers using ^{99m}Tc to measure platinum in the kidney[38]. The main drawback to this source is whether replacement every few days is at all possible. It is produced via heavy ion bombardment of ^{238}U (^{12}C + ^{238}U), a technique currently only being performed at beam line facilities in Italy at INFN[14]. Even if the material could be produced at other locations, the use of ^{238}U as a target material is challenging because of limitations on separated uranium isotopes through nuclear proliferation treaties. The use of ^{112}Pd is unlikely.

^{103}Pd could be a potential alternative as it is used as a radioisotope in brachytherapy seeds for cancer treatment[20,22]. ^{103}Pd produces few ϒ-rays but emits rhodium X-rays at 20.1 and 22.7 keV. The x-rays have photoelectric cross-sections that are higher than for the silver x-rays used in prior strontium XRF systems. These are sufficiently above the K absorption edge of strontium such that some Compton scattered x-rays could fluorescence the strontium in bone, leading to a very small increase in strontium x-ray signal. In terms of dose, the 2.8 keV rhodium Lα x-ray would contribute approximately 84% of the dose to the skin and 57% of the dose to the bone surface. However, with an appropriate filter design this could be eliminated. The half-life of ^{103}Pd of approximately 17 days would require source replacement on a monthly basis, which would be an ongoing operational cost.

The design of brachytherapy seeds is also an important consideration when choosing a fluorescence source. Certain materials present within the seed may result in additional X-rays being produced, leading to larger dose to a patient, and creating a more complicated spectrum from which to extract signal. For example, ^{125}I decays via electron capture to ^{125}Te. A 35.5 keV photon is released in 6.68% of decays, with tellurium X-rays released in 93.32% of decays. The construction of ^{125}I brachytherapy seeds from IsoAid™ consists of ^{125}I adsorbed onto a silver marker, housed in a titanium capsule[25]. Due to the presence of the silver marker, additional silver X-rays are produced from the source that would otherwise not be present. While this has the beneficial effect of inducing a larger XRF signal for strontium, it also complicates the spectrum due to scattering of the silver photons[25,41].

For ^{103}Pd, this is not a problem. TheraSeed® ^{103}Pd brachytherapy seeds consist of two ^{103}Pd graphite pellets on either side of a lead marker used for imaging in patients[20,26,36,39]. The pellets and marker are

housed in a titanium capsule. Due to this construction the X-rays that could be produced would be lead L-x-rays between 10.5 and 12.6 keV, titanium K x-rays from 4.5 – 4.9 keV and carbon at 277 eV[37]. The carbon and titanium x-rays can be easily filtered out by encapsulation, and any lead x-rays produced should be resolved from strontium peaks in the spectrum.

In terms of cost, ^{103}Pd seeds are 1.77 times[4] more expensive than ^{125}I seeds on a per implant basis and the shorter half-life means sources would need to be replaced a factor of 3.5 times more frequently If used in an ongoing basis, ^{103}Pd sources would therefore carry an operational cost that is approximately 6 times higher than ^{125}I seeds.

The largest strontium Kα x-ray signal was produced in the models by rhodium K x-rays, which may explain the excellent performance of some handheld x-ray sets. A disadvantage of this x-ray source is that the Compton scattered X-rays (17.5 keV) increase the background signal under the strontium Kα x-ray signal. As the minimum detection limit is proportional to the √background, this does reduce the precision of the system and worsen the MDL. Handheld x-ray sets do have an advantage over radioisotopes: their results are not dependent on the decay of an isotope, meaning ongoing source replacement costs are eliminated. As previously discussed, the handheld x-ray sets would be challenging to implement in some jurisdictions (e.g. Ontario, Canada)

Table 4 shows a summary of the isotopes and X-rays and their corresponding magnitudes.

Source	Effect of Compton background strontium K_α x-ray Peak (Signal:Background Ratio)	Effect of Compton background under strontium K_β x-ray Peak (Signal:Background Ratio)
^{103}Pd	569	1.21
^{112}Pd	10.5	1.37
^{142}Xe	11.7	1.18
^{171}Lu	7.1	1.48
^{180}Os	45.6	1.43
^{181}Ir	12.7	1.20
Mo X-rays	4.8	1.42
Rh X-rays	483	1.51

Table 4: The signal to background ratios for the strontium K_α and K_β x-ray peaks for each isotope investigated for a 180° measurement geometry modelling a 1500 µg Sr/g Ca calcium hydroxyapatite phantom with 2mm PLA overlay to simulate soft tissue.

90° Measurement Geometry

The three isotopes that produced the largest strontium K_α x-ray signal while having low signal backgrounds were in order, ^{181}Ir, ^{180}Os, and ^{171}Lu. Again, as with the 180° geometry, while ^{181}Ir and ^{180}Os have the highest peak areas, practically they would not be viable due to their extremely short half-lives. ^{171}Lu would thus be the next candidate, however there are limitations with this isotope. One limitation is the half-life of 8.2 days which would require frequent source changes. Furthermore, isotope production may be a challenge. ^{171}Lu is produced by bombarding ^{172}Yb targets with protons in the ^{172}Yb(p,2n)^{171}Lu reaction[18]. This has been performed at Chalk River Laboratories in Chalk River, Ontario in the past, but it is not clear that there could be a commercial provider of sources[18]. A further issue with ^{171}Lu is that the

ϒ-rays of energy 667 and 739 keV pose a problem for patient dose, as they represent 12% and 61% of the delivered skin dose respectively, while contributing little to strontium-ray signal.

Source	Effect of Compton background strontium Kα x-ray Peak (Signal:Background Ratio)	Effect of Compton background under strontium Kβ x-ray Peak (Signal:Background Ratio)
^{103}Pd	6.18×10^{10}	1.26
^{112}Pd	5.66×10^{3}	0.941
^{142}Xe	1.05×10^{13}	1.12
^{171}Lu	4.86×10^{9}	1.09
^{180}Os	4.82×10^{4}	0.600
^{181}Ir	1.29×10^{5}	1.08
Mo X-rays	7.70	1.14
Rh X-rays	109	0.949

Table 5: The signal to background ratios for the strontium K_α and K_β x-ray peaks for each isotope investigated for a 90°degree measurement geometry modelling a 1500 µg Sr/g Ca calcium hydroxyapatite phantom with 2mm PLA overlay to simulate soft tissue.

The magnitude of the strontium Kα x-ray signal is significantly lower for the 90° geometry compared with the 180°degree geometry. This is due in part to the effect of geometry on the signal. At 90° degrees, the amount of bone sampled using this model is 11% lower than for the 180° geometry. In the particular geometry modelled here, there are also potentially greater attenuation effects.

For source energies below ~ 65 keV any Compton scattered electrons in the 180° geometry will not contribute directly to the background under the strontium K_α x-ray peak, as the maximum electron energy is 13.29 keV, 0.8 keV lower than the strontium K_α x-ray energy of 14.1 keV. Any fluorescing sources that emit x- or ϒ-rays above this energy can create Compton electrons that could contribute to the background under the x-ray signal.

For the 90° geometry, sources that emit x- or ϒ-rays with energies below ~ 90 keV will not produce Compton electrons capable of contributing to the background under the strontium Kα x-ray peak. Sources with x- or ϒ-ray emissions above this energy can create Compton scattered electrons that could contribute to the background.

Conclusion

A systematic search has been undertaken to find radioisotope or x-ray sources that could improve the performance of systems to measure strontium in bone in vivo by x-ray fluorescence. Hand-held x-ray sets with rhodium targets are likely to be the best portable systems. However, these x-ray sets are challenging to use in some jurisdictions. When radioisotope source energies, availability and practicality are taken into account, it is recommended that an in vivo XRF system in a 180° measurement geometry that employs ^{103}Pd brachytherapy sources be tested, as it may offer advantages over the current best radioisotope-based systems.

References

[1] Ahlgren, L., Lidén, K., Mattsson, S. and Tejning, S. "X-ray fluorescence analysis of lead in human skeleton in vivo." *Scandinavian journal of work, environment & health*, 1976, pp.82-86.

[2] Bangash, S., U., K., McNeill, F., E., Farquarson, M., J., and Chettle D., R. "Feasibility of a 109Cd-based portable XRF device for measuring skin iron concentration in anaemic and beta-Thalassaemic patients" *Biomedical Physics and Engineering Express* vol 8, 2022, pp 065034.

[3] Blake, G., M. and Fogelman, I. "Effect of Bone Strontium on BMD Measurements" *Journal of Clinical Densitometry* vol 10, 1, 2007, pp 34 – 38.

[4] Blanchard, P., Pugh, T., J., Swanson, D., A., Mahmood, U., Chen, H., Wang, X., Graber, W., J., Kudchadker, R., J., Bruno, T., Feeley, T., and Frank, S., J. "Patient-reported health-related quality of life for men treated with low-dose-rate prostate brachytherapy as monotherapy with 125-iodine, 103-palladium, or 131-cesium: Results of a prospective phase II study" *Brachytherapy,* vol 17, 2018, pp 265 – 276.

[5] Elements of Nuclear Physics, Burcham, W., E. Longman. 1979

[6] Chettle D., R., McNeill F., E. "Elemental analysis in living human subjects using biomedical devices" *Physiological Measurements*, vol 40, no 12, 2019, pp 12TR01.

[7] Chu, S., Y., F., Ekström, L., P., Firestone, R., B. "WWW Table of Radioactive Isotopes, database version" 1999, http://nucleardata.nuclear.lu.se/nucleardata/toi/

[8] Da Silva, E., Mankovskii, G., Kirkham, B., Groves, J., Gherase, M., Fleming, D. E. B., and Pejović-Milić, A. "Evaluation of portable x-ray fluorescence spectrometers for in vivo quantification of bone strontium and lead on the basis of the minimum detectable limit: a phantom study." *Adv. X-Ray Anal.*, vol *61*, 2018, pp 116-121.

[9] "Protelos and osseor – referral | European Medicines Agency" *European Medicines Agency* September 19 2014. https://www.ema.europa.eu/en/medicines/human/referrals/protelos-osseor Accessed January 2024

[10] X-rays in Atomic and Nuclear Physics, Dyson, N., A. Longman. 1973

[11] "XRF – Energy-dispersive X-ray fluorescence analysis" helmut-fischer.com. Helmut Fischer Group. https://www.helmut-fischer.com/en/applications/solutions/xrf-energy-dispersive-x-ray-fluorescence-analysis Accessed March 2024.

[12] Hirayama, H., Yoshihito, N., Bielajew, A., F., Wilderman, S., J,., and Nelson, W., R. The EGS5 Code System. SLAC-R-730. 2005.

[13] Heirwegh, C., M., Chettle D., R., and Pejovic-Milic A. "*Ex vivo* evaluation of a coherent normalization procedure to quantify *in vivo* finger strontium XRS measurements" *Med Phys* vol 39 (2), 2012, pp 832-841.

[14] Houry, M., Lucas, R., Porquet, M., G., Theisen, C., Girod, M., Aiche, M., Aleonard, M., M., Astier, A., Barreau, G., Becker, F., and Chemin, J., F., Lucas, "Structure of neutron rich palladium isotopes produced in heavy ion induced fission" *The European Physical Journal A-Hadrons and Nuclei*, 1999, vol 6, pp 43 – 48.

[15] International Atomic Energy Agency (IAEA) "Live Chart of Nuclides" Livechart – Table of Nuclides – Nuclear structure and decay data, 2023, https://www-nds.iaea.org/relnsd/vcharthtml/VChartHTML.html Accessed April 2024

[16] Johns Hopkins "Bone Densiometry" https://www.hopkinsmedicine.org/health/treatment-tests-and-therapies/bone-densitometry Accessed March 2024

[17] Johns Hopkins "Osteopenia 101" 2007, https://www.hopkinsarthritis.org/ask-the-expert/osteopenia-101/ Accessed March 2024

[18] Kaye, G. "Excited states of 171Yv fed in the electron capture decay of 171Lu" *Nuclear Physics*, vol 86, no 2, 1966, pp 241 – 267.

[19] Lord, M., L., Chettle, D., R., Grafe, J., L., Noseworthy, M., D., and McNeill, F., E. "Observed deposition of gadolinium in bone using a new noninvasive in vivo biomedical device: results of a small pilot feasibility study" *Radiology*, vol 287, 2017, pp 96 – 103.

[20] Makhlouf, A., A., Boyd, J., C., Chapman, T., N., and Theodorescu, D. "Perioperative Costs and Charges of Prostate Brachytherapy and Prostatectomy" *Adult Urology*, 2002, vol 60, no 4, pp 656 – 660.

[21] Meunier, P. J., D. O. Slosman, P. D. Delmas, J. L. Sebert, M. L. Brandi, C. Albanese, R. Lorenc et al. "Strontium ranelate: dose-dependent effects in established postmenopausal vertebral osteoporosis—a 2-year randomized placebo controlled trial." *The Journal of Clinical Endocrinology & Metabolism* 87, no. 5, 2002, pp 2060-2066.

[22] Meunier P. J., Roux C., Seeman E., Ortolani S., Badurski J. E., Spector T. D., Cannata J., Balogh A., Lemmel E. M., Pors-Nielsen S., Rizzoli R., Genant H. K., and Reginster J. Y. "The Effects of Strontium Ranelate on the Risk of Vertebral Fracture in Women with Postmenopausal Osteoporosis" *New England Journal of Medicine* vol 350(5), 2004 pp 459-468.

[23] Moise H., Adachi, J., D., Chettle, D., R., and Pejovic-Milic, A. "Monitoring bone strontium levels of an osteoporotic subject due to self-administration of strontium citrate with a novel diagnostic tool, *in vivo* XRF: A case study" *Bone* vol 51, 2012, pp 93-97.

[24] Moise, H., Chettle, D., R., and Pejovic-Milic, A. "Monitoring bone strontium intake in osteoporotic females self-supplementing with strontium citrate with a novel in-vivo X-ray fluorescence based diagnostic tool" *Bone* vol 61, 2014, pp 48 – 54.

[25] Moise, H. Energy Dispersive X-ray Fluorescence Spectrometry and Kinetic Modeling of Elemental Strontium in Human Bone. 2014. McMaster University, PhD.

[26] Monroe, J., I., and Williamson, J., F. "Monte Carlo-aided dosimetry of the Theragenics TheraSeed® Model 200 103Pd interstitial brachytherapy seed" *Medical Physics,* vol 29, no 4, 2002, pp 609 – 621.

[27] Nielsen, S., P., Slosman, D., Sorensen, O., H., Basse-Cathlinat, B., De Cassin P., Roux, C., and Meunier, P., J. "Influence of Strontium on Bone Mineral Density and Bone Mineral Content Measurements by Dual X-ray Absorptiometry" *Journal of Clinical Densitometry* vol 2, no 4, 1999, pp 371 – 379.

[28] Nguyen J. et al. "Investigating coherent normalization and dosimetry for the 241Am-La K XRF system" *Physiological Measurement* vol 41, 2020, pp 1-15.

[29] "Black-box warning for strontium ranelate (Protos) added to Product Information" *NPS MedicineWise* December 1 2014. https://www.nps.org.au/radar/articles/black-box-warning-for-strontium-ranelate-protos-added-to-product-information Accessed January 2024

[30] Pejovic-Milic, A., Stronach, I. M., Gyorffy, J., Webber, C., E., and Chettle, D., R. "Quantification of bone strontium levels in humans by in vivo x-ray fluorescence" *Medical Physics* vol 31, no 3, 2004, pp 528 – 538.

[31] Puri, S., et al. "K and L shell x-ray fluorescence cross sections" *Atomic Data and Nuclear Data Tables* vol 61, 1995, pp 289-311.

[32] Reginster, J., Y., Deroisy, R., Dougados, M., Jupsin, I., Colette, J., and Roux, C. "Prevention of early postmenopausal bone loss by strontium ranelate: the randomized, two-year, double-masked, dose-ranging, placebo-controlled PREVOS trial." *Osteoporosis international* 13, 2002, pp 925-931.

[33] Reginster J. Y., Seeman E., De Vernejoul M. C., Adami S., Compston J., Phenekos C., Devogelaer J. P., Diaz-Curiel M., Sawicki A., Goemaere S., Sorensen O. H., Felsenberg D., and Meunier P. J. "Strontium Ranelate Reduces the Risk of Nonvertebral Fractures in Postmenopausal Women With Osteoporosis: Treatment of Peripheral Osteoporosis (TROPOS) Study" *Journal of Clinical Endocrinology and Metabolism*, vol 90, 2005, pp 2816 – 2822.

[34] Specht, A., J., Mostafaei, F., Lin Y., Xu., J and Nie, L., H. "Measurements of Strontium Levels in Human Bone In Vivo Using Portable X-ray Fluorescence (XRF)" *Applied Spectroscopy* Vol 71, no 18, 2017, pp 1962-1968.

[35] Snyder R., E., and Secord D., C. "The in situ measurement of strontium content in bone using x-ray fluorescence analysis" *Physics in Medicine and Biology* vol 27, no 4, 1982, pp 515 – 529

[36] "Theraseed® Palladium 103" Theragenics.com. Theragenics. https://www.theragenics.com/product-catalog/brachytherapy/brachytherapy-seeds/theraseed/ Accessed May 2024

[37] Thompson, A., Attwood, D., Gullikson, E., Howells, M., Kim, K., J., Kirz, J., Kortright, J., Lindau, I., Liu, Y., Pianetta, P., Robinson, A., Scofield, J., Underwood, J., Williams, G., and Winick, H. "X-ray Data Booklet" *Lawrence Berkeley National Laboratory*, 2009.

[38] Todd A., C., Chettle D., R., Scott M.,bC., Somervaille L., J., Braithwaite R., A., Beaney R., P., and Buxton E., J. "A pilot study using 99mTc to measure lead and platinum in the human kidney." *Nuclear medicine and biology*, vol 20, no 5, 1993, pp 589 – 95.

[39] Wallner, K., Merrick, G., True, L., Sutlief, S., Cavanagh, W., and Butler, W. "125I versus 103Pd for low-risk prostate cancer: preliminary PSA outcomes from a prospective randomized multicenter trial" *International Journal of Radiation Oncology, Biology, Physics,* vol 57, no 5, 2003, pp 1297 – 1303.

[40] Wielpolski L., Vartsky, D., Yasumura, S., and Cohn, S., H. “Application of XRF to Measure Strontium in Human Bone In Vivo” *Advances in X-ray Analysis,* vol 26, 1982, pp 415 – 421.

[41] Zamburlini, M., Pejovic-Milic, A., Chettle, D., R., Webber, C., E., and Gyorffy, J. “In vivo study of an x-ray fluorescence system to detect bone strontium non-invasively” *Physics in Medicine and Biology* vol 52, 2007, pp 2107 – 2122.

[42] Zhang, X., Wells, E., M., Specht, A., J., Weisskopf, M., G., Weuve, J., and Nie, L., H. “In vivo quantification of strontium in bone among adults using portable x-ray fluorescence” *Journal of Trace Elements in Medicine and Biology* vol 74, 2022, pp 127077.

Chapter 5:

5.1 Conclusions and Future Work:

In this thesis, I have described the work I have performed to improve in vivo measurements of strontium in bone using x-ray fluorescence. The novel thesis work is presented in three separate chapters that outline 1) the design and implementation of a new detection system consisting of an SDD and ^{109}Cd source, 2) Monte Carlo simulations of the developed system that test the validity of the application of the normalization of strontium Kα x-ray signals to coherent scatter signals to account for tissue overlay thickness and patient position, and 3) the results of a systematic search using Monte Carlo modelling to find an ' ideal' x-ray fluorescence source for in vivo measurements of strontium in bone.

In Chapter 2, I show how I was able to develop and implement a new X-ray fluorescence system for the measurement of strontium in vivo, outlining the testing of the new system that employs an SDD detector and a ^{109}Cd source. In experimental tests, the system performed as well as previous systems, with minimum detectable limits of similar magnitude. However, the system achieved these detection limits with a dead time that was a factor of approximately 10 times lower than prior measurement systems. I suggest that if a significantly more active ^{109}Cd source were to be employed with the system, that it would achieve significantly better detection limits than previous radioisotope-based systems. The system also offers further advantages over prior systems. It is considerably smaller than previously used systems, in part due to it's use of Peltier rather than LN_2 cooling. It thus represents a step towards a system that could be employed clinically as it is lightweight, portable and can be used in locations where liquid nitrogen is difficult obtain, while also achieving either a better detection limit (or shorter measurement times).

The system is calibrated using 3D printed phantoms and to the best of my knowledge, these are the first 3D printed finger phantoms to be employed as calibration standards for low-energy XRF measurements. The 3D printing process provides significant advantages over other phantom methodologies as it is easy to use, low-cost, and creates robust phantoms. It provides a simple method for the creation of anatomically correct phantoms whose x-ray properties match human bone and soft tissue well, potentially resulting in more accurate calibration of the system.

Through Monte Carlo simulations using the EGS5 code, I was able to show that while normalization of the strontium Kα signal to the coherent scatter signal is not able to correct for tissue overlay thickness, it may be able to correct for positioning and motion errors. Furthermore, it seems likely that the previously published Compton correlation method can used with this system to estimate soft tissue thickness. This estimate, combined with the coherent normalization, could potentially eliminate the need for independent measurements of soft tissue overlay thickness, such as the ultrasound measurements that have been previously employed. This too represents a step towards a system that can be clinically implemented, as it reduces a bone strontium measurement to one patient appointment with a single technology, rather than two separate appointments with different technologies.

While I have developed a system that is an improvement over prior technologies, I have also conducted the first systematic investigation of possible fluorescing sources to improve in vivo strontium XRF measurements. The results of this investigation lead me to recommend two different paths forward for future research. Radioisotope-based in vivo strontium measurement systems may be improved by employing ^{103}Pd sources, potentially in the form of low cost, readily obtainable brachytherapy seeds. Portable X-ray gun systems already perform better than radioisotope systems for the in vivo measurement of strontium in bone (albeit at a higher dose). However, these systems may be improved if they employ rhodium target in the x-ray set.

I acknowledge that there are limitations to this work. First, while I have shown that ^{109}Cd employed with an SDD is an excellent basis for a system, this source is costly and hard to obtain in a 'spot' source design. The sources used in this work were manufactured in a Russian cyclotron facility and the most recently acquired source cost $24,000 CAD. Current geopolitics mean we cannot currently purchase further sources.

Secondly, calcium hydroxyapatite phantoms were chosen over plaster-of-Paris phantoms in this work for two reasons: one is that calcium hydroxyapatite is a more accurate analog to bone mineral, the second is that, in general, it has much lower levels of strontium contamination compared to plaster of Paris. However, in this work, we found that the contamination of the calcium hydroxyapatite phantoms was almost 3 times higher than the contamination observed in the plaster-of-Paris phantoms. Additionally, air bubbles became trapped in the phantoms when filling them, despite best efforts to remove them, causing the phantoms to crack.

5.2 Suggestions for future work

I have already made two suggestions for further work by suggesting the testing of ^{103}Pd sources and/or rhodium target x-ray sets as Monte Carlo studies indicated these as the two most promising for system improvement. Studies with both should be considered. However, because of the lengthy necessary approvals required for the use of portable X-ray guns for in vivo measurements, portable XRF may not be readily feasible in the Province of Ontario. Therefore, of the two systems, ^{103}Pd should be pursued first by researchers in Ontario. ^{103}Pd can be readily obtained as brachytherapy seeds, and this radioisotope system would also not result in as large a patient dose to the patient as portable XRF

I have further suggestions beyond the employment of different fluorescing sources as to how XRF systems for the in vivo measurement of strontium in bone may be improved.

As discussed previously, the contamination inherent in the hydroxyapatite phantoms was unexpectedly high being significantly larger than that of prior plaster-of-Paris phantoms. Contamination could likely be reduced by first purifying reagents before proceeding with the phantom fabrication process. There were also problems with air bubbles dried in the matrix which made phantoms very fragile. I suggest a vent could be modelled in the 3D- print design of the phantom to let out any trapped air, or alternatively, the cavity into which the hydroxyapatite solution is poured could be made larger.

If they become possible to obtain, a more active ^{109}Cd source could be used in the future to further improve the MDL and/or reduce the necessary measurement time of the system. As discussed in Chapter 2, a source that is 16 times higher in activity than the current ^{109}Cd source would likely result in an MDL that is approximately a factor of 3 times better than the MDL of previous systems. This would take advantage of the faster collection times of an SDD. In addition, updated electronics that have faster processing should be employed to make further system improvements, as this activity of source would result in a deadtime of 40 – 50% with current electronics.

The results from the simulations in Chapter 3 suggest a combination of Compton correction and normalization to the coherent signal can correct for soft tissue overlay thickness and position are encouraging, as it would mean that no additional methods are required to measure the thickness of the overlying soft tissue. While simulation data can be useful predictors, the accuracy of the measurement must still be validated. A study using ex vivo finger samples with intact overlying tissue, possibly from cadavers, should be performed to compare the bone strontium levels estimated by XRF in the ex vivo samples and levels estimated though another method such as ICP-MS. Confirmation of the accuracy of the system should be obtained prior to in vivo measurements

Finally, a full dosimetry study should be performed prior to in vivo studies to ensure the dose delivered by this new system is indeed within recommended limits for medical devices. While simple dosimetry

has been performed to assess skin dose, a fully study that assess the dose to other parts of the body form scattered radiation should be performed

5.3 Conclusion

Low doses of strontium may prove beneficial to those at risk or suffering from osteoporosis. However, the long-term effects of strontium supplementation are not known, therefore it is important to monitor people who are self-supplementing for any adverse health consequences. A new system for measurements of strontium in vivo has been developed that that may deliver improved performance over prior systems, with the added advantage of being more portable. The system was calibrated against 3D printed anthropomorphic finger, showing the potential of 3D printing applications for phantom creation. Monte Carlo simulations have shown that normalization of the strontium Kα x-ray signal to the coherent scatter signal, combined with a Compton correlation method, should result in a reduction in variability of the signal due to changes in positioning and tissue overlay thickness, providing a more robust measurement system. An investigation of ideal fluorescence sources showed that while this technology is an improvement over prior systems, there may be better sources that improve in vivo strontium measurements. Overall, this thesis has described work that shows the potential for yet further improvements to the in vivo measurement of strontium in bone by XRF and is another step towards potentially using such systems in a clinical setting.

Appendix:

Phantom	Concentration (ppm)	Mass Brushite (g)	Mass $Ca(OH)_2$ (g)	Volume of Sr stock solution (μL)
S0	0	8.0022	2.3125	0
S1	25	8.0027	2.3091	8
S2	50	7.0090	2.0201	14
S3	100	8.0180	2.3109	31
S4	250	8.0027	2.3116	78
S5	500	8.0006	2.3169	204
S6	750	6.9980	2.0235	233
S7	1000	8.0314	2.3201	311
S8	1250	8.0083	2.3203	389
S9	1500	8.0116	2.3194	467

Table A.1: Actual values of reagents used to create strontium-doped calcium hydroxyapatite phantoms for use in calibrating an in-vivo strontium XRF system. The above table is for phantoms with no PLA overlay.

Phantom	Concentration (ppm)	Mass Brushite (g)	Mass $Ca(OH)_2$ (g)	Volume of Sr stock solution (μL)
S0	0	5.0106	1.4502	0
S1	25	5.0063	1.4515	5
S2	50	5.0004	1.4419	10
S3	100	4.9994	1.4469	19
S4	250	5.025	1.4458	49
S5	500	5.0142	1.4439	97
S6	750	5.0054	1.4525	146
S7	1000	5.0089	1.445	194
S8	1250	4.9998	1.4457	243
S9	1500	5.0018	1.4483	292

Table A.2: Actual values of reagents used to create strontium-doped calcium hydroxyapatite phantoms for use in calibrating an in-vivo strontium XRF system. The above table is for phantoms with a 2mm overlay of PLA.

Phantom	Concentration (ppm)	Mass Brushite (g)	Mass $Ca(OH)_2$ (g)	Volume of Sr stock solution (µL)
S0	0	5.0185	1.4523	0
S1	25	5.0044	1.4482	5
S2	50	5.0192	1.473	10
S3	100	5.0018	1.4458	19
S4	250	5.0132	1.4593	49
S5	500	5.009	1.4519	97
S6	750	5.003	1.4529	146
S7	1000	5.0052	1.4429	194
S8	1250	5.0173	1.4528	243
S9	1500	5.0069	1.4565	292

Table A.3: Actual values of reagents used to create strontium-doped calcium hydroxyapatite phantoms for use in calibrating an in-vivo strontium XRF system. The above table is for phantoms with a 2.5 mm overlay of PLA.

Phantom	Concentration (ppm)	Mass Brushite (g)	Mass $Ca(OH)_2$ (g)	Volume of Sr stock solution (µL)
S0	0	5.0149	1.4503	0
S1	25	5.0233	1.4497	5
S2	50	5.0081	1.4518	10
S3	100	5.0158	1.4422	19
S4	250	5.0023	1.4486	49
S5	500	5.005	1.4427	97
S6	750	5.0104	1.4553	146
S7	1000	5.0027	1.4473	194
S8	1250	5.0134	1.4562	243
S9	1500	5.0134	1.4658	292

Table A.4: Actual values of reagents used to create strontium-doped calcium hydroxyapatite phantoms for use in calibrating an in-vivo strontium XRF system. The above table is for phantoms with a 2.9 mm overlay of PLA.

Phantom	Concentration (ppm)	Mass Brushite (g)	Mass $Ca(OH)_2$ (g)	Volume of Sr stock solution (µL)
S0	0	10.0037	2.8865	0
S1	25	10.0694	2.8916	10
S2	50	10.0046	2.8958	19
S3	100	10.0068	2.8896	39
S4	250	10.001	2.8881	97
S5	500	10.0094	2.8889	194
S6	750	10.0113	2.8869	252
S7	1000	4.9948	1.4583	194
S8	1250	10.0175	2.8886	486
S9	1500	5.0182	1.4484	292

Table A.5: Actual values of reagents used to create strontium-doped calcium hydroxyapatite phantoms for use in calibrating an in-vivo strontium XRF system. The above table is for phantoms with a 3.5 mm overlay of PLA.

Phantom	Concentration (ppm)	Mass Brushite (g)	Mass $Ca(OH)_2$ (g)	Volume of Sr stock solution (µL)
S0	0	10.0037	2.8865	0
S1	25	10.0694	2.8916	10
S2	50	10.0046	2.8958	19
S3	100	5.0042	1.4417	19
S4	250	5.0134	1.4552	49
S5	500	5.0060	1.4534	97
S6	750	5.0042	1.4418	146
S7	1000	5.0006	1.4646	194
S8	1250	10.0175	2.8886	486
S9	1500	4.9982	1.4492	292

Table A.6: Actual values of reagents used to create strontium-doped calcium hydroxyapatite phantoms for use in calibrating an in-vivo strontium XRF system. The above table is for phantoms with a 4 mm overlay of PLA.

Note that for the above tables (A.1 – A.6), a larger starting mass of brushite was used for some phantoms to expedite the creation process. The mass of $Ca(OH)_2$ and volume of strontium stock solution used was then adjusted accordingly so that the wanted concentration could be achieved.

```
ELEM
&INP IRAYL=1 /END
SI                    SI
SI
ENER
&INP AE=0.512,UE=10.511,AP=.001,UP=10.0 /END
TEST
 &INP /END
PWLF
 &INP /END
DECK
 &INP /END
ELEM
&INP IRAYL=1 /END
BE                    BE
BE
ENER
&INP AE=0.512,UE=10.511,AP=.001,UP=10.0 /END
TEST
 &INP /END
PWLF
 &INP /END
DECK
 &INP /END
MIXT
 &INP NE=5,RHO=3.05,RHOZ=0.2,41.38,18.49,39.87,0.06,IRAYL=1,IBOUND=1,INCOH=1,ICPROF=-
3,IAPRIM=1 /END
BONE
H  O  P  CA SR
ENER
```

```
&INP AE=0.521,UE=10.511,AP=.001,UP=10.0 /END
TEST
 &INP /END
PWLF
 &INP /END
DECK
 &INP /END
MIXT
 &INP NE=3,RHO=1.2046E-3,GASP=0.93174,RHOZ=0.75575,0.23143,0.01282,
  IAPRIM=1,IRAYL=1/END
AIR-AT-NTP
N  O  AR                AIR-GAS
ENER
 &INP AE=0.521,UE=10.511,AP=0.0010,UP=10.0 /END
TEST
 &INP /END
PWLF
 &INP /END
DECK
 &INP /END
COMP
 &INP NE=3,RHO=1.25,PZ(1)=1,PZ(2)=2,PZ(3)=1.5,IRAYL=1,IBOUND=1,INCOH=1,ICPROF=-3,IAPRIM=1
/END
PLA-PLASTIC
O  H  C
ENER
 &INP AE=0.521,UE=10.511,AP=0.0010,UP=10.0 /END
TEST
 &INP /END
PWLF
```

```
 &INP /END
DECK
 &INP /END
ELEM
&INP IRAYL=1 /END
NI                    NI
NI
ENER
&INP AE=0.521,UE=10.511,AP=.001,UP=10.0 /END
TEST
 &INP /END
PWLF
 &INP /END
DECK
 &INP /END
ELEM
&INP IRAYL=1 /END
AL                    AL
AL
ENER
&INP AE=0.521,UE=10.511,AP=.001,UP=10.0 /END
TEST
 &INP /END
PWLF
 &INP /END
DECK
 &INP /END
COMP
 &INP NE=2,RHO=0.96,PZ(1)=1,PZ(2)=1,IRAYL=1 /END
POLYSTYRENE
```

```
H  C
ENER
 &INP AE=0.521,UE=10.511,AP=0.0010,UP=10.0 /END
TEST
 &INP /END
PWLF
 &INP /END
DECK
 &INP /END
```

Figure A.1: Material card for a benchmarked EGS5 simulation with a 1500ppm phantom with 2mm of PLA overlay.

```
RCC  1      0.00       0.0       0.22       0.00       0.0
          0.045       0.68
RCC  2      0.00       0.0       0.0        0.00       0.0
          0.0025       0.7
RCC  3      0.00       0.0       0.0025     0.00       0.0
          1.36       0.7
RCC  4      0.00       0.0       0.00       0.00       0.0
          1.3615      1.00
RCC  5      0.00       0.0       0.00       0.00       0.0
          2.00       1.15
RCC  6      0.00       0.0       -0.025     0.00       0.0
          0.025       1.15

RCC  7      -3.00      0.0       -1.100     6.00       0.0
          0.00       0.375
RCC  8      -3.00      0.0       -1.100     6.50       0.0
          0.00       0.575
RCC  9      0.00       0.0       -4.00      0.00       0.0
          8.00       4.00
RCC  10     0.00       0.0       -5.00      0.00       0.0
          10.00      5.00
END
Z0001    +1
Z0002    +2
Z0003    +3    -1
Z0004    +4    -3    -2
Z0005    +5    -4    -3
Z0006    +6
Z0007    +7
Z0008    +8    -7
```

```
Z0009      +9      -8      -5      -6
Z0010      +10     -9
 END
  1   2   0   6   7   8   3   5   4   0
```

Figure A.2: Geometry card for a benchmarked EGS5 simulation with a 1500ppm phantom with 2mm of PLA overlay, for a 180^{o} geometry

```
 RCC   1       0.00        0.0        0.22        0.00        0.0
           0.045        0.68
 RCC   2       0.00        0.0        0.0        0.00        0.0
           0.0025        0.7
 RCC   3       0.00        0.0        0.0025        0.00        0.0
           1.36        0.7
 RCC   4       0.00        0.0        0.00        0.00        0.0
           1.3615        1.00
 RCC   5       0.00        0.0        0.00        0.00        0.0
           2.00        1.15
 RCC   6       0.00        0.0        -0.025        0.00        0.0
           0.025        1.15

 RCC   7       -3.00        0.0        -0.800        6.00        0.0
           0.00        0.375
 RCC   8       -3.00        0.0        -0.800        6.50        0.0
           0.00        0.575
 RCC   9       0.00        0.0        -4.00        0.00        0.0
           8.00        4.00
 RCC   10       0.00        0.0        -5.00        0.00        0.0
           10.00        5.00
 END
Z0001      +1
```

```
Z0002      +2
Z0003      +3      -1
Z0004      +4      -3      -2
Z0005      +5      -4      -3
Z0006      +6
Z0007      +7
Z0008      +8      -7
Z0009      +9      -8      -5      -6
Z0010      +10     -9
 END
  1   2   0   6   7   8   3   5   4   0
```

Figure A.3: Geometry card for a benchmarked EGS5 simulation with a 1500ppm phantom with 2mm of PLA overlay, for a 90^{o} geometry